UNIVERSIDAD COMPLUTENSE DE MADRID
FACULTAD DE CIENCIAS FÍSICAS

TESIS DOCTORAL

Emergent interfacial phenomena in complex-oxide based devices
Fenómenos emergentes de intercara en dispositivos basados en óxidos complejos

MEMORIA PARA OPTAR AL GRADO DE DOCTOR

PRESENTADA POR

Fernando Gallego Toledo

Directores

Federico Mompean García
Zouhair Sefrioui Khamali
Alberto Rivera Calzada

Madrid

UNIVERSIDAD COMPLUTENSE DE MADRID
FACULTAD DE CIENCIAS FÍSICAS

Emergent interfacial phenomena in complex-oxide based devices

Fenómenos emergentes de intercara en dispositivos basados en óxidos complejos

Fernando Gallego Toledo

Memoria presentada para optar al título de doctor

Directores:
Federico Mompean García
Zouhair Sefrioui Khamali
Alberto Rivera Calzada

Madrid 2020

II

A mis padres, mis abuelos,

Y a Carol

IV

"La vida es fluir"

Javier Ibarra (Kase.O)

"Enloquecer no es más que un acto de cordura. A veces para abrir la mente hay que forzar la cerradura"

José Javier Sánchez (Piezas)

"Bebiendo fe como si alguien me quitara el vaso"

Ignacio Fornés (Nach)

VI

Agradecimientos

Siendo sincero he tenido muchos momentos de duda en estos cuatro años en los que nunca llegué a estar seguro de que llegaría este momento. El momento de cerrar una fantástica etapa llena de experiencias, momentos felices, aprendizajes y personas maravillosas que me han ayudado, cada una a su manera, a andar este camino que jamás habría podido recorrer solo. Pero aquí estoy, y es momento de agradecer a todos aquellos que siempre han estado dispuestos a ofrecerme su ayuda.

En primer lugar, quiero agradecer a mis directores de tesis, Federico Mompean, Zouhair Sefrioui y Alberto Rivera, la confianza depositada en mí para este proyecto. Espero haber sabido devolverla a través del esfuerzo y el trabajo. Gracias Federico por la plena disposición a medir muestras a cuál más complicada y pelear con los datos y la física de los experimentos fuera cual fuese la hora y el día. Gracias Zouhair por transmitirme todo tu conocimiento en uniones túnel y por estar siempre dispuesto a diseñar nuevos experimentos por pura y genuina curiosidad. A Alberto, gracias por la paciencia y la ayuda que has tenido conmigo para convertirme en un científico capaz de manejarse en un laboratorio, por estar siempre dispuesto a echarme una mano con todo lo que se escapaba de mi alcance y por supuesto por el buen humor que muchas veces me ayudó a hacer más llevadero el día a día. Entre todos me distéis la oportunidad de comenzar una carrera científica y estoy muy agradecido por ello.

Quiero hacer una mención especial a Jacobo Santamaría, que es el artífice de que yo esté hoy donde estoy, tanto por los ánimos a buscar una tesis cuando estaba haciendo el máster como por las facilidades que me ha dado siempre para trabajar en el grupo de Física de Materiales Complejos (GFMC). Lo mismo puedo decir de Mar García en el 2d Foundry, donde me dieron la confianza de usar los equipos para hacer las medidas necesarias y fundamentales para completar esta tesis.

También quiero agradecer, en el seno del GFMC, a Carlos León, por no eludir nunca una discusión sobre física, por tarde que fuese y complicada la tarea, y por ese gran sentido del humor. A María Varela por estar siempre sonriente y dispuesta a resolver cualquier duda que surgiese y emprender proyectos en común. A Juan Beltrán, por aportar su punto de vista diferente y a veces transversal de los experimentos. A Rainer Schmidt por enseñarme otra forma de ver las cosas, tanto a nivel laboral como cultural. Y por las charlas de baloncesto. A Norbert Nemes por la cantidad de física que conoce y que es capaz de transmitir. A Neven Biskup por las agradables charlas y algunas ayudas.

En cuanto a las personas con las que he convivido día a día en el laboratorio, quiero agradecer también a Ana Pérez y Mariona Cabero, que me guiaron por el laboratorio y tuvieron la paciencia de enseñarme todo durante el primer año, tanto crecimiento de muestras, medidas, equipos, papeleo… Pero sobre todo me enseñaron que debía ser paciente y no desesperar si no salía todo como esperaba. De David Hernández aprendí que no hay excusas, hay que esforzarse y perseverar todos los días y no rendirse nunca. Quiero agradecer también a Víctor Rouco, que me ha salvado los últimos meses de tesis librándome del peso experimental, y a cambio sólo he tenido que aguantar que me preguntase ¿Tú me quieres? Cada 10 minutos. A Fabián Cuéllar y Javier Tornos no sabría por dónde empezar a agradeceros. Me enseñasteis todos los trucos de los equipos de crecimiento y fabricación, pero también a ser cuidadoso y metódico en cada cosa que hacía. Gracias por todo troncos, os habéis sentado conmigo tantas veces a ayudarme que no las puedo contar (algunas de esas veces hasta relacionadas con ciencia). Esta amistad hace años que se salió de los límites del trabajo y es de las mejores cosas que me llevo de aquí. Somos un equipo. Quiero agradecer a mis compañeros de viaje desde el principio, David Sánchez y Gloria Orfila. Gloria, unos diez viajes a Berlín yo creo que unen mucho, y de ahí salieron bromas que nos quedaremos para siempre. Tendremos que volver de turismo algún día para inventarnos más nombres de paradas. David, mi compañero de despacho desde el primer hasta el último día. Gracias por los chascarrillos, las siestas, y toda la ayuda tronco, nos vemos en París. A Andrea, gracias por traer energía y nuevas ganas al laboratorio cuando todo ardía, aunque a veces esa energía me sobrepasase. Cuida mucho de Apache y Josefa. A Alex, gracias por ser digno heredero del humor en el laboratorio, no es tarea fácil. A Emanuel, nos hemos visto poco, pero eres una gran persona, eso no se puede fingir. Y me encantan tus expresiones.

Fuera del laboratorio, quiero agradecer el buen trabajo de Nacho Carabias en el C.A.I. de difracción de Rayos X, el de Sergio Valencia en el Helmholtz Zentrum Berlin, y el de Manuel Valvidares y Hari Babu en el sincrotrón de ALBA. También agradezco a José González Calbet y Mariona Cabero por la adquisición y la interpretación de todas las imágenes de microscopía que aparecen en esta tesis, las cuales han sido fundamentales para el estudio realizado. Gracias a Suzanne te Velthuis por las medidas de difracción de neutrones presentadas. También gracias a Mari Carmen Muñoz y Juan Beltrán por el estudio de primeros principios llevado a cabo en las muestras de iridiato, así como a Javier García-Barriocanal por el análisis de los mapas del espacio recíproco en estas mismas muestras. Por último, agradecer a Manuel Bibes la confianza depositada en mí para darme la oportunidad de continuar con mi carrera científica incluso antes de ver la tesis terminada.

VIII

X

Content

XIV

Motivation, Objectives and outline of the thesis

Motivation

A wide variety of interesting and not predicted properties in solids arise at interfaces [1–4]. The principal characteristic of interfaces is the spatial symmetry breaking, which generates intrinsic electric fields and special charge distributions [5,6]. Also, two-dimensionality when the thickness is reduced, usually enhances the effects of electron correlations. These two features and their combination offer new possibilities and novel effects for surfaces and interfaces that are not present in the bulk material. The strong electronic correlations entangle the degrees of freedom of an electron within a solid: Charge, spin, lattice and orbital symmetry, leading to a rich diversity of states [7]. Specially in Transition Metal Oxides (TMOs), correlations generate properties like Mott transition or High Tc superconductivity. The bands occupation of the systems depends sensitively on the electronic and magnetic reconstruction at the interface. During this electronic reconstruction, charge density, repulsion energy and bandwidth, may vary dramatically, giving place to properties completely different from the bulk. Surfaces and interfaces are a platform for imposing boundary conditions to unleash the properties of hidden phases by altering the delicate balance between competing spin, charge, orbital and lattice degrees of freedom.

TMOs are compounds that consist of oxides of transition metal elements with unfilled d-orbitals [8]. In this systems, orbital hybridization of metallic d-orbitals and oxygen p-orbitals plays an important role in determining the intrinsic properties of the compounds, allowing these systems to be used for many different applications [9]. TMOs with 5d elements, like Iridium, add the Spin-Orbit coupling interaction [5] which restores the angular momentum sector. Large orbital moments endow these compounds with orbital magnetism which in presence of the Spin Orbit interaction make them suitable candidates for spintronic and spin-orbitronic applications.

Multiferroic tunnel junctions are powerful devices to study the interfacial properties of complex oxides. Tunnel current across a tunnel barrier depends strongly on the density of states of the electrodes at the interface, allowing us to tailor deep modifications of the ground state of the electrodes at their interfaces [10]. Moreover, strongly out of equilibrium states will occur at interfaces due to combined strain modulations and electric fields which promote mass transport (typically oxygen vacancies) to equalize chemical potentials. As a result, completely new phases may nucleate at the interface with unexpected electronic properties. In

our work, we have used a tunnel junction device to induce superconductivity at the interface of the non-superconducting cuprate, $La_{1-x}Sr_xCuO_{2.5-\delta}$ (LSCO), via a novel form of topotactic reaction, as used recently to induce superconductivity in an infinite-layer nickelate [11]. The combination of strain modulation with the strong electric field developing in ultrathin layers at moderate voltages triggers the ionization and transport of oxygen vacancies, which in turn dope the cuprate and modify its interfacial ground state from metallic to superconducting. The migration of oxygen plays the role of tuning the connectivity of the oxygen sublattice, a critical parameter controlling the nucleation of superconductivity in the cuprates through its effect on dimensionality, bandwidth or strength of electronic correlations.

In 5d oxides the strong spin orbit interaction couples electric field and symmetry breaking to the electronic structure. In this thesis we have used the strong electric fields developing in Electric Double Layer transistors (EDLT) to induce profound modifications of their electronic structure. In particular we have used $SrIrO_3$, which is a correlated semimetal with narrow t_{2g} bands, the interplay between Coulomb repulsion, bandwidth and Spin-Orbit interaction, which have similar values about 0.3 eV, can generate unexpected exotic phases [5]. These features can be modified with the dimensionality and also with the doping, leading to the apparition of a Mott transition. A clear evidence that electronic correlations are playing an important role in this system is that a magnetic transition occurs linked to the metal-to-insulator transition. Our main finding has been the possibility of using an external electric field to tailor the strength of electronic correlations, through the effect of spin orbit interaction on band splitting. The external control of the Coulomb interaction has enabled toggling the system among a metallic paramagnetic state and an insulating state with long range canted ferromagnetic order and topological properties.

These results demonstrate the possibility of using external stimuli to tailor the nucleation of new phases at interfaces of complex oxides layers and heterostructures. Inducing interfacial phase transitions into new electronic states, like the superconducting state on a non-superconducting cuprate or the ferromagnetic state in a paramagnetic iridate, are examples that illustrate the power of the method. These novel strategies may be used in the future for the design of novel functionalities in spintronic and spin orbitronic devices.

Objectives

- The central objective of this thesis is to explore routes to manipulate the emergent electronic states nucleating at oxide interfaces. This is a key step towards their functionalization in device novel concepts in a future oxide electronics. Two different routes will be explored, both connected to the large electric field developing in ultrathin layers at moderate voltages. One

will be to explore the coupling of ferroelectric polarization to mass transport at interfaces between ferroelectric oxides and other functional oxides (ferromagnetic or superconductor) to trigger the nucleation of novel spin or superconducting states. We aim at controlling novel states resulting from the coupling of the ferroelectric polarization to the electrochemical states driven by oxygen deficiency and mixed valence. The second will be the use of oxides with strong spin orbit interaction to couple the electronic structure to electric fields. We propose that the symmetry breaking induced by the strong electric field caused by the double layer in field effect experiments will control the mixing of orbitals with different symmetry to arrive at novel correlated states.

- These objectives will be accomplished by the growth of thin films and heterostructures based on complex oxides, their structural and electrical characterization, optimizing the conductive properties of the systems for their application of devices, by designing and fabricating multiferroic tunnel junctions and Hall bars as functional electronic devices and their magnetotransport characterization.

Thesis Outline

- **Chapter 1:** A brief introduction will be devoted to outline the general concepts of correlated oxides and to describe materials properties and experimental methods used in this thesis such as ferroelectric tunnel junctions and ionic liquid gating.

- **Chapter 2:** In this chapter the experimental techniques used during the thesis are described: Growing techniques like high pressure sputtering system; For structural characterization, X-Ray diffraction, Scanning Transmission Electron Microscopy and Atomic Force microscopy are described; X-Ray Magnetic Circular Dichroism and Polarized Neutron Reflectometry are used to obtain the interfacial and bulk magnetic profile. Details of the tunnel junction and Hall bar devices fabrication are presented. Measurement systems like He closed-cycle cryostation and Physical Properties Measurement System (PPMS) are described.

- **Chapter 3:** In this chapter structural and electric properties of $La_{0.84}Sr_{0.16}CuO_{2.5-\delta}$ thin films are studied. Symmetric $La_{0.84}Sr_{0.16}MnO_3/BaTiO_3/La_{0.84}Sr_{0.16}MnO_3$ and asymmetric $La_{0.84}Sr_{0.16}MnO_3/BaTiO_3/La_{0.84}Sr_{0.16}CuO_{2.5-\delta}$ tunnel junctions are studied. The arising of an induced magnetic state in the titanate due to the interfacial Superexchange with the bottom LSMO is discussed. The apparition of an interfacial superconducting state in LSCO and its tunability with the ferroelectric polarization direction is

demonstrated. The role of oxygen vacancies displacement and ionization in both experiments is considered.

- **Chapter 4:** In this chapter, a structural and electric characterization of $SrIrO_3$ thin films is performed. Both Metal-to-Insulator transitions as a function of the film thickness and as a function of the lattice parameter of the substrate are studied. The fabrication and characterization of an Electric Double Layer transistor based on $SrIrO_3$ are described. Magnetoresistance and Hall measurements are taken and modelized to explain the origin of the MIT. A weak ferromagnetic state is found in the insulating state of the SIO, probably associated to the electronic correlations of the system.

- **Chapter 5:** The final chapter summarizes the major conclusions of this work. Also an attached annex of the list of publications resulting from this thesis work and a list of national and international conference contributions.

References

[1]   A. Chen, Q. Su, H. Han, E. Enriquez, and Q. Jia, Adv. Mater. **31**, 1 (2019).

[2]   A. Schilling, M. Cantoni, J. D. Guo, and H. R. Ott, Nature **363**, 56 (1993).

[3]   R. Ramesh and D. G. Schlom, Nat. Rev. Mater. **4**, 257 (2019).

[4]   D. J. Groenendijk, C. Autieri, T. C. van Thiel, W. Brzezicki, J. R. Hortensius, D. Afanasiev, N. Gauquelin, P. Barone, K. H. W. van den Bos, S. van Aert, J. Verbeeck, A. Filippetti, S. Picozzi, M. Cuoco, and A. D. Caviglia, Phys. Rev. Res. **2**, 1 (2020).

[5]   D. J. Groenendijk, C. Autieri, J. Girovsky, M. C. Martinez-Velarte, N. Manca, G. Mattoni, A. M. R. V. L. Monteiro, N. Gauquelin, J. Verbeeck, A. F. Otte, M. Gabay, S. Picozzi, and A. D. Caviglia, Phys. Rev. Lett. **119**, 2 (2017).

[6]   E. I. Rashba, Sov. Phys. Solid State **2**, 1109 (1960).

[7]   Y. Tokura, M. Kawasaki, and N. Nagaosa, Nat. Phys. **13**, 1056 (2017).

[8]   C. N. R. Rao, Annu. Rev. Phys. Chem. **40**, 291 (1989).

[9]   V. Garcia and M. Bibes, Nat. Commun. **5**, 1 (2014).

[10]   M. Y. Zhuravlev, R. F. Sabirianov, S. S. Jaswal, and E. Y. Tsymbal, Phys. Rev. Lett. **94**, 1 (2005).

[11]   D. Li, K. Lee, B. Y. Wang, M. Osada, S. Crossley, H. R. Lee, Y. Cui, Y. Hikita, and H. Y. Hwang, Nature **572**, 624 (2019).

Chapter 1: Introduction

1. Introduction to complex oxides

In the last years, the demand for smaller, faster and more powerful computers has driven the interest in novel materials that can generate devices with improved properties like lower energy consumption, and higher speed and capacity of data storage. This interest expanded the field of materials research in general, and specially the field of transition metal oxides (TMOs). Understanding and tailoring the TMOs phenomenology will be crucial for the development of the next-generation quantum technologies, which surely will play an important role to address the future technological demands.

TMOs, or sometimes simply termed complex oxides, have a wide variety of exceptional physical properties due to the delicate interplay among their spin, charge and orbital degrees of freedom. In particular, transport behavior varies from insulating, to semiconducting or superconducting. They can also show a ferroic order below a critical (Curie) temperature. The broad diversity of properties originates in transition metal elements with unfilled d-orbitals: Ti, V, Cr, Mn, Fe, Co, Ni and Cu, which form stable oxides. The *3d* electrons of these compounds have a radial quantum number n=3 and angular-momentum quantum number *l*=2. The *3d* states are five-fold degenerated in a spherical potential because 2l+1=5. In addition, most of the compounds that show this kind of properties share a common atomic structure; they are perovskites. In this structure with generic formula ABO_3, the transition metal ions (B) are surrounded by six oxygen ions (O^{2-}), forming an octahedron. The transition metal ion is placed at the same distance to the six oxygen ions, so it is subject to a crystal field potential with cubic symmetry [1]. In a cubic crystal field, the eigen-functions of a *3d* electron are linear combinations of the spherical harmonics, being *d(x^2-y^2)* and *d($3z^2$-r^2)* the two high energy states, known as the e_g orbitals; and the three low energy states *d(xy)*, *d(xz)* and *d(yz)*, known as t_{2g} orbitals. The value of this splitting is around 3 eV in typical oxides with perovskite structure. The *d*-electrons experience competing forces: one is the Coulomb repulsion which tends to localize the electrons at atomic lattice sites, and the other is the hybridization of the *d*-orbitals with the oxygen *p*-orbitals, which tends to delocalize the electrons [2].

Typically, an electron in a solid has four degrees of freedom: Charge, spin, lattice and orbital symmetry, and the interaction between these parameters is responsible for the rich variety of states in these systems. The strong electronic correlations in these systems can lead to the emergence of novel functions in materials. These

properties include Mott metal-insulator transition, high temperature superconductivity, colossal magnetoresistance, topological insulators, etc. One of the most important discoveries in correlated materials science was the copper-oxide high-temperature superconductors in 1986, and this stirred the interest in studying the Mott transition in correlated electron systems [3].

High-Tc copper oxides have a structure composed by CuO_2 sheets, separated from each other by ionic "blocking layers". The carrier density in these sheets is high, reaching one electron (or hole) per Cu site, but even with this, the copper sheets are originally insulating because of the large electron correlations. The superconducting state is triggered when the CuO_2 layers are doped with holes coming from the blocking layers, modifying the number of conduction electrons and triggering the Mott transition [4].

Colossal magnetoresistance (CMR) manganites awakened a lot of interest in the 90s due to their gigantic decrease of resistance induced by the application of an external magnetic field. This effect comes from the interplay between electron properties and its effect on the lattice [5–7].

In general, the Mott transition (metal-insulator transition in a correlated-electron system, MIT) is one of the most important features in correlated materials. The origin of the MIT can be as simple as a bandgap closing, or be due to more complicated phenomena like Anderson localization, polaron self-trapping, etc. But almost all are related to electron-electron interaction beyond one particle scenario. In these systems with one electron per site, expected to be metals in the one electron theory of solids, electrostatic repulsion fixes every electron to its atomic site. This opens a gap at the Fermi energy, which is called Mott gap.

The enormous progress achieved in the study of complex oxides properties stems from the improvement in thin film deposition techniques (i.e. sputtering, Pulsed Laser Deposition, etc.). Modern growing techniques fabricate (ultra)thin layers with epitaxial relationships with the bottom substrates. The crystalline quality of the samples is as good as that of single crystals. Since most of the interesting properties of complex oxides arises at interfaces, with the optimization of the growing techniques, interfaces are grown between dissimilar materials with atomic perfection. The interfaces of transition-metal oxides (TMOs) present an intrinsic spatial symmetry breaking related to structure, so the interface quality is critical. Also, two-dimensionality usually enhances the effects of electron correlations by reducing their kinetic energy. These two features of complex oxide interfaces offer new possibilities and novel effects that are not present in the bulk material.

There are three important symmetries to consider, spatial inversion symmetry (**r** ->-**r**), responsible for the ferroelectricity in insulating materials, for example; time reversal symmetry (**t** -> **-t**), whose rupture is associated with magnetism and Gauge (G) symmetry, associated with the phase (θ) change in the wavefunction, so that broken G symmetry is related to superconductivity and superfluidity [8]. The spatial symmetry breaking at the interface between correlated oxides can determine the nucleation of emergent electronic phases with interesting properties that were not present in the constituent oxides [9]. The three parameters to consider in the study of interfacial properties of correlated oxides are the Charge density (*n*), repulsion energy (*U*), and bandwidth (*W*). The charge density varies smoothly across the interface between oxides with different electrochemical potentials over the Thomas-Fermi screening length. The repulsive interaction *U* depends critically on the ionic environment. Finally, the bandwidth *W* is controlled by the bond reconstruction at the interface. These interfacial properties may have a critical influence in the nucleation of novel phases during a process called electronic reconstruction.

Complex oxides based on *5d* elements (like Osmium or Iridium) are not widely used due to the shortage of these elements in nature and the difficulty of synthesizing them into a compound. These materials have also strong electronic correlations, but here combined with another important property, a strong spin-orbit coupling (SOC) interaction. This interaction consists of a dependence between the spin and orbital degrees of freedom. The SOC is a useful property for the development of spintronic devices, which are devices that operate with spin instead of charge currents, giving rise to minimal dissipation devices [10]. In this work we are studying the 113 strontium iridiate $SrIrO_3$ because it combines electronic correlations with SOC and is a candidate for the next generation of spin-based devices.

1.1 Electronic correlations

Transition metal oxides have incompletely filled *d*-orbitals with narrow energy bands. Due to the overlap between contiguous orbitals, the individual electrons cannot be described as non-interacting systems. The interaction is indeed described using the Hubbard model, which is the simplest mode of interacting particles in a lattice, with only two terms in the Hamiltonian. The first one is the kinetic energy ***t***, the energy the electrons need to hop between neighboring lattice sites, and the second one is a potential term consisting of an additional energy *U* for a pair of electrons occupying the same site, due to Coulomb repulsion (Figure 1.1). For electrons in a solid, the Hubbard model can be considered as an improvement on the tight-binding model, which includes only the hopping term [11]. For strong
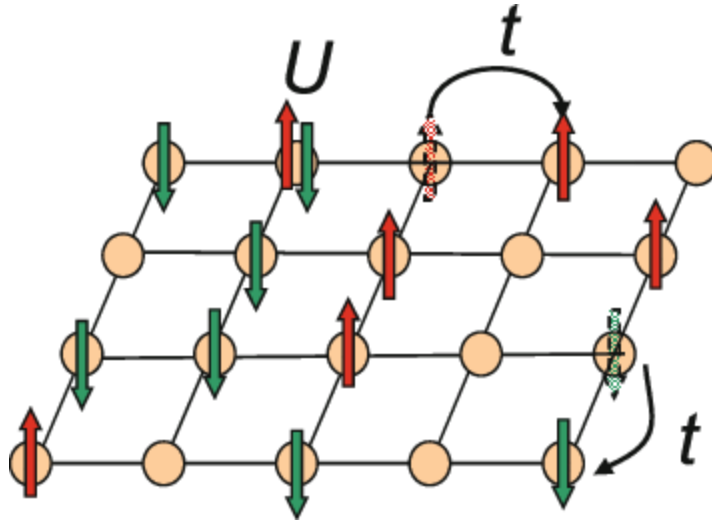
Figure 1.1: Schematic figure of the Hubbard model. t is the hopping parameter and U is the energy cost for a double occupation of a site. Spin up and down electrons are represented with up and down arrows, respectively

interactions, it can give qualitatively different behavior from the tight-binding model, and correctly predicts the existence of Mott insulators. These materials are prevented from becoming conducting by the strong repulsion between the electrons.

The Hubbard Hamiltonian expression is as follows:

$$H = -t \sum_{i,j,\sigma} c_{j\sigma}^{\dagger} c_{i\sigma} + \sum_{i} U_i n_{i\uparrow} n_{i\downarrow} \tag{1}$$

The first term corresponds to kinetic energy and describes the destruction of an electron on site i and its creation on the j site. The second term is the energy U added if a site is occupied with two electrons. $c_{j\sigma}^{\dagger}$, $c_{i\sigma}$ and $n_{i\uparrow}$ are the creation, annihilation and number operator of an electron on the *i*-th side with spin σ.

While conventional band theory predicts a metallic state for a half-filled band, the Hubbard model correctly predicts the Mott insulating state. The Hubbard model is important for high-temperature superconductivity, for example. Additionally, it encouraged the development of dynamical mean-field theory, which is widely used to calculate the electronic structure of strongly correlated materials.

2. Introduction to tunnel junctions

When an ultrathin insulating layer is growth between two metallic materials (called electrodes), they form a tunnel junction. The first epitaxial tunnel junctions based on complex oxides used manganites as electrodes and a 6 nm thick SrTiO₃ film as tunnel barrier [12]. The tunnel current is extremely sensitive to the density of states at the interface between the barrier and the electrodes, thus it can be used for studying interfacial properties of the system. In this sense, tunnel junctions are one of the best options to exploit novel interface effects in electronic devices, and in particular TMOs. The variety of interfacial properties available in TMO are displayed in their phase diagrams, which are very dependent on doping, so small changes in the carrier density can induce large changes in the physical properties. Further tuning of the properties of the system is enabled the by other external degrees of freedom, like mechanical strain or magnetic fields.

2.1 Spin dependent tunneling

Electron tunneling is a quantum mechanical effect by which an electron in a metallic electrode can flow into another electrode across an insulating barrier. The traditional way of modelling these phenomena is to consider the electron as a wave that encounters a potential step. Although most of the intensity is reflected, some of it decays exponentially within the barrier width. If the barrier is sufficiently thin, there exist a non-zero probability of finding the electron on the other side of the tunnel barrier.

The current across the structure can be calculated as the product of the following terms: the density of states (DOS) in the electrodes, the square of the tunneling matrix elements *M*, obtained from the transmission coefficient *T(E)=|M|²*, the probability of the thermal occupation of the initial (a) state, and the probability that the final state (b) is empty.

$$I_{a \to b}(V) = \int_{-\infty}^{+\infty} \rho_1(E)\rho_2(E + eV)|M|^2 f(E)[1 - f(E + eV)]dE \qquad (2)$$

The total tunnel current is given by $(I_{a \to b} - I_{b \to a})$.

For non-magnetic electrodes and a dielectric diamagnetic barrier, Simmons gave an expression for the current density, *J*, using the Wentzel-Kramers-Brillouin (WKB) approximation [13] for an arbitrary barrier of average height $\bar{\varphi}$ above the Fermi level and assuming T=0 (so Fermi-Dirac functions can be approximated to step functions). The result for a trapezoidal barrier is as follows:

$$J(V) = \frac{J_0}{d^2}\left(\varphi - \frac{eV}{2}\right)\exp\left[-Ad\sqrt{\varphi - \frac{eV}{2}}\right] - \frac{J_0}{d^2}\left(\varphi + \frac{eV}{2}\right)\exp\left[-Ad\sqrt{\varphi + \frac{eV}{2}}\right] \quad (3)$$

Where $A = 4\pi\sqrt{2m^*}\hbar$ and $J_0 = {}^e/_{2\pi\hbar}$, with m^* as the effective mass of the tunneling electrons, *d* is the barrier thickness, φ is the average barrier height and *eV* is the applied bias.

The tunnel current density depends, thus, exponentially on the barrier thickness, and the square root of the effective mass and the barrier height. This dependence implies that, even small changes in one of these parameters, will have a strong influence on the tunnel current. The tunnel current density dependence with the voltage is:

$$J \sim \alpha V + \beta V^3 \quad (4)$$

Therefore, the conductance $G = dI/dV$ will have a quadratic dependence with voltage. The expression for the current density is only valid for bias lower than φ / *e*, above it, the tunneling is no longer direct, and should be described by a Fowler-Nordheim regime.

Simmons makes two approximations in this tunnel current model. The first one is that tunneling is elastic, so the final state of an electron tunneling from the Fermi level of the first electrode is a state at an energy eV above the Fermi level in the second electrode. The second one is that the electrode density of states (DOS) does not have any influence on the tunnel current. Indeed, tunnel junctions based on simple metals with broad *s* bands the electrode DOS effects are negligible, but in tunnel junctions with superconducting electrodes, the DOS has an important role. Below the critical temperature, the opening of a quasi-particle gap results in strong DOS variations close to the Fermi level that are visible in I(V) and G(V) curves. Even junctions with electrodes of the same material present different interfacial properties at both sides of the insulating barrier, so the barrier profiles should be asymmetric. A barrier model was reported by Brinkmann [14] using a trapezoidal potential model where:

$$\bar{\varphi} = \frac{\varphi_1 + \varphi_2}{2} \quad (5)$$

$\bar{\varphi}$ being the effective barrier height in eV.
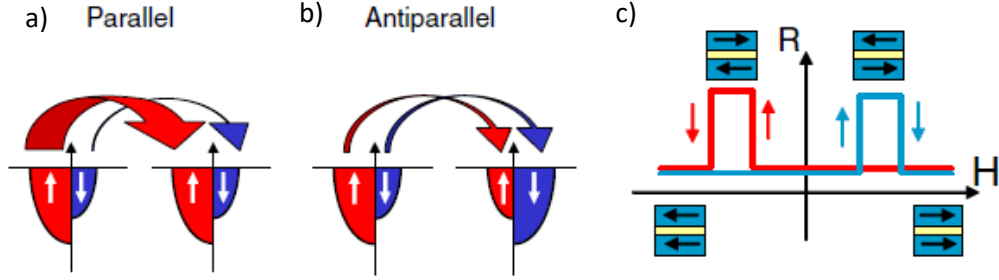
Figure 1.2: Scheme of the tunnel current dependence of the relative orientation of the magnetization of the ferromagnetic electrodes. If they are parallel (a), there will be a strong current from the spin-up channel, resulting in a low resistance state. If the electrodes are anti-parallel (b), there will be a weak total current and so a high resistance state. The system will have 2 different resistance states as shown in the scheme in (c).

In tunnel junctions, direct tunneling is not the only possible transport mechanism across the barrier. There are at least three mechanisms: Direct tunneling, Fowler-Nordheim and thermoionic emission [15]. Direct tunneling dominates the conduction at low voltages, while the Fowler-Nordheim regime dominates at large voltages. Experimentally it is difficult to establish a frontier between the different methods, since it depends on various parameters like dielectric constants, screening lengths, barrier heights and effective masses. Nevertheless, it is possible to identify the mechanism by studying its temperature and voltage dependence. Direct tunneling is independent from temperature.

When the electrodes are ferromagnetic metals, their non-equivalent DOS for spin up and down bring about novel physical effects. Assuming the spin is conserved during the tunneling process, the total current will be the sum of the spin-up and spin-down currents. Then the conductance of the magnetic tunnel junction (MTJ) will be different for the parallel and the anti-parallel states and proportional to the DOS of the electrodes in both cases:

$$G_P \sim N_{1\uparrow}N_{2\uparrow} + N_{1\downarrow}N_{2\downarrow} \qquad (6)$$

$$G_{AP} \sim N_{1\uparrow}N_{2\downarrow} + N_{1\downarrow}N_{2\uparrow} \qquad (7)$$

Where N_1 and N_2 are the DOS of the electrodes for the majority ($\uparrow$) and minority ($\downarrow$) spin electrons (Figure 1.2). The tunnel resistance is not the same for the parallel and anti-parallel states, so we can define an expression proportional to the resistance difference, which is the Jullière expression [16] of Tunnel Magnetoresistance effect (TMR):

$$TMR = \frac{R_{AP} - R_P}{R_P} = \frac{2P_{spin}^1 P_{spin}^2}{1 - P_{spin}^1 P_{spin}^2} \qquad (8)$$

With $P_{spin}^i = \frac{N_{i\uparrow} - N_{i\downarrow}}{N_{i\uparrow} + N_{i\downarrow}}$, for i=1,2. In order to enhance the TMR effect, Jullière's expression suggests searching for materials with a high spin polarization. Half Metals are materials with a spin polarization of 100%; their DOS at the fermi level is finite for one spin direction and negligible for the other. Optimized junctions based on half-metallic manganite electrodes like $La_{2/3}Sr_{1/3}MnO_3$ (LSMO) exhibit TMR values of several hundred percent, corresponding within the Jullière model to P_{spin} of up to 95%.

2.2 Ferroelectric oxides

Although all dielectrics can be electrically polarized and show a dipolar moment per unit volume when subject to an external electric field, a ferroelectric material is an insulating material that have at least two metastable states of spontaneous polarization, which have a non-zero electric polarization in absence of applied electric field. For a system to be considered ferroelectric, it must be possible to switch between the two states by applying an electric field larger than the characteristic coercive field of the material. The switching mechanism are collective ionic displacements rather than individual unit cell distortions. Therefore, the existence of ferroelectricity in a system depends crucially on its crystal symmetry. The confirmation of ferroelectricity comes from the measurement of polarization-field hysteresis loops (P-E), as in Figure 1.3.

In ferroelectrics, non-zero polarization remains until temperature increases up to the Curie temperature (T_c) where a phase transition occurs from the ferroelectric state to a non-polar paraelectric phase. The symmetry-breaking that takes place in the transition from the paraelectric to the ferroelectric state is consistent with a second-order transition because the dielectric susceptibility diverges during it.

Most of the ferroelectric oxides have perovskite structure, with formula ABO_3, with A and B representing the cationic elements. The structure consists on an oxygen octahedron centered on a cation B, and A cations occupy the spaces between octahedra. Below T_c, the structure is polar: the shift of B cations away from the central position induces a net dipole moment showing polarization whose direction
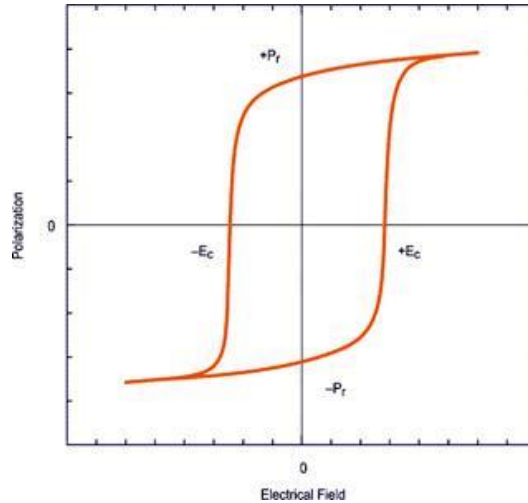
Figure 1.3: Ferroelectric hysteresis cycle representation. P_R is the remanent polarization in absence of electric field and E_C is the coercive electric field. At zero field two stable polarization states can be achieved.

and magnitude depend on the B cations with respect to the center of charges defined by the oxygen octahedra (Figure 1.4).

In an ideal cubic perovskite, the structure is centrosymmetric, and therefore, not ferroelectric. The reason for the existence of ferroelectricity is the presence of long-range Coulomb forces that favor the ferroelectric state. These long-range forces are in competition with short-range repulsions between the electron clouds, which favor the non-polar structure [17,18]. The balance between the short-range repulsion that favor the non-ferroelectric structure and bonding considerations which favor the necessary distortions to generate the ferroelectric phase, determines the apparition of ferroelectricity in a material [19].
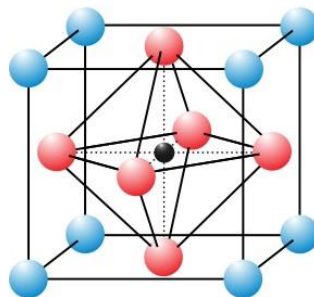
Figure 1.4: Crystal structure of a perovskite ABO_3 in a paraelectric phase, where A are the blue ions, B the black ion, and the red circles are the oxygen octahedra.

2.3 Ferroelectric tunnel junctions

The recent advances in the understanding of ferroelectricity at the nanoscale have motivated the design and fabrication of heterostructures for data storage in which the information resides in the direction of the ferroelectric polarization. A ferroelectric tunnel junction (FTJ) is expected to show very interesting physics resulting from the interplay between tunneling and ferroelectricity at the nanoscale. Tsymbal and Kohlstedt [20] have proposed three possible mechanisms for the modulation of the tunnel current with the modification of the FE polarization of the barrier (Figure 1.5).

1. First, accumulated polarization charges at the interface of the ferroelectric will be asymmetrically compensated on each electrode depending on their Thomas-Fermi screening length (λ_{eff}). Polarization charges at a ferroelectric surface, depending on their sign, will repel or attract electrons in the vicinity of the electrodes, λ_{eff}, and the excess charges will be screened farther away. The Thomas-Fermi screening length is a function of the electronic DOS at the Fermi level: for good metals, it can be 0.1 nm, while for semiconductors it can reach tens of nanometers, and the screening will be imperfect. The different screening induces an asymmetric variation of the electrostatic potential across the tunnel barrier. When the electrodes connecting the barrier are made from different materials, the screening is different for the two interfaces and there is a shift of the average barrier height of $\varphi \pm \Delta\varphi$ when the polarization flips. In an idealized ferroelectric capacitor where the metal electrodes are perfect conductors, the screening charges are located at the interface with the ferroelectric,
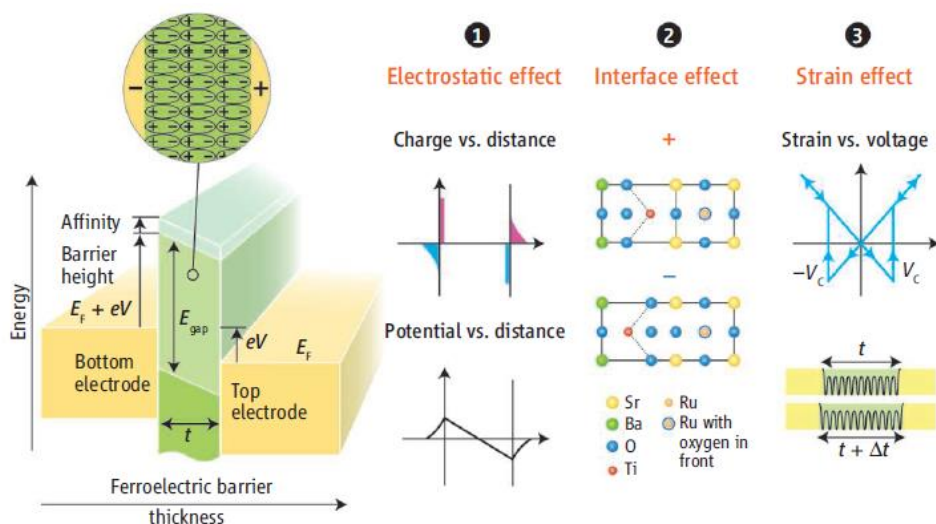
Figure 1.5: Scheme of a tunnel junction with a ferroelectric acting as a tunnel barrier and three possible explanations for the tunnel current variation [20].

14

compensating the polarization charges. In a real metallic electrode, the screening charges are distributed over a small but finite length in the metal of about λ_{eff} = 0.1 nm. This spatial charge distribution creates finite dipoles at the interfaces and leads to an associated voltage drop:

$$\Delta V = \frac{\lambda_{\text{eff}}}{\varepsilon_0} P \tag{9}$$

where P is the FE polarization and ε_0 is the vacuum electric permittivity.

2. The second mechanism is the interface effect. The interfacial DOS is modified according to the position of the ions in the last atomic layer in the ferroelectric, which in turn affects the tunnel current.

3. The third one is related to the piezoelectric effect through which the barrier thickness would be changed upon switching the polarization direction. Since the tunnel current depends exponentially on the barrier width, it can be widely modified.

The size of the barrier has a great influence in the tunnel current, as have been previously discussed. To fabricate a ferroelectric tunnel junction, the most important thing is to grow a ferroelectric layer thin enough to permit electrons to tunnel across it. But in many cases, samples do not show ferroelectricity below certain thickness, probably due to the fabrication process. The most common issues are the apparition of dead layers, grain boundaries and defects such as oxygen vacancies. Extrinsic factors like low quality FE layer also contribute, and this is evidenced by the fact that the minimum thickness for ferroelectricity has decreased by orders of magnitude over the years.

The key parameter that sets the critical thickness appears to be the screening of the depolarizing field. This field is inversely proportional to the film thickness and may lead to the suppression of ferroelectricity:

$$E_d = -2\frac{\lambda_{eff}}{d\varepsilon_0} P \tag{10}$$

Where d is the ferroelectric film thickness. This indicates that when ferroelectric film thickness is reduced to the range of λ_{eff}, the high depolarizing field could suppress the ferroelectricity. Figure 1.6 shows how the charges distribute for a perfect metal (Figure 1.6b) and how the charges distribute, and the voltage and electric field profiles at the electrodes when they are real metals (Figure 1.6 right panels) [21].
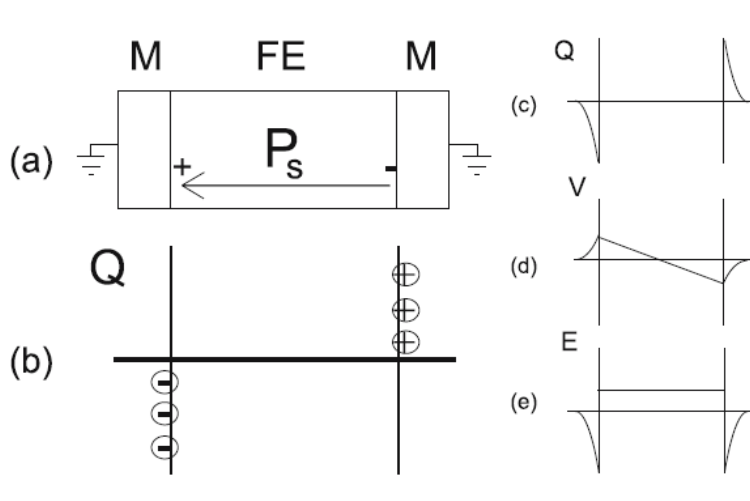
Figure 1.6: a) Scheme of a metal/ferroelectric/metal system with the ferroelectric spontaneously polarized with a homogeneous polarization Ps. b) Scheme of the charge distribution for perfect metallic electrodes. c), d) and e) charge distribution, voltage and electric field profiles for realistic metallic electrodes. From Dawber et al. [21]

2.4 Giant Electroresistance in FTJs

Zuravlev proposed a theoretical model in 2006 [22], considering screening of the polarization charges in metallic electrodes and direct quantum tunneling across a ferroelectric barrier. They calculated the change in the tunneling conductance associated with the polarization switching.

The reversal of the electric polarization in the ferroelectric produces a change in the electrostatic potential profile across the junction, as seen in Figure 1.6d. This leads to a resistance change of a few orders of magnitude when the metal electrodes have significantly different screening lengths, a phenomenon called Giant Electroresistance Effect (GER).

The physical mechanism responsible for this effect is the change of the electrostatic potential profile $\varphi(z)$ induced by the reversal of the electric polarization in the ferroelectric. In the ferroelectric, the surface charges are not completely screened by the adjacent metals and therefore the depolarizing field E in the ferroelectric will be not zero. The electrostatic potential associated with this field depends on the direction of the polarization. This leads to an asymmetric potential profile for the two different polarization directions and is the origin of the GER effect.
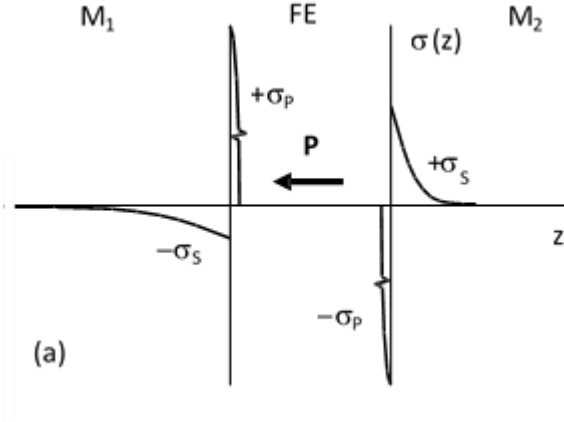
Figure 1.7: Scheme of the charge distribution along the two metals M1 (with a large screening length) and M2 (with a short screening length) that compose a ferroelectric tunnel junction.

Considering a Ferroelectric film of thickness d, placed between two metals of infinite area. The polarization (assumed uniform) points to the direction perpendicular to the plane of the interface (z). Charge densities are created at the two interfaces of the ferroelectric: $\pm\sigma_P = \pm|P|$. The polarization charges are screened by the charges of the two electrodes, represented by the screening charge per unit area, $\mp\sigma_S$, as is shown in the Figure 1.7.

The following assumptions are in effect: the ferroelectric is perfectly insulator, so all the compensating charges come from the electrodes, and the FTJ is short circuited and connected to a low impedance source, which equalizes the electrostatic potentials of the two electrodes at infinity. According to the Thomas-Fermi model, the screening potential within metals 1 and 2 is given by:

$$\varphi(z) = \begin{cases} \dfrac{\sigma_S \delta_1 e^{-|z|/\delta_1}}{\varepsilon_0}, & z \leq 0 \\[4mm] -\dfrac{\sigma_S \delta_2 e^{-|z-d|/\delta_2}}{\varepsilon_0}, & z \geq d \end{cases} \tag{11}$$

Where δ_1 and δ_2 are the Thomas-Fermi screening lengths in the electrodes and σ_S is the magnitude of the screening charge per unit area, which is the same in the metals 1 and 2 due to the charge conservation. Since the electric field is constant inside the ferroelectric, the potential drop can be calculated as:

$$\varphi(0) - \varphi(d) = \frac{d(P - \sigma_S)}{\varepsilon_S}. \tag{12}$$

P is the absolute value of the spontaneous polarization of the material, and ε_s is the dielectric permittivity. This expression takes account of the induced component of the polarization resulting from the electric field present in the ferroelectric. Combining the eqs. (10) and (11):

$$\sigma_S = \frac{dP}{\varepsilon(\delta_1 + \delta_2) + d} \tag{13}$$

with $\varepsilon = \varepsilon_F / \varepsilon_0$.

For a good metal, δ_1 and δ_2 will be small, and $\sigma_S = P$, which implies no depolarizing field inside the ferroelectric. In the opposite limit, when the screening length tends to infinity, the depolarizing field increases to saturation at $E = -P/\varepsilon$.

Figure 1.8 shows the electrostatic potential of a junction composed of a ferroelectric with two metals with different screening lengths. The difference in the screening lengths leads to different absolute values of the electrostatic potential at the interfaces, φ_1 and φ_2, which makes the potential asymmetric. The switching of the polarization on the ferroelectric layer changes the potential profile from the solid line to the dashed one and changes the resistance of the junction.

In order to predict the resistance change associated with the polarization switching, it is assumed that the dominant mechanism is direct quantum mechanical electron tunneling across the barrier. The potential profile for the electrons is a combination of the electrostatic potential generated by the polarization, the electronic potential which determines the bottom of the bands in the two electrodes with respect to the Fermi energy (E_F), and the potential barrier created by the ferroelectric insulator. The barrier potential has a rectangular shape and a height U over the E_F.

The electronic potential is determined by the screening lengths, which are related to the Fermi wave vectors k according to the Thomas-Fermi theory, by:
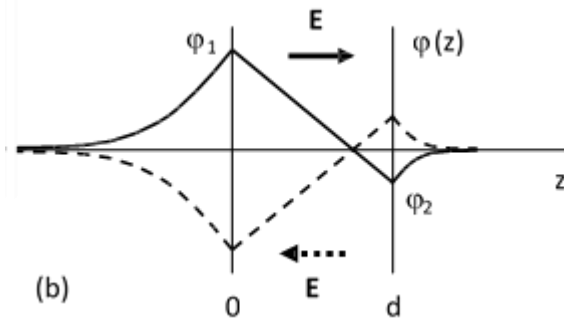
Figure 1.8: Distribution of the screening potentials across a ferroelectric tunnel junction with electrodes with different screening lengths.
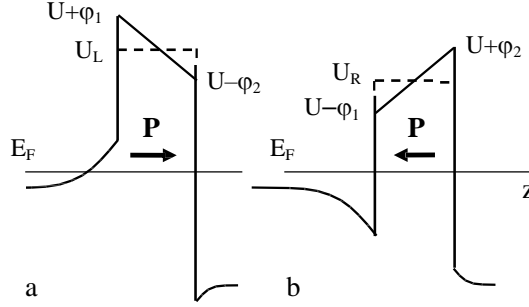
Figure 1.9: Barrier profile in a FTJ when ferroelectric polarization points towards the metal with (a) short and (b) large screening lengths

$$k_{1,2} = \frac{\pi a_0}{4\delta_{1,2}^2},$$
(14)

Where a_0 is the Bohr Radius. The resulting potential $V(z)$ for the two polarizations is shown in the Figure 1.9.

The difference between φ_1 and φ_2 controls the asymmetry in the potential profile which is decisive for the resistance change when the polarization switches. The average potential barrier height for polarization pointing to the left, $U_L = U + (\varphi_1 - \varphi_2)/2$, and is not equal to the average potential barrier height when the polarization pints to the right, $U_R = U + (\varphi_2 - \varphi_1)/2$. This produces a dramatic change in the resistance of the current across the ferroelectric tunnel barrier.

2.5 The role of Oxygen Vacancies in complex oxides doping

When considering screening charges (either to screen the ferroelectric polarization charges in a tunnel junction or to screen the ionic charges of a polarized ionic liquid), oxygen vacancies (OV) are another mechanism to be considered. In complex oxides, oxygen vacancies generate free electrons via the reaction:

$$O_0 \rightarrow \frac{1}{2}O_2 + V_o^{\cdot\cdot} + 2e^-$$
(15)

where O_o denotes an oxygen atom in its lattice position and $V_o^{\cdot\cdot}$ denotes a double positive charge oxygen vacancy. These carriers, further than screening the polarization charges, may influence the electrostatic boundary conditions, favoring one ferroelectric polarization over the other one. Furthermore, the ionization

process of OV may have an important role in the doping mechanism of oxides, giving new perspectives in the realm of controlled phase transition of correlated oxides.

2.6 La$_{1-x}$Sr$_x$MnO$_3$

Lanthanum-Strontium manganite La$_{1-x}$Sr$_x$MnO$_3$ (LSMO) is a well-known oxide characterized by the possibility of providing spin-polarized currents at room temperature in some phases [23]. This system presents an interesting phase diagram with hole doping (Figure 1.10), including metal-to-insulator and magnetic transitions [24]. Also, the structure changes with doping: as shown by Urushibara et al. [7], the LSMO structure at room temperature is orthorhombic for *x* less than 0.175. At larger *x* it is rhombohedral, but in the *x* value range between 0.175 and 0.25 the rhombohedral structure appears as a result of the phase transition from the orthorhombic structure occurring with increasing temperature. For LSMO in the range from *x*=0.25 to x=0.5 the Curie temperature is virtually *x*-independent, being close to 350K. In particular we have worked with La$_{0.7}$Sr$_{0.3}$MnO$_3$, which has a Curie temperature of Tc=354K. For this Sr stoichiometry the saturation magnetization of the manganite is 3.7 μ_B/Mn$_{atom}$.

Regarding the transport properties of the lanthanum manganites, resistivity vs. temperature curves are presented in Figure 1.10 (Right) adapted from [7]. We can observe that for x=0.3 the resistivity at low temperatures is of the order of ρ=10^{-4}
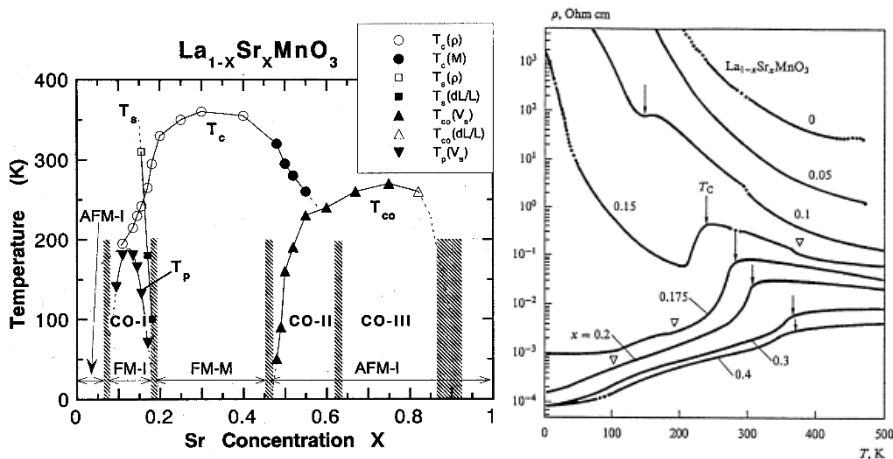
Figure 1.10: Left: Phase diagram of La$_{1-x}$Sr$_x$MnO$_3$. Adapted from [24]. The acronyms AFM, FM, I and M denote antiferromagnet, ferromagnet, insulator and metal, respectively. Also CO (I, II and III) denotes the three types of charge orderings in the compound. Right: Resistivity as a function of temperature for different Sr concentration in La$_{1-x}$Sr$_x$MnO$_3$. Arrows indicate the Curie temperature for each compound. Adapted from [7].

$\Omega\cdot$cm, which correspond to the conductive values of a degenerate semiconductor or a *poor* metal.

Another important property of LSMO is that is a Half-Metal at low temperatures, as discussed in [23]. A half-metal is a material exhibiting, at low temperatures, metallic behavior for one electron spin polarization and insulating behavior for the other spin polarization. In consequence, the electronic density of states is 100% spin polarized at the Fermi level.

2.7 BaTiO$_3$

Barium titanate BaTiO$_3$ (BTO) is a band-gap insulator which presents ferroelectric behavior below its Curie temperature Tc=393K, where it suffers a phase transition from a Paraelectric to a Ferroelectric. The phase transition is accompanied by a structural transition from cubic to tetragonal (both perovskite structures). The ferroelectric polarization appears when Ti^{4+} ions move from their high symmetry position in the center of the oxygen octahedra. This generates a finite dipolar moment with a saturation polarization of P$_S$=33 μC/cm^2 [25].

The ferroelectric state in BTO is so stable that it can support the electron doping even with carrier densities reaching values above the critical concentration n$_c$=10^{21} cm^{-3}, when BTO becomes metallic [26]. This is because itinerant electrons, instead of destroying ferroelectricity due to their screening of the long-range Coulomb interactions, screen the strong crystal field interactions caused by oxygen vacancies. The possibility of combining the resilient ferroelectric behavior with a MIT opens a novel field of research in order to benefit from the use of doped ferroelectrics in the fabrication of electronic devices.

2.8 La$_{1-x}$Sr$_x$CuO$_{2.5-\delta}$

High critical-temperature superconductivity was discovered in cuprates in 1986 [27], and it marked an inflection point in the relevance of complex oxides in materials science. Interestingly, in these materials, energy bands are such that the difference between the levels of the oxygen and the metal is very small. This highlights the important role oxygen plays in the electric conduction of the system, almost equal to the relevance of copper in these structures. In these systems, superconductivity comes from the doping of the CuO$_2$ planes with electrons coming from the "charge reservoir" layers, typically when the doping level reaches one electron per Cu site. The electronic density may be modified with the addition or suppression of oxygen ions from the system.

Lanthanum-strontium cuprate $La_{1-x}Sr_xCuO_{2.5-\delta}$ (LSCO) was first synthesized in 1998 [28] and is a metallic, but not superconducting cuprate, which accommodates a wide range of oxygen stoichiometries. As oxygen vacancies concentration varies, the band structure evolves from metallic when there are no oxygen vacancies, to insulating (due to the opening of a Hubbard gap) when OV concentration raises to 0.5 per Cu site. This system has a similar structure to other superconducting cuprates with CuO_2 planes, but the oxygen vacancies channels present along the a and b crystallographic axes break the connectivity of oxygen octahedra, impeding the superconductivity in this compound. As has been observed in similar cuprates like $La_{2-x}SrCuO_4$, hole doping beyond a certain limit suppresses superconductivity unless the system is able to generate oxygen vacancies to compensate the charge [29].

3. Introduction to Quantum Materials

As has been already mentioned, in solids, electrons have several degrees of freedom, including charge, spin and orbital. In addition, considerations of topological nature should be taken into account, ultimately linked to the phase of the wavefunctions, determined in turn by the interatomic potentials and the crystal structure. The behavior of some materials under certain conditions can only be explained by considering the correlations between all the above-mentioned degrees of freedom, defining their electrical, magnetic, optical, mechanical and thermal properties (Figure 1.11). These materials are known as quantum materials, and the collective electronic properties that are not present in individual electrons are called emergent [30] and are the responsible for various macroscopic quantum phenomena like metal/insulator transition (MIT) or superconductivity.

3.1 Metal-insulator transition in correlated electronic systems

The metal-insulator transition is one of the most important properties in quantum materials. Its origin can be diverse but is usually related to electron-electron interactions (and if this is the case, called Mott transition), which has already been briefly discussed earlier in this Introduction. This MIT can be very useful for the developing of electronic devices, providing gigantic and ultrafast switching of various physical properties, not only electrical but also magnetic, optical, etc.

From this perspective of device operability, the MIT can be classified into two types, according to the approach followed to achieve the transition: *bandwidth control of the MIT*, which changes the electronic correlations by changing the ratio between the electron correlation energy (U) and the one-electron bandwidth (W); and *band-*
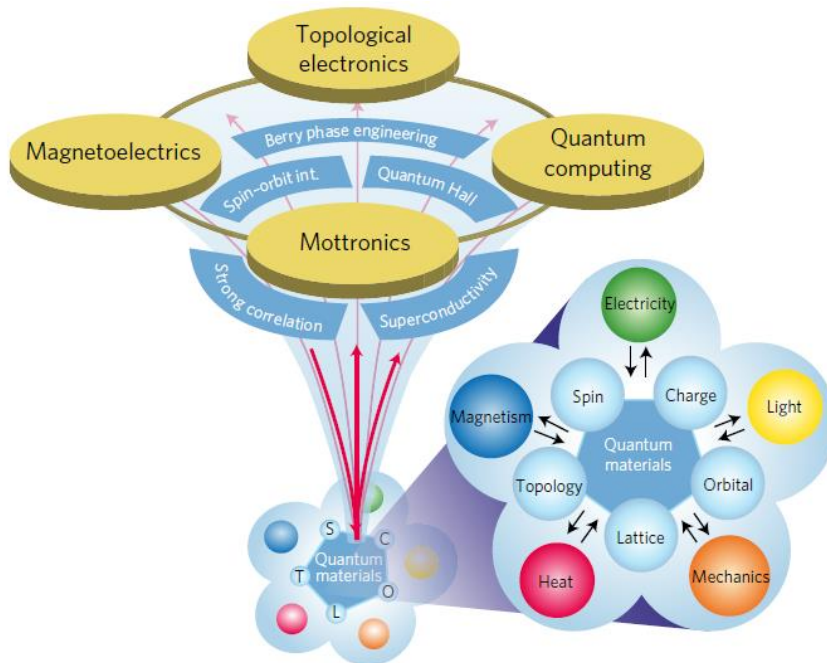
Figure 1.11: The bottom pentagon shows the different degrees of freedom of strongly correlated electrons in solids, and the different external stimuli that make the system respond collectively. The top scheme shows the variety of emergent functions coming from the electronic correlations, and the different future applications of these quantum materials. Adapted from [30].

filling control, which changes the number of electrons in the system by chemical or electrostatic doping. The bandwidth can be changed via modification of the bonding angle between the transition metal and the surrounding oxygens.

The correlation between charge, spin and orbital in electrons plays an important role in the MIT, particularly in *d*-electron compounds, like $SrIrO_3$. In case of half band filling (or fractional states), correlations can lead to an insulating groundstate in the system associated to a charge localization. A process that may be followed by an ordering in spin or orbitals.

Thus, MIT materials can be used in integrated circuits as non-volatile memories called Resistance Random Access Memories (ReRAM), which memorize the information in the resistance state of each device cell (metallic or insulating) and can be rewritten many times. Expected advantages of ReRAM compared with flash memory include higher-density integration, higher access speed, and lower energy consumption [31,32]. One important consideration is that the injection or rejection of oxygen vacancies in the material can change band filling, triggering the MIT and, with it, the enormous resistance switching observed for some transition-metal oxides, like manganites [33].

The ReRAM structures are now being commercialized as an intermediate step between the high-speed but low-density Dynamic RAM, and the low-speed and high-density storage HDDs. Quantum materials and its "emergent" properties portfolio are the most promising systems to solve one of the major issues in technology, the information storage problem.

3.3 Field effect transistor for Ionic Liquid Gating

Taking into account all the possible functions of the MIT in quantum materials, its electrical control is most useful. One common way to induce the transition and control the large change of the resistance is via carrier doping of the system. The tuning of the physical properties of electronic systems by controlling the carrier density has become an interesting phenomenon in condensed matter devices [34]. As can be seen in Figure 1.12 by varying the carrier concentration, new states of matter can be induced in complex oxides, moving from antiferromagnetic insulator to metal, or even superconductor states.

Different methods can be used to modify the carrier concentration of a solid material [35]. For example, chemical doping is an easy method. It consists on the replacement of one atom of the unit cell for another of different type, or in the addition of atoms to the unit cell, but not in the lattice sites. This type of doping introduces inevitable changes in the crystal structure, giving rise to a modification of the physical properties in a not-desired way. On the other hand, a purely electrostatic doping is achieved in the Field-Effect transistors (FET), which use an electric field in a gate to induce a carrier density by accumulation or depletion of charges at the surface of the material, underneath the gate. The principal advantage of using this concept is that the doping is reversible because the electric field can be turned on and off and can be applied in both directions. This makes this kind of devices a unique tool to control carrier density without generating structural or chemical disorder [36].

Field-Effect transistors are probably the most used devices in technology, and its principal application is to deal with digital signals forming the modern integrated circuits with over 10^7 devices. The device is based on regulating a conduction channel by an electric field between two terminals, source and drain (N doped) in a semiconductor (P doped). The channel is covered by an insulating dielectric film and a metal contact in a capacitor structure, forming the gate, as it is shown in the schematic representation of Figure 1.13. Applying a positive or negative voltage to the gate with respect to the semiconductor (usually shorted with the source) creates an accumulation of electrons or holes in the surface of the semiconductor, at the interface with the dielectric, in the channel region (N-type or P-type). In this way,
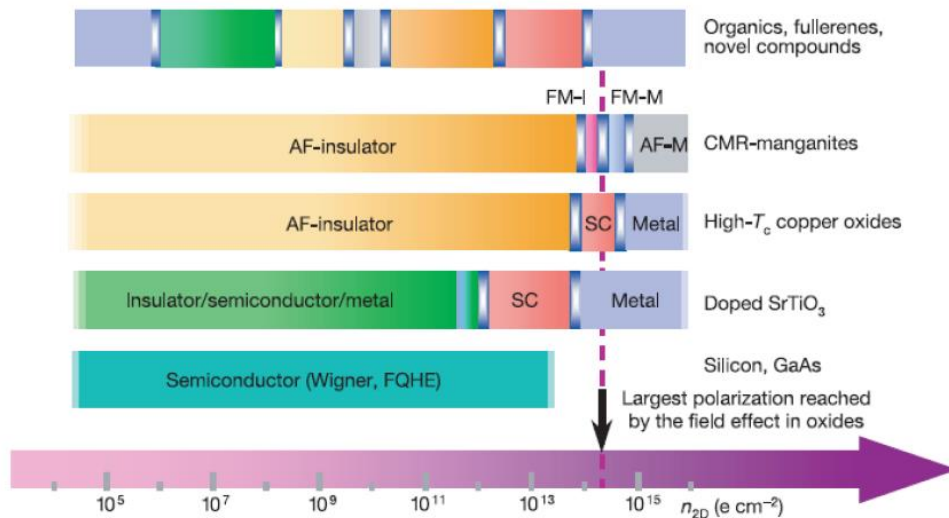
Figure 1.12: Phase diagram of different compounds at T=0K as a function of the 2-dimensional carrier density. Complex oxides as manganites or copper oxides have a very rich phase diagrams, crossing through different conducting and magnetic states with the increasing of carrier density. Adapted from [35]

one can increase or decrease the carrier concentration of the semiconductor, or the device material in general, and create a conduction path between the source and the drain. If the accumulated charges contribute to the conduction of the material, the channel resistance will decrease, and the current will flow through it. On the other hand, if the charges do not contribute to the conduction (for example, a hole doping in an n-type semiconductor), the conductivity of the device will be decreased.

If we could use the FET structure to modulate the carrier density of a correlated oxide, it will change not only its conductivity, but also its intrinsic properties, as shown in Figure 1.12. Looking into the numbers, typically a carrier density of 10^{15} e/cm^2 is needed for a CMR manganite to cross its phase transition boundary from antiferromagnetic insulator to metallic and ferromagnetic, or for HTc cuprates to reach the superconducting phase.

There are two ways of increasing the carrier density generated at the conductor's interface. The first one is to increase the carrier accumulation by inducing higher electric fields. However, when the electric field reaches values of 10^6 V/cm, electrical breakdown of the insulator takes place. The second way is to improve the geometric scaling of the channel reducing the thickness, which allows the enhancement of the accumulated charge while controlling the power dissipation. But the problem gets unsolvable when the size of the transistor reaches the nanometric length, in this range, it is difficult to manage leakage currents from gate to channel. Taking all the

25
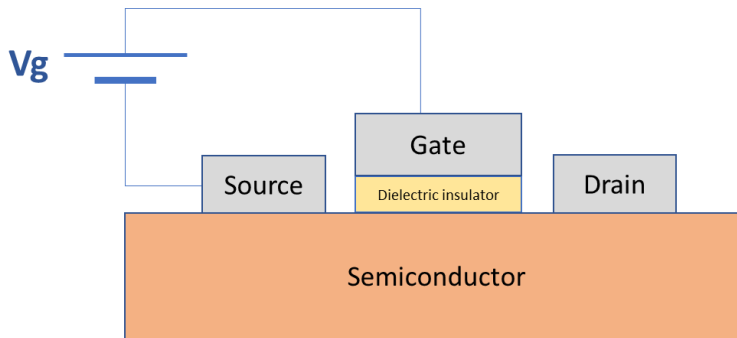
Figure 1.13: Schematic diagram of a semiconductor FET. The Source and the Drain are connected by a semiconductor, and the resistance of the system is controlled by the voltage applied between the source and the gate.

limitations into account, FET structures are limited to induce a carrier concentration of n=10^{13} cm^{-2}, an insufficient number to trigger a phase transition for most complex oxides. High-permittivity dielectrics as $SrTiO_3$, which is the substrate used to grow multiple oxides, can be used, reaching charge densities of $7 \cdot 10^{13}$ carriers/cm^2 [37]. An alternative is to use ferroelectric oxides as gate electrodes. Oxides as $BiFeO_3$ or $BaTiO_3$ present spontaneous polarization values of *ca*. 0.25 C/m^2, leading to possible charge transfers of 10^{14} carriers/cm^2. Although the ferroelectric polarization is remnant, so is not necessary to maintain the voltage applied once the polarization is set, the doping cannot induce the carrier density necessary to explore the whole phase diagram of complex oxides. A novel system capable of achieve higher carrier densities is the Electric Double Layer Transistor (EDLT), described in the next section.

In FET structures, the characteristic value of the accumulation and depletion layer thickness is controlled by the screening length, λ_{eff}, so that systems with low carrier density like semiconductors, will have large values of λ_{eff}. The carrier density decays exponentially inside the conductor over the Thomas/Fermi screening length, which value is [38]:

$$\lambda_{eff} = \left(\frac{\varepsilon_s \varepsilon_0 k_B T}{e^2 n_{eff}} \right)^{1/2} \tag{16}$$

Where ε_s is the dielectric constant of the semiconductor, ε_0 is the dielectric constant of the vacuum and n_{eff} is the density of electrons responsible for the screening of the electric field. In the case of complex oxides, n_{eff} is near 10^{15} carriers/cm^3 and therefore the screening length will be in the nanometric range.

3.4 Electric Double Layer Transistor

The Electric Double Layer Transistor (EDLT) solves the doping limitation of the FET, thanks to the use of a liquid dielectric for the gate, instead of a solid one. When a voltage is applied in the gate of an EDLT, the charge transfer achieved in these devices is around 10^{15} carriers/cm^2, which allows us to explore the varied phase diagrams of the TMO.

3.4.1 Ionic liquids

The liquid dielectric used in EDLT is a (room temperature) ionic liquid (IL), a molten salt composed generally by an organic cation and an inorganic anion. The electrons are completely bound to the molecules, therefore ILs show negligible electronic conductivity. The cation is very asymmetric causing that the combined structure is difficult to pack in a symmetric lattice, so they have unusually low melting temperatures compared to the normal salts like NaCl (800 C), and most of the ILs form glasses at low temperature. Typically, ILs are in liquid state at room temperature and exhibit a large ionic conductivity, and due to the Coulomb long-range interactions between ions, they have exclusive properties like very low vapor pressures. The ionic liquid mostly used in the gating of EDLT and consequently used in this work is the DEME-TFSI, specified in Figure 1.14.

N,N-diethyl-*N*-methyl-*N*-(2-methoxyethyl) ammonium, [DEME]$^+$

Bis(trifluoromethanesulfonyl)amide,[NTf$_2$]$^-$
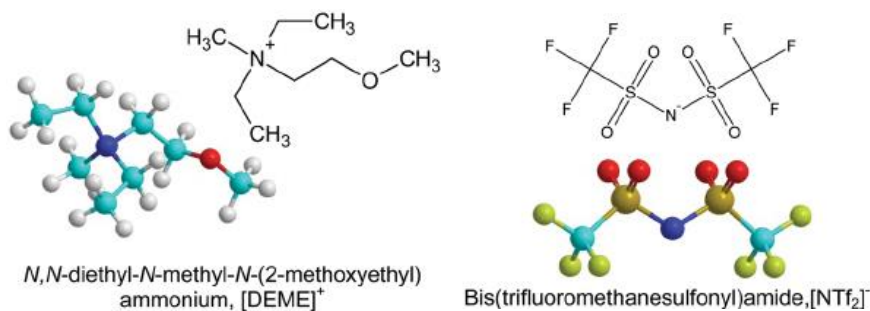
Figure 1.14: Structure of the positively (DEME) and negatively (TFSI) charged molecules of the ionic liquid DEME-TFSI

3.4.2 EDLT gating mechanism

In this device, the three terminals (source, drain and gate) and the surface of the conducting channel are submerged in an IL (Figure 1.15). When a positive voltage is applied between the material/source and the gate, anions will accumulate at the gate interface and cations will distribute over the channel surface. Correspondingly,

the channel will be doped with electrons in order to screen the electric field of the cations, forming the Electric Double Layer (EDL) of the device.

Just as in conventional FETs with solid dielectrics, in EDLT it is impossible to operate with an unlimited value of the gate bias. Increasing the voltage over a specific value, determined by the electrochemical stability window of the IL, electrochemical reactions occur. The redox potential between the ionic liquid and the channel material defines a range of gate doping of several Volts, limiting the maximum gate voltage and hence the maximum carrier tunability in the device.

3.4.2 Applications of Electric Double Layer Transistors

Ionic liquid gated EDLTs break the limit of the maximum accumulated carrier concentration until gate breakdown in conventional FET. The superior level of charge injection reached in EDLT makes this device a unique tool for many research areas [39], such as ferromagnetism, superconductivity, spintronics or mottronics. They proved to be essential to investigate electric field induced phenomena in a broad range of materials and probe correlated electron physics.

The first EDLT gate voltage conductance dependence and charge carrier modulation was achieved in the amorphous semiconducting InO_x in 2007 [40]. Also in 2007, Iwasa et al. were able to dope ZnO thin films, triggering a phase transition from semiconducting to metallic [41]. They used a (PEO) electrolyte as Ionic Liquid, and applying a positive bias, generated an accumulation of electrons up to 10^{13} cm^{-2}. In 2009 the experiment gave similar results with DEME-TFSI IL, but with a considerable higher carrier density generated ($5 \cdot 10^{14}$ cm^{-2}).
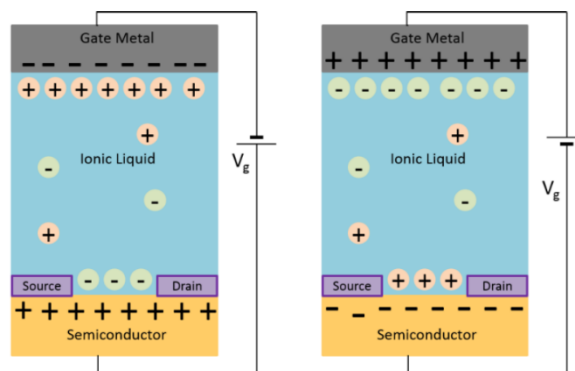

Figure 1.15: Diagram of an EDLT and the charges accumulation for a negative voltage (left) and positive voltage (right). For a negative (positive) voltage applied to the gate, the conducting channel will be doped with holes (electrons).

Several experiments have been performed with EDLT in order to explore phase transitions in complex oxides:

Superconductor to Insulator Transition:

The possibility to induce or destroy superconductivity just by applying electric field may be one of the most interesting applications in actual technology, especially in High-Tc superconductors like $YBa_2Cu_3O_7$. These systems are expected to experiment strong field-effects due to their low carrier density, which leads to an electric-field penetration depth of nanometers order.

Ueno et al. [42] first achieved a superconductor to insulator transition (SIT) using the EDLT technique in 2008. They reported electrostatic doping of $SrTiO_3$ (STO) single crystals that conduced to a 2-dimensional superconducting state below Tc=0.4K for an external applied voltage of 3.5V. The ionic liquid used was $KClO_4$/PEO.

In 2009, Ye et al. reported a SIT transition on atomically flat films of ZrNCl with Tc=15.2K and Vg=4V using an IL (DEME-TFSI) as gate dielectric of the EDLT. This result revealed the Electric Double Layer Transistor as a versatile tool for the induction of electronic phase transitions in superconductors.

In 2011, Bollinger et al. achieved a SIT on $La_{2-x}Sr_xCuO_4$, a high Tc superconductor, using an EDLT [43]. They were able to tune continuously the carrier density using the electric field effect, moving the critical temperature up to 30 K. They observed that the critical sheet resistance, $R_\square = \rho/d$ (being ρ the resistance of a single metallic layer of the cuprate and d the distance between metallic layers), was precisely the quantum resistance for electron pairs R_Q = h/4e^2 = 6.5 kΩ, suggesting that the phase transition was driven by quantum phase fluctuations and copper pair (de)localization. They also compared the critical sheet resistance of YCBO, obtaining the same value [44].

Metal to Insulator Transition:

Electrostatic control of MIT in solids is one of the most promising features for technology applications in recent years and works modulating the carrier concentration in materials with MIT using EDLTs are described below.

The first studies of the MIT were focused in comparing the effect of electron and hole doping in niquelates with respect to the same experiments with chemical doping [45]. Torrance et al. studied rare-earth niquelates $RNiO_3$ (being R a rare earth element), demonstrating that the radius of the R atoms controlled the tilting of NiO_6 octahedral, modifying the MIT temperature. The subsequent studies shown that

electrostatic doping [46,47] generated similar results in $NdNiO_3$ [48,49]. Furthermore, charge order effect observed in $NdNiO_3$ near the Mott transition may be important for understanding the nature of insulating state as well as interpreting the field effect results, because the gate-induced charges may distribute homogenously in charge ordered insulators at low temperatures [50].

Lee et al reported in 2011 EDLT measurements in $SrTiO_3$ thin films [51]. They measured the systematic decrease of the temperature of carrier freeze-out with increasing carrier concentration with the MIT disappearing when superconductivity appeared. In addition, a regime of anomalous Hall effect was found, suggesting magnetic ordering that is reminiscent of effects associated with quantum critical behaviors in some complex compounds.

In 2012, Nakano et al. studied VO_2 with EDLT, founding a MIT at 340K [52]. They demonstrated that the transition occurred due to the electrostatic charging at the material surface, driving the previously localized carriers in the bulk material into motion, and generating a 3-dimensional metallic state in the system. The voltage applied to the oxide was lower than 1 V.

In 2017, Groenendijk et al. [53] studied the MIT of $SrIrO_3$ with the variation of thickness, finding a correlated insulating state in the 2D limit. They also found a divergence in the relative susceptibility near the transition point, indicative of the opening of a Mott gap and the concomitant enhancement of magnetic order. The study of this system with electrostatic doping in EDLT is an attractive open problem.

3.5 $SrIrO_3$

Strontium Iridate $SrIrO_3$ (SIO) is a 5d transition metal oxide characterized by having the same energy scale for the Coulomb repulsion (U), the bandwidth (W) and the Spin-Orbit interaction (SOC), around 0.3 eV. The interplay between these features generate exotic electronic phases. This interplay can be modified controlling the W/U ratio, when W is smaller than U, the system is insulating. However, a MIT appears when W values are similar to U and the system becomes metallic. In 5d TMOs the orbitals are more extended than in 3d and 4d compounds, so W should be larger than U, but the bandwidth can be also controlled modifying the dimensionality of the system. SIO thin films experience the MIT for thicknesses under 2 nm. This insulating state should be a correlated state due to an anti-ferromagnetic state developed in the transition [53,54]. It is still not clear if the transition is driven by the interaction between electronic correlations and dimensionality or by the emergent magnetic state in the insulating phase. The

apparition of a ferromagnetic behavior in an insulating state would open the possibility to fabricate a Spin Orbit Mott insulator.

4. References

[1]   S. Maekawa, T. Tohyama, S. E. Barnes, S. Ishihara, W. Koshibae, and G. Khaliullin, *Physics of Transition Metal Oxides* (Springer Berlin Heidelberg, Berlin, Heidelberg, 2004).

[2]   Y. Tokura, Phys. Today **56**, 50 (2003).

[3]   M. Imada, A. Fujimori, and Y. Tokura, Rev. Mod. Phys. **70**, 1039 (1998).

[4]   R. J. Cava, J. Am. Ceram. Soc. **83**, 5 (2000).

[5]   J. Hemberger, A. Krimmel, T. Kurz, H.-A. Krug von Nidda, V. Y. Ivanov, A. A. Mukhin, A. M. Balbashov, and A. Loidl, Phys. Rev. B **66**, 094410 (2002).

[6]   Y. Tokura, Reports Prog. Phys. **69**, 797 (2006).

[7]   A. Urushibara, Y. Moritomo, T. Arima, A. Asamitsu, G. Kido, and Y. Tokura, Phys. Rev. B **51**, 14103 (1995).

[8]   H. Y. Hwang, Y. Iwasa, M. Kawasaki, B. Keimer, N. Nagaosa, and Y. Tokura, Nat. Mater. **11**, 103 (2012).

[9]   P. W. Anderson, Science (80-.). **177**, 393 (1972).

[10]   A. Manchon, H. C. Koo, J. Nitta, S. M. Frolov, and R. A. Duine, Nat. Mater. **14**, 871 (2015).

[11]   J. Hubbard, Proc. R. Soc. London. Ser. A. Math. Phys. Sci. **276**, 238 (1963).

[12]   J. M. D. Coey, M. Viret, and S. Von Molnár, Adv. Phys. **48**, 167 (1999).

[13]   J. G. Simmons, J. Appl. Phys. **34**, 238 (1963).

[14]   W. F. Brinkman, R. C. Dynes, and J. M. Rowell, J. Appl. Phys. **41**, 1915 (1970).

[15]   H. Schmid, J. Phys. Condens. Matter **20**, (2008).

[16]   M. Julliere, Phys. Lett. A **54**, 225 (1975).

[17]   R. E. Cohen, Nature **358**, 136 (1992).

[18]   R. E. Cohen, *Ferroelectricity: The Fundamentals Collection* (2005).

[19]   H. D. Megaw, Acta Crystallogr. **5**, 739 (1952).

[20]   E. Y. Tsymbal and H. Kohlstedt, Science (80-.). **313**, 181 (2006).

[21]   M. Dawber, P. Chandra, P. B. Littlewood, and J. F. Scott, J. Phys. Condens. Matter **15**, (2003).

[22]   M. Y. Zhuravlev, R. F. Sabirianov, S. S. Jaswal, and E. Y. Tsymbal, Phys. Rev. Lett. **94**, 1 (2005).

[23]   J. H. Park, E. Vescovo, H. J. Kim, C. Kwon, R. Ramesh, and T. Venkatesan, Nature **392**, 794 (1998).

[24]   H. Fujishiro, T. Fukase, and M. Ikebe, J. Phys. Soc. Japan **67**, 2582 (1998).

[25]   J. J. Wang, F. Y. Meng, X. Q. Ma, M. X. Xu, and L. Q. Chen, J. Appl. Phys. **108**, (2010).

[26]   T. Kolodiazhnyi, M. Tachibana, H. Kawaji, J. Hwang, and E. Takayama-Muromachi, Phys. Rev. Lett. **104**, 1 (2010).

[27]   J. G. Bednorz and K. A. Müller, Zeitschrift Für Phys. B Condens. Matter **64**, 189 (1986).

[28]   J. B. Torrance, Y. Tokura, A. Nazzal, and S. S. P. Parkin, Phys. Rev. Lett. **60**, 542 (1988).

[29]   J. B. Torrance, Y. Tokura, A. I. Nazzal, A. Bezinge, T. C. Huang, and S. S. P. Parkin, Phys. Rev. Lett. **61**, 1127 (1988).

[30]   Y. Tokura, M. Kawasaki, and N. Nagaosa, Nat. Phys. **13**, 1056 (2017).

[31]   A. Sawa, Mater. Today **11**, (2008).

[32]   R. Waser and M. Aono, Nat. Mater. **6**, 833 (2007).

[33]   S. Q. Liu, N. J. Wu, and A. Ignatiev, Appl. Phys. Lett. **76**, 2749 (2000).

[34]   D. W. Greve, *Field Effect Devices and Applications: Devices for Portable Low Power, and Imaging Systems* (1998).

[35]   C. H. Ahn, J. M. Triscone, and J. Mannhart, Nature **424**, 1015 (2003).

[36]   B. E. N. G. Streetman and S. K. Banerjee, *Solid State Electronic Devices* (1972).

[37]   D. Matthey, N. Reyren, J. M. Triscone, and T. Schneider, Phys. Rev. Lett. **98**, 1 (2007).

[38]   X. Guo and R. Waser, Prog. Mater. Sci. **51**, 151 (2006).

[39]   R. Kötz and M. Carlen, Electrochim. Acta **45**, 2483 (2000).

[40]   R. Misra, M. McCarthy, and A. F. Hebard, Appl. Phys. Lett. **90**, 3 (2007).

[41]   H. Shimotani, H. Asanuma, A. Tsukazaki, A. Ohtomo, M. Kawasaki, and Y. Iwasa, Appl. Phys. Lett. **91**, 2007 (2007).

[42]   K. Ueno, S. Nakamura, H. Shimotani, A. Ohtomo, N. Kimura, T. Nojima, H. Aoki, Y. Iwasa, and M. Kawasaki, Nat. Mater. **7**, 855 (2008).

[43]   A. T. Bollinger, G. Dubuis, J. Yoon, D. Pavuna, J. Misewich, and I. Božović, Nature **472**, 458 (2011).

[44]   G. Dubuis, A. T. Bollinger, D. Pavuna, and I. Božović, J. Supercond. Nov. Magn. **26**, 749 (2013).

[45]   J. B. Torrance, P. Lacorre, A. I. Nazzal, E. J. Ansaldo, and C. Niedermayer, Phys. Rev. B **45**, 8209 (1992).

[46]   S. Asanuma, P. H. Xiang, H. Yamada, H. Sato, I. H. Inoue, H. Akoh, A. Sawa, K. Ueno, H. Shimotani, H. Yuan, M. Kawasaki, and Y. Iwasa, Appl. Phys. Lett. **97**, 3 (2010).

[47]   Z. Yang, Y. Zhou, and S. Ramanathan, J. Appl. Phys. **111**, 1 (2012).

[48]   S. W. Cheong, H. Y. Hwang, B. Batlogg, A. S. Cooper, and P. C. Canfield, Phys. B Phys. Condens. Matter **194**–**196**, 1087 (1994).

[49]   J. L. García-Muñoz, M. Suaaidi, M. J. Martínez-Lope, and J. A. Alonso, Phys. Rev. B **52**, 13563 (1995).

[50]   U. Staub, G. I. Meijer, F. Fauth, R. Allenspach, J. G. Bednorz, J. Karpinski, S. M. Kazakov, L. Paolasini, and F. d'Acapito, Phys. Rev. Lett. **88**, 4 (2002).

[51]   Y. Lee, C. Clement, J. Hellerstedt, J. Kinney, L. Kinnischtzke, X. Leng, S. D. Snyder, and A. M. Goldman, Phys. Rev. Lett. **106**, 1 (2011).

[52]   M. Nakano, K. Shibuya, D. Okuyama, T. Hatano, S. Ono, M. Kawasaki, Y. Iwasa, and Y. Tokura, Nature **487**, 459 (2012).

[53]   D. J. Groenendijk, C. Autieri, J. Girovsky, M. C. Martinez-Velarte, N. Manca, G. Mattoni, A. M. R. V. L. Monteiro, N. Gauquelin, J. Verbeeck, A. F. Otte, M. Gabay, S. Picozzi, and A. D. Caviglia, Phys. Rev. Lett. **119**, 2 (2017).

[54]   P. Schütz, D. Di Sante, L. Dudy, J. Gabel, M. Stübinger, M. Kamp, Y. Huang, M. Capone, M. A. Husanu, V. N. Strocov, G. Sangiovanni, M. Sing, and R. Claessen, Phys. Rev. Lett. **119**, 1 (2017).

Chapter 2: Experimental Techniques

1. Samples growing: Sputtering system

The complex oxides samples fabricated in this thesis were grown using a high pressure sputtering system (Figure 2.1), which has proven to be an appropriate technique for the growth and fabrication of complex oxides [1]. The system was installed in "CAI de técnicas físicas UCM". The method consists on separate atoms from targets stoichiometrically made of the growing compound, using oxygen as the sputtering element. The extracted atoms deposit on a substrate placed on a heater plate in front of the targets. The growth takes place inside a vacuum chamber, where a previous vacuum of 10^{-6} mbar is achieved. The vacuum process consists of two stages:

1. Pre-vacuum with a membrane pump. With this method the chamber can reach a pressure of 10^{-1} mbar.

2. High vacuum. A pressure of 10^{-6} mbar is reached using a turbo-molecular pump supported by the membrane pump. After the cleaning process, the turbo-molecular pump is switched to "low speed" mode, in order to stabilize the growing pressure, 3.2 mbar of pure O_2.
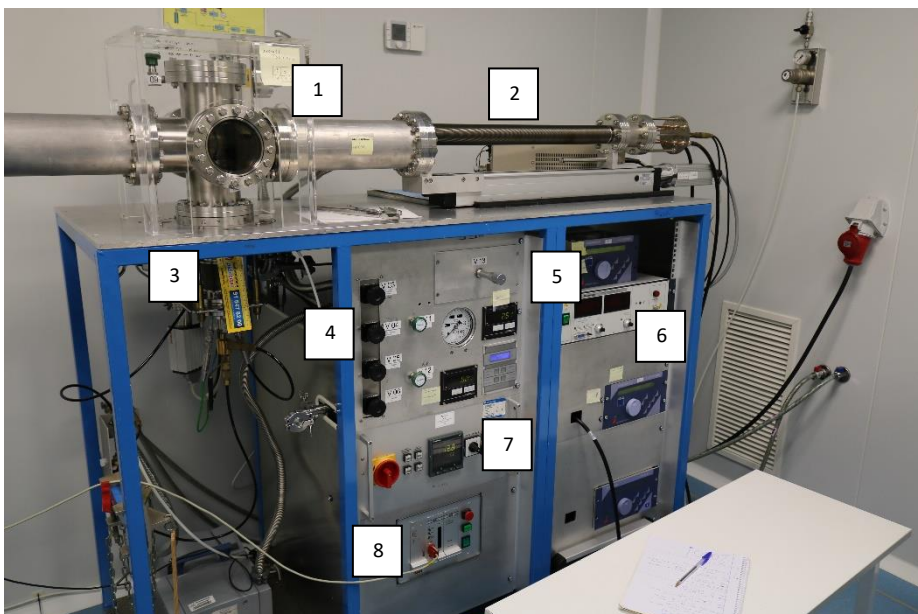

Figure 2.1: Image of a high-pressure sputtering system. 1: Vacuum chamber. 2: Remote controlled mobile arm. 3: Heater plate. 4: Pressure control valves. 5: Pressure meters. 6: Radiofrequency sources. 7: Heater plate controller. 8: Mobile arm controller.

A constant oxygen flow is injected and controlled with high precision needle valves. The pressure control is important since the sputtering rate depends on the energy of the incoming O_2 ions and also on the target atomic components. There exist several parameters which modify the deposit rate and the samples quality apart from the O_2 pressure in the chamber, such as the substrate temperature, the applied RF power or the annealing conditions.

The RF power is used instead of DC to limit the charge accumulation at the surface when the target is insulating. When the RF power is applied, the oxygen ions get attracted by the electric field towards the target, forming a plasma (Figure 2.2) and sputtering atoms from the surface. The extracted atoms deposit on the surface of the substrate. The high pressure of oxygen has three principal functions: To thermalize homogeneously the deposited atoms, to prevent the back-sputtering and to avoid the loss of oxygen in the crystal structure. All these conditions favor low sputtering rates (<1nm/min). Furthermore, the substrate temperature during the growing process is 900ºC (for LSMO and BTO), 750ºC (for LSCO) or 650ºC (For SIO), depending on the target, which permits diffusion of the ions along the surfaces, favoring the epitaxial growth. To preserve the oxygen stoichiometry, the chamber is oxygenated at 800ºC with 900 mbar of O_2, and the 1-hour annealing is made at 750ºC. An extra annealing of 15 minutes at 550ºC was made to the heterostructures and single layers of LSCO in order to optimize its transport properties.

For the deposition of metals, a DC magnetron sputtering was used. In this system, the plasma is confined close to the target using a magnetron which is composed by two concentric magnets that create a magnetic field whose lines close on the target. The electrons, by the Lorentz force, cover an helicoidal trajectory guided by the

Figure 2.2: Oxygen plasma formed around a complex oxide target.

magnetic field lines, generating a higher electron density closer to the target. The system was used for the non-epitaxial deposition of metals at room temperature. The driving gas used is Ar and the deposition is produced at high vacuum (10^{-3} mbar). The sputtering was used for the deposition of gold over the *tunnel-junction* and *Hall-bar* samples.

2. Structural characterization

X-Ray diffraction (XRD) and reflectivity (XRR) patterns are very helpful techniques to determine the thickness, composition and structural quality of single layers and heterostructures. The measurements have been performed at "CAI de difracción de rayos X at UCM", and the equipment used is a Philips X`pert MRD diffractometer with a Cu tube as X-Ray source operating at 45kV and 40 mA. The radiation energy is selected by using a monochromator made from silicon. It has high energy resolution (1 eV – 10 KeV). The selected energy in our case is the Cu Kα_1 (λ=0.15418 nm).

2.1. X-Ray diffraction

X-Ray diffraction is a non-destructive technique that allows us to infer the thickness, crystalline quality and lattice parameter of compounds. The separation between planes in a crystal is *d*. When the X-Rays are reflected in the specular direction, their interference will be modulated by this *d* parameter. The path difference between two consecutive planes is *2d·sin*θ, being θ the angle between the incident and the reflected beams (Figure 2.3). The interference will be constructive if the difference of path is an integer multiple of the wavelength, according to Bragg´s law [2,3]:

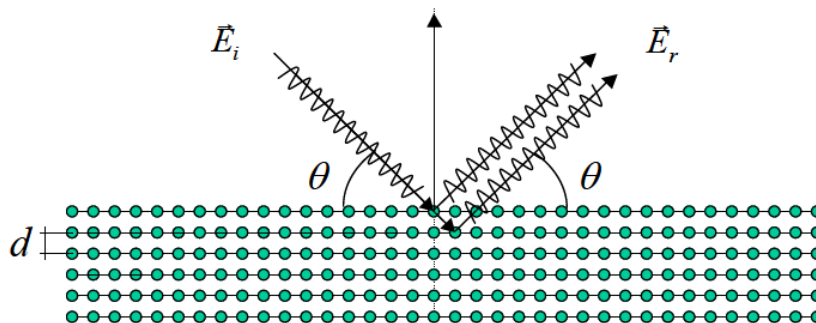$$2d_{hkl} \sin \theta = n\lambda_x \qquad (17)$$

Figure 2.3: Bragg´s reflection of a family of crystallographic planes. The separation between consecutive planes is d and the incident angle is θ.

Where d_{hkl} is the distance between planes of a family with indexes {hkl}. N is an integer number which represents the reflection order. Braggs´s law can be used for determining the lattice parameter in the out of plane direction, c. The diffraction scan is carried out in θ-2θ geometry (Figure 2.4).

In the case of multilayers measurements, the characteristic lengths scales are the lattice parameters of each material plus the modulation wavelength Λ, which is the thickness of the complete structure. This additional periodicity will form new diffraction peaks, which can be used to obtain the average lattice constant d, from [4]:

$$2\frac{\sin\theta}{\lambda_x} = \frac{1}{\bar{d}} + \frac{m}{\Lambda}$$

(18)

Where m is an integer used for labeling the order of the satellite peaks around the main bragg peak, and $\bar{d} = \Lambda/(N_A + N_B)$, being N_A and N_B the number of atomic planes of the materials A and B in the bilayer. This method is used in superlattices and is an accurate method for thickness calibration.
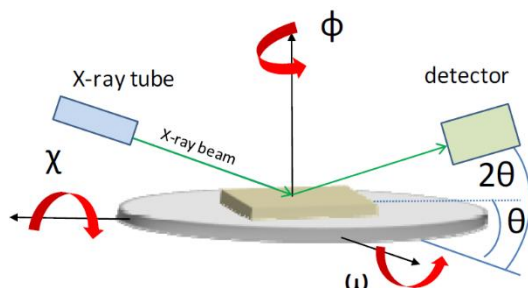
Figure 2.4: Schematic diagram of the θ-2θ geometry for x-ray diffraction

2.2. X-Ray reflectivity

In Bragg geometry, at θ values below the critical angle of the material, total internal reflection of the radiation takes place. Above the critical angle, the radiation is probing and being scattered by the electronic distribution deeper into the material. Large spacings, corresponding to the layer interfaces, which are much larger than interplanar lattice distances, give rise to oscillations in the reflected intensities. For the analysis, we consider the beam will travel a larger distance inside the material than the spacing between the crystallographic family planes of the material (*d*). In these conditions, the measurements will be sensitive to the refractive index of the material and therefore, to the composition. The different refractive indexes of
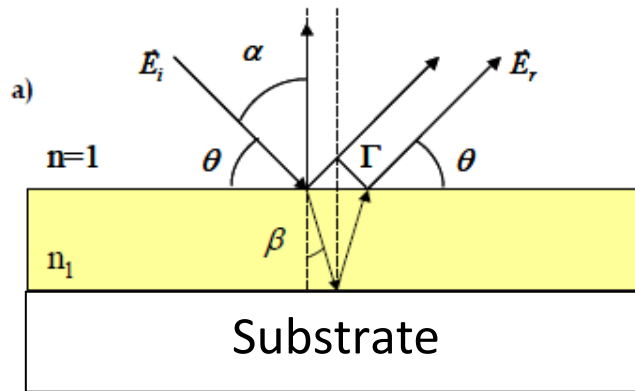
Figure 2.5: Scheme of the low angle reflectivity in a single layer. θ is the incident angle, β is the refracted angle and Γ is the path difference between the reflected and the refracted beam when both escape the thin film.

successive layers induce a change in the path length of the beam, favoring a constructive or destructive interference of the reflected beams.

When the radiation beam reaches the surface, part of it is reflected and the rest penetrates the sample until is reflected at the interface with the substrate. This beam crosses the film again and escapes at the surface (Figure 2.5). As a result of this process, oscillations from the interference appear in the reflectivity pattern. A maximum will appear when the optical path difference is an entire multiply of the X-Rays wavelength:

$$\Gamma = 2n_1 d \cos\beta = m\lambda_x \tag{19}$$

Where Γ is the path difference, n_1 is the refractive index of the thin film, d is the layer thickness, β is the refraction angle and λ_x is the wavelength of the incident radiation. The period of the oscillations is inversely proportional to the thickness of the sample. So, knowing the angular position of the maxima (or the minima), we can infer the thickness of the thin film:

$$\sin^2\theta = \left[\frac{(n-k)\lambda_x}{2d}\right]^2 + 2\delta \tag{20}$$

where k=0 for minima and k=1/2 for maxima, and (1-δ) is the real part of the refraction index.

2.3. Atomic Force Microscopy (AFM)

Atomic force microscopy (AFM) is currently the most used technique in the scanning probe microscopy family. The AFM has two principal advantages over other microscopy techniques. The first one is that do not require special environmental conditions for functioning. The second one is the high resolution, the order of sub-nanometer in the vertical direction and tens of nanometers in the lateral direction. The technique is based on the movement of a probe, consisting on a sharp tip placed at the end of a cantilever, over the surface of the sample. When the tip approximates to the surface, the cantilever feels the forces between sample and tip. For very short distances, inferior to 10Å, the force between atoms is repulsive following a Lennard-Jones potential and avoids the contact between particles. For larges distances (10-200Å), the force becomes attractive due to the predominance of the Van der Waals force.

By scanning the tip over the surface, the vibration of the cantilever is proportional to the topography. The cantilever´s deflection can keep either the distance to the surface or the contact force constant (depending on the mode used) while moving the tip. The cantilever deflection is measured reflecting a laser light on the back of the cantilever, which is collected by the photodetector.

The most used mode of the AFM is the *tapping* mode. The operation mode consists on scan the probe across the surface while the cantilever is oscillating. It oscillates at a frequency near its resonance frequency, with a variable amplitude around 50nm. Variations in the surface topography modify the oscillation frequency, and this variation is collected by the photodetector, which transforms it into an image of the surface.

All the AFM measurements in this work were performed at the "Instituto Nacional de Microscopía Electrónica (CNME)"at UCM.

3. Scanning Transmission electron microscopy (STEM)

Scanning transmission microscopy (STEM), developed in 1938 by von Ardenne [5], is a proficient technique to study the atomic and electronic structure of complex oxides due to its high spatial and energy resolution (Angstrom and eV resolution) [6]. The system consists on a transmission microscope equipped with a system of deflection coils in order to scan the beam over the sample (Figure 2.6). This is a way to combine the high resolution of TEM with the capabilities of a scanning microscope. Thanks to the implementation of spherical aberration correction in the early 2000´s [7,8], high resolution images under the angstrom barrier were achieved.
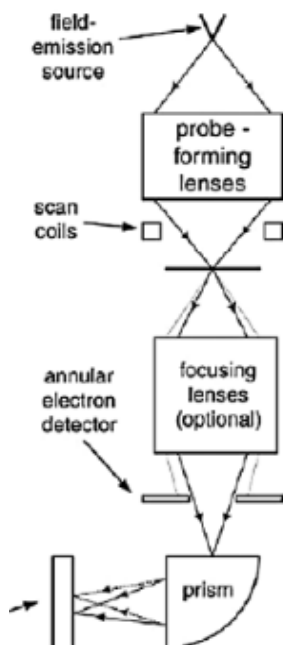
Figure 2.6: Represenation of a STEM system. Adapted from [6]

The operation of the system consists on the application of a high voltage (3-4kV) to the tip to extract the electrons. Once the electrons have been extracted, a second voltage is applied in order to accelerate them to the required energy and to focus the beam into an angstroms-diameter spot. After the gun, the condenser lenses form a demagnified image of the source. A set of coils composed by deflectors produce the shift of the beam to scan the sample surface.

One of the most useful techniques in STEM is the Z-Contrast. In this technique, a high angle annular dark field (HAADF) detector is installed for detecting electrons dispersed at high angles. These electrons come from an elastic scattering with atomic nuclei and carry information about the atomic number of the atom, generating an atomic distribution of the sample.

All the STEM measurements in this work were performed by Mariona Cabero and José María González-Calbet at the Instituto Nacional de Microscopía Electrónica (CNME)" at UCM, using a JEM ARM 200 cF aberration corrected.

3.1 Electron energy loss spectroscopy (EELS)

EELS technique analyzes the energy distribution of electrons that cross the sample vertically. With EELS we can obtain chemical and orbital information of samples,

measuring the part of the electrons that penetrate the sample and get inelastically scattered, transferring part of their energy to the sample [9].

The EELS spectrometer consists on a magnetic prism that deflects electrons with a concrete angle as a function of their energy. The deflected electrons reach to the dispersion plane, where they are collected by the photodiode.

From the EEL spectrum we can obtain information about the elastic scattering, which embraces the electrons that have gone through the sample without losing energy, and also about the inelastic scattering coming from the interaction between electrons and nuclei. The important part of the spectrum are the *white lines*, typical from transition metals. These lines come from internal transitions between the *2p* and the *3d* levels [6]. The *white lines* appear in pairs separated by a few eV because, due to the spin-orbit coupling, the L level divides into two levels, L_2 and L_3, and the M levels (from rare earths) into M_4 and M_5. Furthermore, the ratio between the two *white lines* is proportional to the oxidation state of the analyzed element. The EELS spectra are very sensitive to the oxides thickness, so is important to normalize the measurements with respect to it [10].

4. X-Ray Magnetic Circular Dichroism (XMCD)

X-Ray magnetic circular dichroism (XMCD) spectroscopy is a technique that uses high energy X-rays to explore the structural and magnetic properties of materials. The technique was proposed by Erksine et al. [11] in 1975 and developed by Müller et al. [12] in 2002. The principal advantage over the traditional magnetic techniques is that is element specific. XMCD permits to determinate spin and orbital magnetic moments and their anisotropies. An XMCD experiment typically is performed at a High Energy electron accelerator installation and consists on illuminate the sample with circularly polarized x-Rays with the energy of the absorption edge of a specific element. The dichroism signal consists on the difference between left and right circularly polarized x-ray absorption cross section. This dichroism signal is directly proportional to the macroscopic magnetic moment of a ferromagnetic or ferrimagnetic material.

4.1. X-Ray absorption Spectroscopy (XAS)

X-Ray absorption spectroscopy studies the effect of photon absorption in the matter. This process is not necessarily dependent on the spin of the incident photon. When the photon impacts with an atom, it is absorbed, giving rise to a transition of an electron from a low energy state to an empty state above the Fermi level, only if the energy of the photon is equal or higher than the energy of the empty level. The absorption pattern depends on the energy of the incident photon and on the
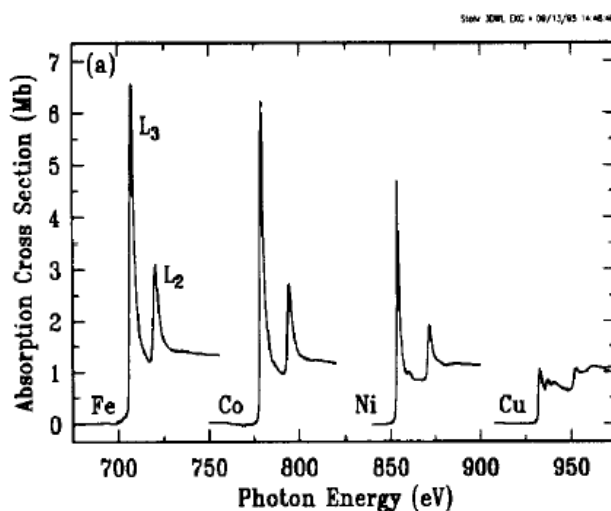
Stohr JOUR. DXC • 08/13/93 14:46:46

Figure 2.7: X-Ray absorption spectra near the L₂ and L₃ for different elements: Fe, Co, Ni and Cu. In the Cu edge L₂ and L₃ lines are not appreciated. Adapted from [14]

absorption edge of the measured element [13,14]. When the photon energy exceeds the absorption edge of the element, a peak in the absorption intensity is observed (Figure 2.7). The excited photoelectrons leave a hole in the core, generating an instability in the atom. Electrons are transferred to the inner levels emitting characteristic X-Rays in the process. The energy of these x-rays corresponds to the energy difference between the two corresponding shells. The *Fluorescence Yield* (FY) mode consists on the detection of these x-rays. The secondary emitted X-rays can promote additional electronic transitions. When a vacancy is generated in the L-shell, and electron from the M or N-shell decays to occupy the hole, emitting x-rays again (Figure 2.8). Normally the x-rays have enough energy to excite a core level to an unoccupied state above the Fermi level, because transition metals have the d-orbitals partially filled and close to the Fermi energy.

On the other hand, if the x-ray energy is absorbed by one of the outer electrons, it will be ejected from the atom. This is called an *Auger electron*. So, the complete energy absorption spectrum will consist of well-defined lines due to photoelectrons and Auger electrons, and a background of secondary electrons, with less defined energy ranges. The Total Electron Yield (TEY) mode consists of measuring all the electrons emitted by the sample and allows us to get an idea of the photo-absorption process.

Spectra taken from a transition metal shows two broad peaks that reflect the width of the d-bands. But the rest is difficult to identify due to the multiplet structure with interactions between 2p core-hole and 3d-valence electrons with 2p O levels, also the spin-orbit interactions and hybridization with O 2p ligands [15,16].
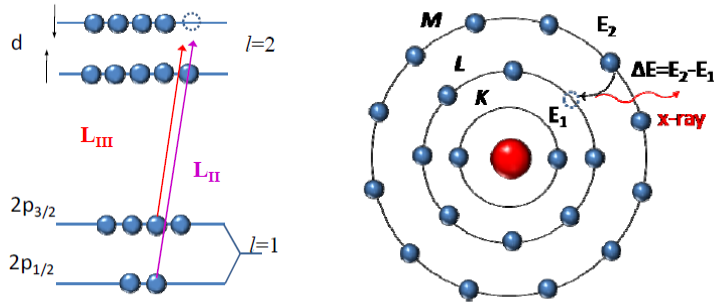
Figure 2.8: Schematic representation of a transition of an electron from the core (left) and of a fluorescence process (right).

4.2. XMCD

X-Ray magnetic circular dichroism (XMCD) is a technique that uses the polarization properties of X-Rays to probe microscopic magnetism [13]. The interest of using circular polarized light comes from the fact that magnetic absorption cross-section is directly proportional to the macroscopic magnetic moment.

We study the dichroism effect by applying the principles of crystal-field theory. We use a semiclassical model where the atom is quantified, and the electromagnetic field is described by Maxwell´s equations. The Hamiltonian which describes the interaction between the atom and the electric field is:

$$H_{int} = -\left[\sum_i \frac{q}{m} p_i \cdot A(r_i) - \sum_i \frac{q^2}{2m} A(r_i)^2\right] - \left[\sum_i g_i \frac{q}{m} S \cdot B(r_i)\right] \quad (21)$$

Where q is the electron charge, m its mass, **p** its momentum and **S** its spin. The electromagnetic field generated by the incident photon is described here by the vector potential **A**, which includes the magnitude of electric field, **e**, and by the magnetic field **B**. In principle, only the first term is relevant to X-Ray absorption and its "spin sensitivity", because the only spin dependent term in the expression is the third one. This term is the dipolar magnetic contribution, which is negligible because the principal quantum number of the initial state is different from that on the final state. Thus, the wave functions of the initial and final states remain perpendicular during the absorption process and the matrix element **S·B** is zero. This means that the spin is conserved during the absorption.

The probability of transition between and initial state $|i\rangle$ and the final state $|f\rangle$ is given by the Fermi Golden Rule:

$$T_{i,f} = \frac{2\pi}{\hbar} \sum_{i,f} |\langle f | \boldsymbol{r} \cdot \boldsymbol{e} | i \rangle|^2 \delta(E_f - E_i - \hbar\omega) \tag{22}$$

Where **e** is the X-Ray electric field vector and **r** denotes the electron position. The above expression is not spin dependent. The spin dependent will be induced later by the spin-orbit coupling either in the initial or the final states.

For a circularly polarized beam propagating along **z** axis, the expression for the electric field is:

$$\varepsilon^+ = \frac{(e_x + ie_y)}{\sqrt{2}}, \varepsilon^- = \frac{(e_x - ie_y)}{\sqrt{2}} \tag{23}$$

When the light is circularly polarized to the left and the right, respectively. Then, **r·e** will be, in spherical coordinates:

$$\boldsymbol{r} \cdot \boldsymbol{\varepsilon}^\pm = (x \pm iy) = \mp r\sqrt{\frac{4\pi}{3}} Y_1^{\pm 1} \tag{24}$$

Where Y are the spherical harmonics. Then the transition matrix element ($|\langle f | \boldsymbol{r} \cdot \boldsymbol{e} | i \rangle|$) will be non-zero only if:

$$\Delta l = l_f - l_i = \pm 1 \tag{25}$$

$$\Delta m_l = m_{lf} - m_{li} = +1 (\text{left}) \text{ or } -1 (\text{right}) \tag{26}$$

Being l the orbital angular momentum and m_l its projection along the z direction. These are the selection rules for the electric dipole approximation. Finally, the two absorption cross-sections for the left (σ₊) and right (σ₋) circular polarizations are:

$$\sigma_\pm = 4\pi^2 \hbar\omega\alpha \sum_{i,f} \left| \left\langle i \left| \mp r\sqrt{\frac{4\pi}{3}} Y_1^{\pm 1} \right| f \right\rangle \right|^2 \delta(E_f - E_i - \hbar\omega) \tag{27}$$

And the dichroism will be defined as the asymmetry ratio:

$$XMCD = \frac{\sigma_+ - \sigma_-}{\sigma_+ + \sigma_-}$$ (28)

Due to the selection rules, some electronic transitions are forbidden during X-Ray absorption. ΔJ=0, $\pm$1 due to the dipole selection rule, so transitions like 1/2 -> 5/2 are forbidden (spin flips are forbidden in electric dipole transition). So, photoelectrons from the *p*-core shell can only be excited to d hole states with the same spin direction. Hence, the spin-split valence shell acts as a detector for the spin of the excited electron, and the transition intensity will be proportional to the number of empty states at the d-shell with a given spin [17]. Since the dipole selection rule is different for right and left circularly polarized light, the respective components may be absorbed differently, depending on the nature of the initial and final band states. The emitted radiation will be elliptically polarized due to this imbalance. The most common way of measuring XMCD is total electron yield (TEY), which has a higher signal to noise ratio compared to fluorescence yield (FY).

One interesting method of XMCD measuring is X-Ray resonant magnetic reflectivity (XRMR), which provides information from the first atomic layer of the sample. XRMR is a coherent elastic scattering without a complex final state effect, and the participation of a core excitation makes it element selective [18,19]. Is difficult to extract quantitative values from XRMR because the reflected intensity measured is a dynamically scattered beam that depends on the absorptive and dispersive parameters of the material. The determination of the intensity, shape, coercivity and other parameters of XMCD hysteresis loops can be very useful to study the magnetic behavior of single layers and multilayers of soft and hard ferromagnets, also permits to obtain information about induced magnetic states emerging at interfaces of heterostructures [20–22].

5. Polarized Neutron Reflectometry

Polarized Neutron Reflectometry (PNR) is a widely used technique [23,24] that consists on measure the reflection of a neutron beam on a sample as a function of the perpendicular component of the wave vector transfer. Polarized neutrons are intrinsically sensitive to the difference of magnetic and nuclear components of the refractive index across interfaces. So, the technique can provide quantitative information about the magnetization depth profile and structural details of thin films and heterostructures. The reflected neutrons are related to the depth dependence of the index of refraction averaged over the lateral dimensions of the interface. PNR is characterized by an extremely high depth resolution of a fraction

of nanometer even for films of a hundred nanometer thick. It is a very well-suited probe for characterization of magnetic thin films.

In a PNR experiment, a magnetic field H is applied to the sample. Given the relation $B = \mu_0 H + M$, and since H is usually much smaller than M, the neutron spin will interact only with the magnetic induction inside the sample and then cannot distinguish between spin and orbital moment. The magnetic contribution to the scattering potential is given by $V_m = -\mu_n \cdot B$, where μ_n is the neutron magnetic moment. Neutrons are previously polarized with a magnetic field and can be send parallel or antiparallel to the applied field. If the magnetic induction **B** inside the sample makes an angle with the external field **H**, the in-plane component of **B** that is perpendicular to **H** will lead to spin-flip neutron scattering as a consequence of the precession of the neutron spin around **B**. A scheme of the process is presented in the Figure 2.9.

As a convention, R^{++} and R^{-} are the non-spin-flip reflectivities, where the + and − signs represent the spin parallel or anti-parallel to the applied field.

PNR measurements and analysis were conducted at the at the Spallation Neutron Source User facility operated by the Oak Ridge National Laboratory.
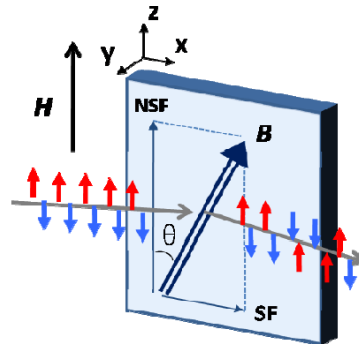
Figure 2.9: Schematic representation of the possible magnetization components of the sample that induce spin-flip and non-spin flip scattering, to the reflected neutron polarization.

6. Fabrication Techniques

Once the thin films and heterostructures have been sputtered, it is necessary to define a pattern on the samples in order to obtain measurable devices. The complexity of the patterning process depends on the materials involved in the thin film and the feature dimensions. For the tunnel junction's fabrication, 5μm lateral

precision is needed in order to avoid tunnel barrier defects. For the Hall bar design, the precision needed is 100µm, far from the lithography limit. Ultraviolet optical lithography and Argon ion milling are the necessary techniques for the fabrication.

6.1. Optical Lithography

Photolithography is a technique used to generate high precision microscopic patterns over photoresist materials [25,26]. The pattern is optically projected on the surface of the sample from a "master pattern" recorded on a photomask. These masks are generally made of a film of chromium on a quartz plate. The method of "printing" the mask on the sample is placing the mask on the sample covered with photoresist and illuminating it with UV radiation. Two types of photoresist are available, positive and negative. Their difference is the behavior when they are illuminated. The positive photoresist becomes soluble to the photoresist developer when its illuminated, so it reproduces the opaque pattern of the mask. On the other hand, negative resist becomes insoluble to the developer when illuminated, reproducing the transparent pattern of the mask.

The principal part of the microlithography is the exposure system. It consists of a lithographic lens structure used for collimating UV light from a Hg lamp, a mask holder, an optical microscope (for aligning mask and sample) and a sample positioner system (Figure 2.10).

An important matter is the thickness of the deposited photoresist. In order to optimize the lateral resolution of the lithography, the resist thickness must be thin (in the micrometric order). This is achieved with a spinner system, where the resist is spinned at 6500 rpm for 30 seconds.
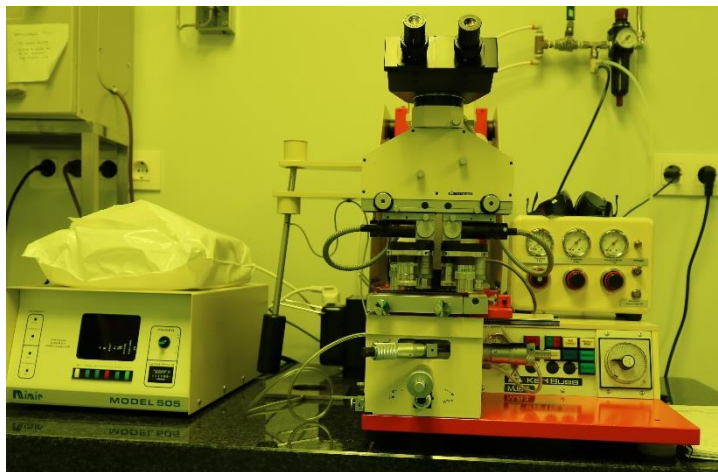

Figure 2.10: Image of the Karl Suss photolithography system used for the fabrication of the samples

6.2. Argon Ion Milling

Ar Ion milling is a non-selective material technique consisting on a sputtering process where the sample is located on the target place. This way the Ar ions impact on the sample surface, removing atoms from the regions that are not protected by the photolithography resist. The system works at high pressures, around 100 mTorr. At these pressures the etching process is isotropic, which means a low aspect ratio etching. The etching rate on complex oxides is around 10 nanometers per minute, meanwhile it is larger on the resist. Using large resist thicknesses allow that the resist is not completely removed during the etching process. After the Ar milling, an Ar+O_2 milling is done in order to retire the resist from the sample surface, leaving only the part of the sample that has not been etched. To minimize any heating that could produce a resist degradation or sample deoxygenation, the sample is mounted onto a water-cooled sample holder.

7. Devices fabrication

Here the steps of fabrication of the two principal devices fabricated in this thesis are described. For the tunnel junctions, the objective was to minimize the number of technological steps and fabricate several devices by sample. Meanwhile, for the Hall bars, the objective was to reduce the number of possible current paths across the sample.

7.1. Tunnel junction devices

The first step of the process is to define the junction pillars in the structure. For that we deposit a metal via sputtering over the sample surface. In our case the selected metal was gold. The first lithography process consists on use a mask with dark junction areas, so once the sample has been exposed and developed, the junction areas are covered by resist and the rest of the sample is clean. In the Ar Ion milling process, the junction areas will be preserved from the etching, defining a trilayer pillar.

Once the pillars are defined, a photoresist is deposited onto the sample in order to passivate it electrically. After that, holes are opened onto the pillars using an inverse optical mask, with the areas of the junctions and the lower electrode transparent and the rest of the mask dark. For the last step, the sample is covered by a mechanical mask and sputtered with gold, forming pads of 1mm^2 area. That pads are later connected to the measuring system. The scheme of the process is presented in the (Figure 2.11).
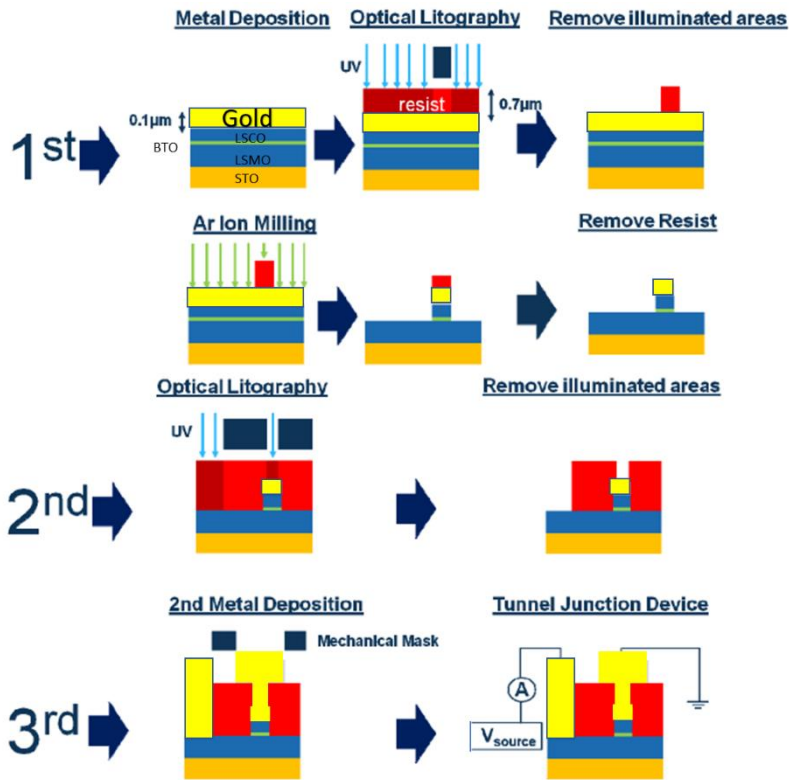
Figure 2.11: Scheme of the patterning process of a tunnel junction from the trylayer to the measurable device

7.2. Hall Bar devices

After the growing process, the iridate samples are covered with sputtered gold in order to passivate it. After that, the first lithography step, where the hall bar and the contacts are covered by the resist after the develop. Once the device is protected, it is defined via Ar ion milling. The resist is retired by an Ar+O_2 ion milling.

With the device defined, it is necessary to retire the gold deposited onto the Hall bar. For this a second lithography step is performed. In this step, the hole sample is illuminated except for the six contacts. With the contacts protected, the sample is introduced into a "gold etchant" liquid. Finally, a second Ion milling with Ar+O_2, in order to remove the resist from the metallic contacts. The scheme of the hole process is presented in the Figure 2.12. The Hall bar dimensions are 1.5mm x 2.5mm, eliminating the possibility of pattern more than one device by sample. The hole dimensions of the device are indicated in the Figure 2.13.
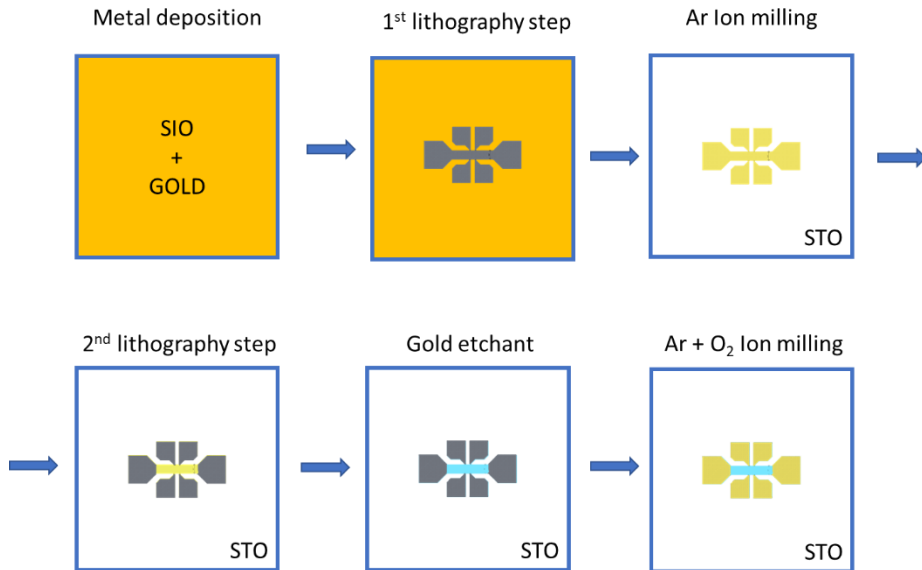
Figure 2.12: Scheme of the fabrication from a SIO layer to a Hall Bar device.
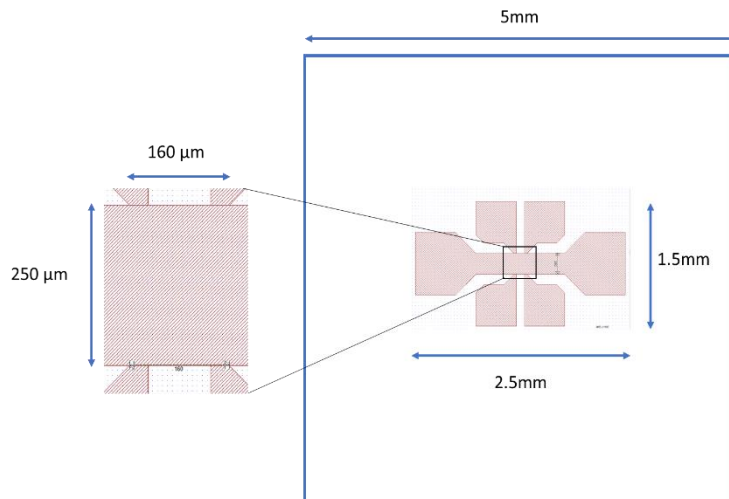
Figure 2.13: Dimensions of a Hall bar device. The current flows across the distance between the two voltage contacts, so the length is 160μm, and the width is 250μm.

8. Transport measurements

8.1 Tunnel junction measurements

Transport in tunnel junctions was measured in two closed He-cycle cryostations with magneto-optic modulus from Montana Instruments [27], installed in the group GFMC (UCM) (Figure 2.14). With the closed-cycle operation no helium is consumed

during the measurements, this avoids the high costs and the challenging operation associated with liquid cryogens. A variable speed helium compressor pumps helium gas into the cryocooler. It permits a wide working-temperature range (from 350K to 3.2K ideally), with a temperature stability of <10mK. A temperature sensor Cernox^{TM} is placed near the sample. Micro coaxial wires connect the sample to the electronic system for low noise measurements. For magnetic measurements, a magneto-Optic modulus with a dipolar magnet is integrated. It provides magnetic fields up to ± 0.7 T.

The resistance measurements of thin films (of LSCO, LSMO, etc) were taken in the Van der Pauw four-point configuration to eliminate any contribution given by the in-series contact resistance [28]. For the tunnel junction measurements, 2-point contact method was used, assuming that the junction resistance is much larger than the contact resistance.

The electroresistance loops were measured by recording the resistance at a 10mV excitation signal (V$_{Read}$) after the application of a write voltage (V$_{Write}$) of the hysteresis loop sequence. Current-voltage and differential conductance-voltage curves were measured simultaneously using a Keithley 6221 to inject the AC or DC current and a Keithley 2182A nanovoltimeter to detect voltage.

The measurements of I vs. V and differential conductance were done independently but in the same measurement. The system applies (with the Keithley 6221: AC and DC current) a DC current to the tunnel junction and measures (using the Keithley 2182A: Nanovoltimeter) the corresponding voltage for the IV curve. After that the 6221 apply a small AC current $I = I_m \cdot \sin(\omega t)$ and measure the resulting voltage $V = V_m \sin(\omega t)$. The differential conductance is obtained dividing I_m/V_m. The

Figure 2.14: Left: Image of a Montana Cryostation s50 series with a magnetic module integrated. Right: Overhead of the sample platform and the pole tips inside the magnetic module

typical input variables were a DC current range [-100nA, 100nA] with a 1nA step. The AC current range was in the interval [2step, 5step]. Every IV and differential conductance measurement was repeated 6 times and averaged to minimize the noise contribution.

8.2 Hall bar measurements

The transport measurements of Hall bar samples needed high magnetic fields and low temperatures. For this aim, a Quantum Design PPMS, capable of applying 14T in the out of plane direction. The system is equipped with several standard options: Electrical conductivity, AC transport, thermal conductivity, Seebeck effect, etc. A range of properties are measurable through configurable external equipments. Temperature operation range is between 1.8K to 300K. An image of the PPMS system used in this work can be seen in the Figure 2.15.

Hall bar samples were measured in the DC resistivity mode using a standard puck (Figure 2.16), which allows to measure up to three different channels. It allows to measure resistances between 10μΩ to 5MΩ in 4-probe configuration and admits currents between 2nA to 8mA. Bridge parameters are configurable in order to limit the maximum voltage, current or power at the sample for protecting sensitive devices.

Figure 2.15: Image of the PPMS located in the ICMM (CSIC). The helium chamber is on the right and the electronics are in the left of the image.

Figure 2.16: Standard three channel puck for PPMS measurements

8. References

[1]   M. Varela, Z. Sefrioui, D. Arias, M. A. Navacerrada, M. Lucía, M. López de la Torre, C. León, G. D. Loos, F. Sánchez-Quesada, and J. Santamaría, Phys. Rev. Lett. **83**, 3936 (1999).

[2]   N. David and N. W. Ashcroft, *Solid State Physics*, First (2003).

[3]   A. Guinier, *X-Ray Diffraction: In Crystals, Imperfect Crystals, and Amorphous Bodies* (2003).

[4]   E. E. Fullerton, I. K. Schuller, H. Vanderstraeten, and Y. Bruynseraede, Phys. Rev. B **45**, 9292 (1992).

[5]   M. von Ardenne, Z. Tech. Phys. **19**, 553 (1938).

[6]   R. F. Egerton, Reports Prog. Phys. **72**, (2009).

[7]   P. D. Nellist, M. F. Chisholm, N. Dellby, O. L. Krivanek, M. F. Murfitt, Z. S. Szilagyi, A. R. Lupini, A. Borisevich, W. H. Sides, and S. J. Pennycook, Science (80-.). **305**, 1741 (2004).

[8]   P. E. Batson, N. Dellby, and O. L. Krivanek, Nature **419**, 94 (2002).

[9]   R. F. Egerton, *Electron Energy-Loss Spectroscopy in the Electron Microscope* (Springer US, Boston, MA, 2011).

[10]   D. H. Pearson, C. C. Ahn, and B. Fultz, Phys. Rev. B **47**, 8471 (1993).

[11]   J. L. Erskine and E. A. Stern, Phys. Rev. B **12**, 5016 (1975).

[12]   K. H. Müller, K. Dörr, T. Walter, M. Sahana, K. Brand, and L. Schultz, J. Magn. Magn. Mater. **242**–**245**, 447 (2002).

[13]   F. Hippert, E. Geissler, J. L. Hodeau, E. Lelièvre-Berna, and J.-R. Regnard, *Neutron and X-Ray Spectroscopy* (Springer Netherlands, Dordrecht, 2006).

[14]   J. Stiihr, J. Electron Spectros. Relat. Phenomena **2048**, 253 (1995).

[15]   B. T. Thole, P. Carra, F. Sette, and G. Van Der Laan, Phys. Rev. Lett. **68**, 1943 (1992).

[16]   T. Burnus, Z. Hu, H. H. Hsieh, V. L. J. Joly, P. A. Joy, M. W. Haverkort, H. Wu, A. Tanaka, H. J. Lin, C. T. Chen, and L. H. Tjeng, Phys. Rev. B - Condens. Matter Mater. Phys. **77**, 1 (2008).

[17]   C. Kao, J. B. Hastings, E. D. Johnson, D. P. Siddons, G. C. Smith, and G. A. Prinz, Phys. Rev. Lett. **65**, 373 (1990).

[18]   S. Valencia, A. Gaupp, W. Gudat, L. Abad, L. Balcells, B. Martinez, S. Valencia, A. Gaupp, W. Gudat, L. Abad, L. Balcells, and B. Martinez, **023903**, (2013).

[19]   M. Yu, J. Hattrick-simpers, I. Takeuchi, J. Li, Z. L. Wang, J. P. Liu, S. E. Lofland, S. Tyagi, J. W. Freeland, D. Giubertoni, M. Bersani, M. Anderle, M. Yu, J. Hattrick-simpers, and I. Takeuchi, **063908**, 1 (2005).

[20]   P. Carra, B. T. Thole, M. Altarelli, and X. Wang, Phys. Rev. Lett. **70**, 694 (1993).

[21]   C. T. Chen, Y. U. Idzerda, H. J. Lin, G. Meigs, A. Chaiken, G. A. Prinz, and G. H. Ho, Phys. Rev. B **48**, 642 (1993).

[22]   J. Tornos, F. Gallego, S. Valencia, Y. H. Liu, V. Rouco, V. Lauter, R. Abrudan, C. Luo, H. Ryll, Q. Wang, D. Hernandez-Martin, G. Orfila, M. Cabero, F. Cuellar, D. Arias, F. J. Mompean, M. Garcia-Hernandez, F. Radu, T. R. Charlton, A. Rivera-Calzada, Z. Sefrioui, S. G. E. Te Velthuis, C. Leon, and J. Santamaria, Phys. Rev. Lett. **122**, 37601 (2019).

[23]   G. P. Felcher, R. O. Hilleke, R. K. Crawford, J. Haumann, R. Kleb, G. Ostrowski, G. P. Felcher, R. O. Hilleke, R. K. Crawford, J. Haumann, R. Kleb, and G. Ostrowski, Rev. Sci. Instrum. **609**, (1987).

[24]   P. Taylor, V. F. Sears, and C. R. Laboratories, Neutron News 37 (1992).

[25]   L. Bergstrom, K. Johansson, and C. Nilsson, *The Physics of Micro/Nano-Fabrication* (Springer US, Boston, MA, 1992).

[26]   M. Ohring, *Materials Science of Thin Films*, 2nd ed. (Elsevier, 2002).

[27]   M. Instruments Https://Www.Montanainstruments.Com/Products/Cryostation/?Tab=product-Specs-Content (2020).

[28]   L. J. Van Der PAUW, Philips Tech. Rev. **20**, 220 (1958).

Chapter 3: Interfacial properties in tunnel junctions based on complex oxides

1. Introduction

The transition metal oxides (TMOs) are a source of novel functionalities, which can be implemented in both thin films and interfaces [1]. The rich physics of this oxide family is related to the delicate balance between charge, spin and orbital degrees of freedom. Most of the materials that show this physics diversity have perovskite structure, having a similar lattice constant, allowing for the growth of heterostructures with very high structural quality. Present synthesis methods are able to engineer interfaces between TMOs with an atomic-scale precision producing atomically sharp interfaces. These are singular regions of the material because there is a natural breaking of the lattice symmetry and structural stress builds up. The distance and the bonds between the ions are altered, giving rise to changes in the bandwidth, interactions, and energy levels degeneracy. This together with unconventional electronic reconstructions that appear in the case of polar surfaces, may promote the appearance of new phases at surfaces and interfaces. Electronic reconstruction related to charge transfer is often possible in oxide-based heterostructures due to the mixed-valence character of the ionic species involved. This charge transfer induces carrier densities that are different at the interface than in the bulk, resulting in physical properties at the interface which may completely differ from those of the constituent materials alone. The objective is to tailor and control the physical properties at these interfaces between complex oxides, which will be the origin of future electronics and spintronics.

Emergent electronic states nucleating at the interface between correlated oxides are very promising in technological applications. The interface reconstructions (orbital, electronic…), underlie important changes in their electric and magnetic ground states. Particularly, in perovskite oxides with an orbital moment quenched by the octahedral crystal field, magnetism is determined by the spin degree of freedom. Interfacial induced properties at oxide interfaces can be used to tailor novel functionalities in multiferroic tunnel junctions.

1.1 Novel functionalities in multiferroic tunnel junctions

Ferroelectric tunnel junctions (FTJ) are tunnel junctions with a ferroelectric barrier. These systems have gathered lot of interest recently due to the possibility of modifying the tunnel current with the ferroelectric state of the barrier (with the polarization pointing up or down). The resistance difference for both states is called

Tunneling electroresistance (TER) [2]. TER can be originated by different methods, as has been previously discussed [3,4]. It can be originated from changes in interface bonds due to the ferroelectric polarization switching or from modulations of the tunnel barrier height resulting from the screening asymmetries of the electrodes. Giant electroresistance has been reported from ferroelectric tunnel junctions, which have metals with different screening lengths as electrodes.

The large electric fields present in the ultrathin barrier to switch the ferroelectric polarization may be responsible for the activation of ion motion, typically oxygen, which is the most mobile atom in transition metal oxides [5]. Such a defect chemistry could be related to profound changes in the physics of the interface like inducing magnetism in non-magnetic materials or forcing a metal-to-insulator transition as a function of the doping level. In the recent times, the coupling between ferroelectric polarization and ferroionic states has been proposed to be the source of novel phenomena [6]. This coupling between oxygen vacancies (OV) and ferroelectric polarization can be enhanced when it occurs at the interface between a ferroelectric and an electrochemically active oxide that has oxygen vacancies spontaneously and mixed-valence transition metal ions. The coupled switching of the OV and the FE polarization may produce enormous changes in the interfacial doping level, yielding unexpected electronic phases.

In the last years, several theoretical studies have predicted that ferromagnetic properties of systems may change dramatically at the interface with a ferroelectric. Conversely, switching the FE polarization could induce modifications of the spin polarization. If we have a tunnel junction, the density of states can be modified ferroelectrically and is expected to modulate the TMR, as García et al. discovered [7].

One of the most promising applications of FE tunnel junctions are Ferroelectric random-access memories, or FeRAMs. The device is typically formed by a ferroelectric thin film sandwiched between two electrodes, and the information is saved in the non-volatile state of the ferroelectric polarization. The polarization of the FTJ is switched by applying an electric field between the electrodes. The tunnel transmission may be tuned by the polarization, producing TER values of ~10^4 % (Figure 3.1). In the recent years, the concept of FTJs has been improved thanks to the experiments of several groups using different ferroelectrics such as $BaTiO_3$ [8–14]. Performance metrics such as ON/OFF ratios, write energies, data retention, scalability and endurance are some critical characteristics to consider in FTJs as non-volatile memories. I versus V_{Write} curves show non-linear characteristics and a weak temperature dependence, indicating that electron transport is in the direct tunneling regime.
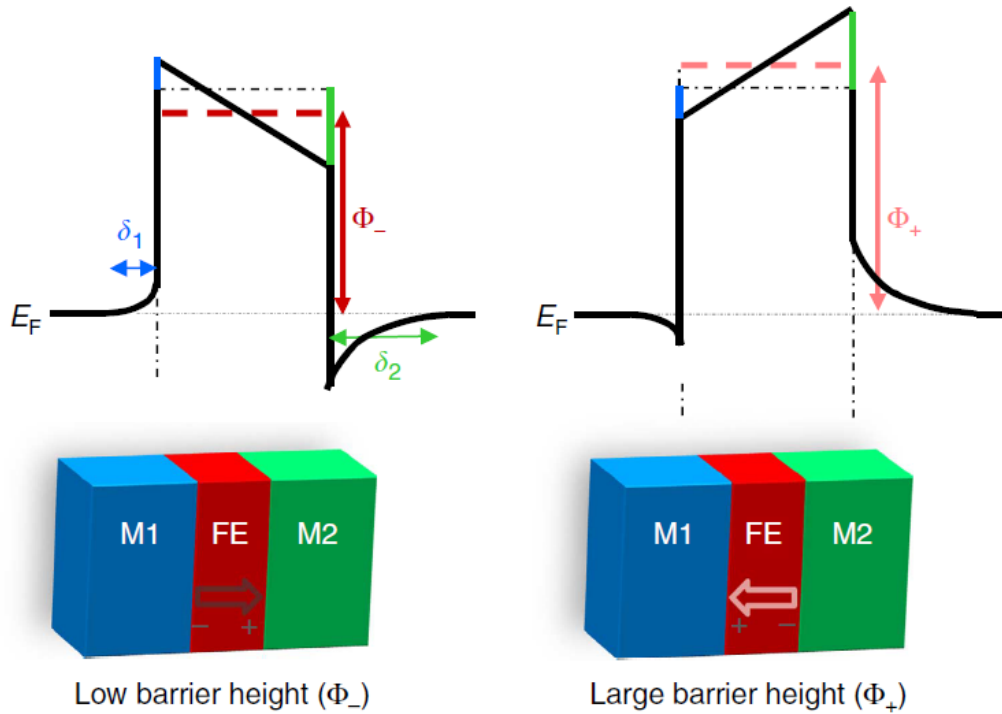
Figure 3.1: Modulation of the tunnel barrier height as a function of the ferroelectric polarization direction. Ferroelectric bound charges are screened in a shorter distance in M1 than in M2. In average, barrier height (φ) is smaller when P points to the electrode M2.

The use of a multiferroic barrier enabled Gajek et al. [15] to demonstrate a four resistance states memory using a tunnel junction based on the ferromagnetic electrode ($La_{0.7}Sr_{0.3}MnO_3$) and the ferromagnetic and ferroelectric barrier ($La_{0.1}Bi_{0.9}MnO_3$). However, a *ab initio* calculations performed on Fe/BTO interfaces show the possibility to enable multiferroic behaviour in FTJ with BTO barrier , thanks to a large interface magnetoelectric coupling resulting from the modification of the interface bonding, switching the ferroelectric polarization [16].

In addition to the use of FTJs as digital memories with discrete resistance states corresponding to the two FE polarization orientations, there is the possibility to access to non-uniform ferroelectric configurations, leading to the creation of multistate digital memories or memristors. Intermediate states can be stabilized depending on the write voltage amplitude. This memristive behaviour emulates the neuronal synapses and is a promising route to implement neuromorphic computing.

As tunnel current is highly sensitive to the electronic properties of the systems at the interface, some materials can exhibit enormous modifications of their properties when an electric field is applied. The modifications can lead to a large

ON/OFF ratio, as Wen et al [8] show in BTO-based tunnel junctions, with an ON/OFF ratio over 10^4. An interesting way to increase this ratio is to induce phase transition at the interface of the materials, like a metal/insulator transition forced by the electric field of the ferroelectric polarization. The modulation of the tunnel resistance induced by the phase transition when switching the ferroelectric polarization was demonstrated by *ab initio* calculations in [17].

1.2 Superconducting cuprates

TMOs are important materials for application in electronic technologies because of their electrical, optical and dielectric properties, despite being historically bad metals. Although these materials are very complex, their usefulness normally comes from their enormous resistance to the electrical current or their optical transparency to some optical wavelengths.

The wide variety of properties in TMOs is related to a fundamental chemical difference between oxygen and the metallic elements, the difference of electronegativities. This difference result in an insulating or semiconducting behaviour in these oxides, with energy gaps between the highest occupied orbitals in the solid, derived from oxygen electronic states, and the lowest unoccupied orbitals derived from the metal electronic states. The concept of complex oxides changed dramatically in 1986 when high critical temperature (Tc) superconductivity was discovered in copper oxides [18]. Currently, there is not a universally accepted theory that explains why these materials are superconductors, but there are some properties of copper oxides or cuprates that characterize them and distinguish them from other electronic oxides.

Most of the conducting TMOs have energy bands that are formed from the interactions of the d-orbitals of the transition metals present in the compound. The atomic orbitals from the transition metal overlap and interact, forming a band of allowed energy states, which will be partially filled by the electrons available, with the energy states of the oxygen not playing any role in the electronic configuration. This happens in conducting oxides such as V_6O_{13}. On the other hand, in the copper oxides, the energy difference between the oxygen and metal orbitals is very small, so the oxygen orbitals will play here an important role in the electronic energy bands. Thus oxygen has the same relevance as copper in the conductivity of these materials, which is a rare situation in conducting oxides [19].

Another interesting factor of copper-oxides derives from the electronic configuration of the Cu^{2+} ions that are the basis of the superconductivity in these compounds. The Cu^{2+} configuration is d^9. It means that there is only one available
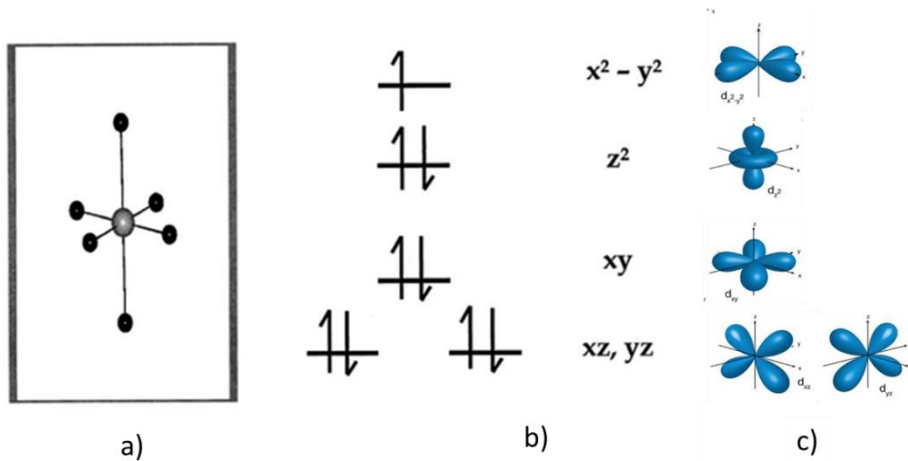
Figure 3.2: a) Cu-O coordination polyhedral present in oxide superconductors. b) d-electron configuration in cuprates with Cu^{2+}. Images adapted from [19]. c) Orbitals shape.

energy state in the d-orbital. The d levels are nondegenerate in the Cu-O polyhedron. The t_{2g} orbitals, which are directed between the oxygen atoms, correspond to lower energies and because of that, are filled with electrons. Because of the Cu-O coordination boundaries, there are four near in-plane oxygens and only one or two apical oxygens, depending on whether the structure is pyramidal or octahedral. Therefore, the orbitals with z components (pointing toward the apical oxygen) have lower energy because of the lower repulsion from the oxygen orbitals. The result is that the unpaired electron will be in the $d_{x^2-y^2}$ orbital, which points towards the in-plane oxygens (Figure 3.2).

The discrete orbitals states in isolated atoms transform in energy bands in solids because of the interaction of all the orbitals, where atoms are close together. As the O 2p and the Cu 3d states have the same energy, as can be seen in the (Figure 3.3a), the electrons fill all the states except half of the Cu $d_{x^2-y^2}$ band. This band structure predicts that these cuprates should be metallic conductors, but instead, they are insulators. The theory of solids assumes that the electrons do not interact to each other, and only interact with the underlying atomic lattice, but in the cuprates there are strong interactions.

When the energy band is half filled, which is the case of cuprates, the addition of a second electron to the $d_{x^2-y^2}$ orbital will require a large amount of energy, because this electron will be repelled by the electron already present. This results in an energy gap when the band is half filled. The bandgap between the highest occupied oxygen states and the empty Cu $d_{x^2-y^2}$ band is responsible for the insulating behavior (Figure 3.3b).
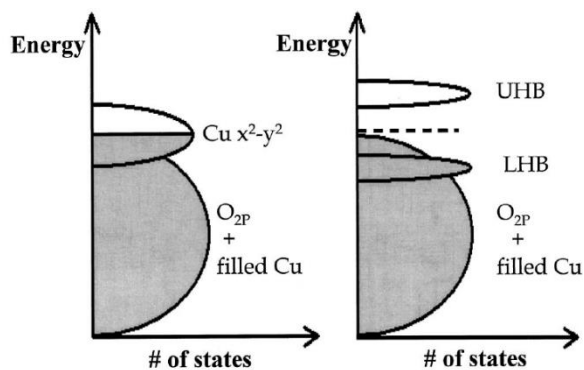
Figure 3.3: a) Energy bands of a superconducting cuprate. b) Scheme of the energy states of a cuprate when the $d_{x^2-y^2}$ band splits due to interacting electrons (into lower Hubbrd band (LHB) and upper Hubbard band (UHB)).

The cuprate family has a common structure that consist on an electronic core formed by a series of CuO_2 planes disposed on a checkerboard-like pattern of the in-plane basal squares of the CuO_x coordination polyhedral (Figure 3.4a). Between these series of CuO_2 planes other layers, known as "Charge reservoir layers", are found. The latter control the electronic density in the CuO_2 planes and electronically connect or disconnect the CuO_2 planes in the "z" axis (Figure 3.4b). The chemistry of these reservoir layers determines the superconducting transition temperature. Superconductivity appears in the system when the number of electrons in the CuO_2 plane is modified from one electron per copper site and the copper ions change from Cu^{2+} to a higher valence. The additional charges come from the charge reservoir layer, typically by the oxygen addition. Nevertheless, the mechanism that triggers the superconductivity in these complex oxides has not been understood yet and is being studied theoretically.

1.3 Recent discoveries in high-temperature superconductivity

The recent finding of superconductivity in a doped finite-layer nickelate has shaken the search of high temperature superconductors. The thin film synthesis consisted in reducing a $Nd_{0.8}Sr_{0.2}NiO_3$ film following a topotactic reaction. This soft chemistry route relies on phase changes produced by atomic oxygen displacements driven by the reaction with reducing agents. The fabrication of reduced derivatives of complex oxides topotactically formed by oxygen de-intercalation reaction with reducing agents has been a strategy pursued in the past [20–25]. Metastable phases such as the Ni (I) compound, fabricated with this method, have been discovered to be superconducting [26,27]. The power of this methodology relies in allowing one to tune the oxygen sublattice of perovskite related oxides. The mixed valence state of transition metal ions and the relative open oxygen lattice allows for topotactic
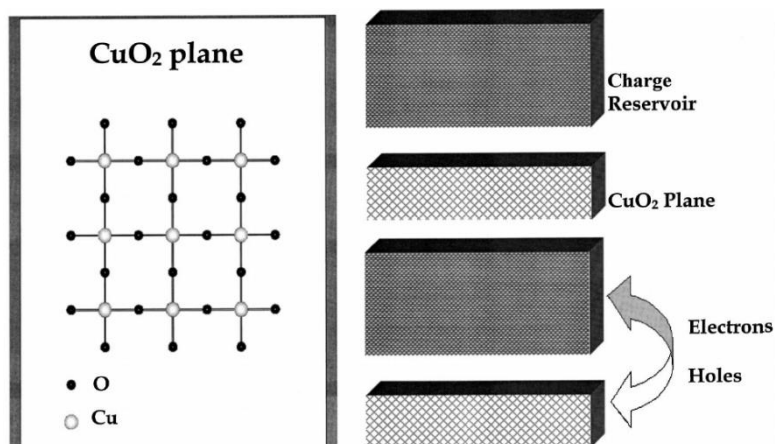
Figure 3.4: a) Distribution of the copper and oxygen atoms in the CuO$_2$ plane. b) Schematic view of the layer distribution in a superconducting cuprate.

reactions driven by the migration of oxygen atoms (vacancies). This modifies the connectivity of the oxygen sublattice which controls important parameters of the electronic phases of the complex transition metal oxides such as dimensionality, band width, strength of the electronic correlations, orbital polarization, etc., which ultimately trigger the nucleation of collective states [28,29].

1.4 Lanthanum-strontium cuprate

In our work, we have studied the La$_5$SrCu$_6$O$_{15}$ (LSCO). This compound was first synthesized just after the discovery of the High Tc Superconductivity [30] and is the first compound of the La-Sr-Cu-O system that is metallic and non-superconducting. It has been used as an electrode in solid oxide fuel cells because of its capacity to host large amounts of oxygen vacancies and because its low activation enthalpy for the reduction and dissociation of oxygen species [31]. This compound belongs to the family of LaCuO$_{3-\delta}$ but is synthesized at high pressures [32,33], and it has an unusually wide range of oxygen stoichiometry 0<δ<0.5.

The copper valence in the LaCuO$_{3-\delta}$ can be varied in the oxygen-defect perovskite almost continuously from +3 to +2, and three distinct ordered phases are observed over its $0.0 \leq \delta \leq 0.5$ stability range. When an oxygen is removed from the tetragonal phase (δ=0) [32], two CuO$_5$ pyramids and two sites which are formally Cu^{2+} are created in the form of square pyramidal pairs for each vacancy inserted. The result is that Cu is found only in octahedral and square pyramidal coordination throughout the range of δ, and that the number of holes (Cu^{3+}) will be equal to the number of octahedral coordination sites in the system (Figure 3.5).
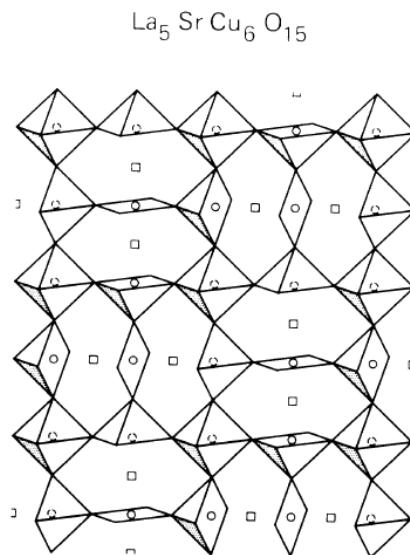
63

$$\text{La}_5 \, \text{Sr} \, \text{Cu}_6 \, \text{O}_{15}$$

Figure 3.5: Scheme of the crystalline structure of the metallic, but not superconducting, $La_5SrCu_6O_{15}$, which is the analogous structure to the cuprate used in our study. Adapted from [38]

In a cubic perovskite, the crystal fields split the fivefold orbital degeneracy of the d states into different levels, a lower triplet, t_{2g}, and an upper doublet, e_g. The e_g in addition, is split into d_{z^2} and $d_{x^2-y^2}$ singlets by tetragonal or lower distortions. The lower t_{2g} states divide into a doublet and a singlet by either a trigonal or a tetragonal distortion, but in the cuprates, as explained before, they are occupied and do not influence the physical properties. The δ=0 rhombohedral (R-)LaCuO$_3$ should be metallic since the two e_g electrons per Cu^{3+} (d^8) are in an orbitally degenerated state that would broaden into a half-filled band. On the other hand, if the correlations are large compared to the bandwidths, this phase would be insulating due to the presence of a Hubbard gap (U) (Figure 3.6). For tetragonal (T-) LaCuO$_3$, if bandwidths are small compared to the crystal field splitting, (T-) LaCuO$_3$ should be an insulator, since the $d_{x^2-y^2}$ band is empty and the d_{z^2} is full. LaCuO$_3$ is a poor metal. This suggest that some overlap occur between empty $d_{x^2-y^2}$ and full d_{z^2} band in the tetragonal form and between empty and full Hubbard bands in the rhombohedral case. Fermi level moves with increasing δ, leading to a Hubbard gap at δ=0.5. As δ increases, oxygen vacancies are created, and these vacancies act as double donors, increasing the Fermi level so that at δ=0.5 the $d_{x^2-y^2}$ becomes half-filled. However, this system has strong correlations, so instead of a metallic behaviour, a Hubbard gap appears, and the system becomes insulator.

In our case, the addition of Sr to LaCuO$_{3-δ}$ is necessary to stabilize the perovskite structure in ambient pressure synthesis [34,35]:

$$1/2 \, O_2 + 2SrO + 2CuO \rightarrow 2 \, Sr_{La} + 2Cu_B + 5O_O^x + V_o^{\cdot\cdot} + 2h^{\cdot} \qquad (29)$$
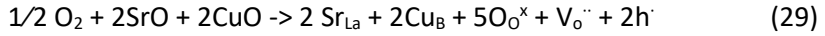
In this equation, negative charges of Sr and Cu are compensated by oxygen vacancies and electron holes that may associate with Cu^{2+} ions and become Cu^{3+}. The presence of Cu^{3+} affects both structural and electrical properties of Sr-doped lanthanum copper oxides.

The structure of $La_{1-x}Sr_xCuO_{2.5-\delta}$ can be orthorhombic or tetragonal, depending on the Sr concentration. As both structures can be considered a distorted and enlarged perovskite, the formation of these structures indicates that the stability of the lanthanum copper oxide perovskite is enhanced by the addition of Sr.

The resistivity of bulk $La_5SrCu_6O_{15}$ is small compared with other cuprates, but never becomes superconducting [36,37]. In fact, the compound has the same structural ingredients as other superconducting cuprates such as CuO_2 sheets (present in all cuprate superconductors), pyramids and CuO chains (present for example in $YBa_2Cu_3O_7$). Also, the Cu valence is similar to that of superconducting compounds. It has an anisotropic 3D perovskite structure with oxygen vacancies channels along the *a* and *b* axes. These channels break the connectivity of oxygen octahedra in a similar way as in the related compound $La_4BaCu_5O_{(13-\delta)}$ [38]. The channels of oxygen vacancies are proposed to be related to the lack of superconductivity of this compound, but this is still an open question.

In this work, we have fabricated ferroelectric tunnel junctions and we show indications of emergent interfacial superconductivity in a non-superconducting cuprate induced by ferroionic coupling at the interface between the cuprate and a
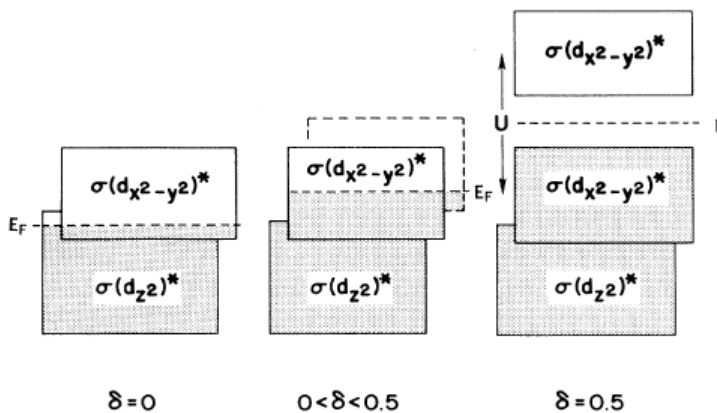

Figure 3.6 : Scheme of the bands diagram of the $LaCuO_{3-\delta}$ as a function of the OV concentration. Adapted from [22].

ferroelectric. As we will demonstrate, the coupled switching of the ferroelectric polarization and the oxygen vacancies have a strong effect enhancing or depressing the gap, indicating that the superconducting state is related to the doping level of the cuprate.

2. Sample growth, characterization and fabrication

We fabricated ferroelectric tunnel junctions that consisted on a cuprate, $La_5SrCu_6O_{15}$ (LSCO) as upper electrode, grown epitaxially on an ultrathin $BaTiO_3$ (BTO) ferroelectric barrier. The bottom electrode was $La_{0.7}Sr_{0.3}MnO_3$ (LSMO). The cuprate has a good lattice matching with the BTO the structure and facilitates the study of the ferroionic coupling at the interface.

Cuprate thin films were grown from a stoichiometric target with composition $La_{0.84}Sr_{0.16}CuO_{2.5-\delta}$, which corresponds to the composition of the $La_5SrCu_6O_{15}$. Samples were grown using a High-Pressure Sputtering system [39,40] in the "Grupo de Física de Materiales Complejos (GFMC)" in "Universidad Complutense de Madrid (UCM)", described in Chapter 2. The growing conditions were a high pressure of pure oxygen (3.2 mbar) and the substrate temperature varied from 750°C for LSCO to 900°C for LSMO and BTO. Once the sample was deposited on the substrate, it went through a one hour annealing at 800°C in a pure oxygen atmosphere (~920 mbar). The samples obtained were homogeneous and, as it is presented in the following section, epitaxial.

2.1 Characterization of LSCO thin films and heterostructures

LSCO samples were grown using a High-pressure Sputtering system and were deposited on (001) $SrTiO_3$. Low magnification High Angle Annular Dark Field (HAADF) Scanning Transmission Electron Microscopy (STEM) image shows that the layers are flat and continuous over large lateral distances (hundreds of nanometers) (Figure 3.7a). The X-Ray diffraction pattern presents the (00c) characteristic reflections of the perovskite structure (Figure 3.7c). Figure 3.7b is a high-resolution STEM dark field image, showing the good epitaxial properties. Buckling in the heavy La/Sr planes can also be observed, which results from the strain field around the chains of oxygen vacancies present in this compound.

Transport measurements were performed in LSCO thin films for different thicknesses (Figure 3.8a) and oxygen concentrations (Figure 3.7b). The R vs. T curves had a metallic behaviour for thicknesses above 5 nm. The 5 nm sample experienced a Metal-Insulator Transition (MIT), showing an insulator behaviour in all the
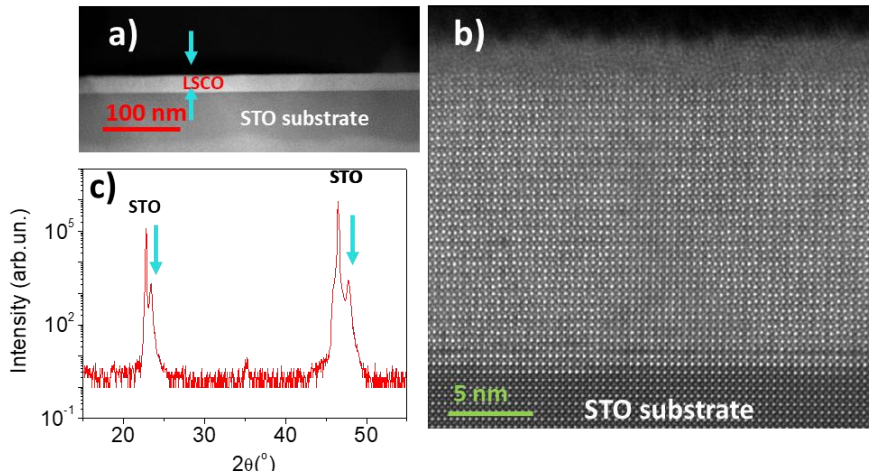
Figure 3.7: a) and b) HAADF images of a LSCO thin film over a STO substrate. c) X-Ray diffraction analysis of a 27nm LSCO thin film.

temperature range. Figure 3.7b shows that the MIT can be induced annealing a metallic sample in vacuum. This suggests that the large concentration of oxygen vacancies combined with their good oxygen diffusivity are playing a role in the electron doping of the system.

Once the LSCO was characterized, we grew epitaxially two different trilayer heterostructures onto (001) SrTiO₃ substrates. The first one was a symmetric heterostructure consisting on LSMO (25nm)/BTO (4.4nm)/LSMO (8nm). The second sample was LSMO (25nm)/BTO (4.4nm)/LSCO (10nm). X-Ray diffraction and reflectometry measurements were performed on the asymmetric heterostructure and are shown on Figure 3.9.
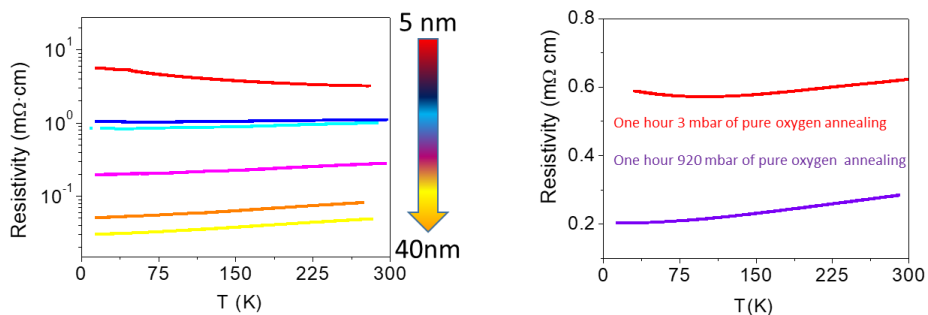

Figure 3.8: a) Resistance versus temperature measurements for LSCO of different thicknesses from 5nm (red) to 40nm (Yellow). A Metal-Insulator transition appears when the LSCO thickness is reduced to 5nm. b) Effect of the oxygen-vacancies concentration in the cuprate resistivity

The LSMO (25nm)/BTO (4.4nm)/LSCO (10nm) sample shows structurally and chemically sharp interfaces, as shown in Figure 3.10a-b. Specifically, Figure 3.10b shows Electron Energy Loss Spectroscopy (EELS) composition maps measured at the specific absorption edges for each element: $L_{2,3}$ for Mn, $M_{4,5}$ for La, $M_{4,5}$ for Ba, $L_{2,3}$ for Ti and $L_{2,3}$ for Cu. With these maps we can deduce the layer termination at the interfaces. From the EELS line scan Figure 3.10d) we observe that both BTO interfaces are TiO_2 terminated. The corresponding lattice planes sequence is represented in the sketch of Figure 3.10c. BTO with symmetrical interfaces has been observed before in LSMO/BTO/LSMO structures grown by High Pressure Sputtering Technique in the same laboratory [41]. On the other hand, the cuprate termination is $(La_{0.84}Sr_{0.16})O$, followed by a CuO_2 plane. We examined the local changes in the Ti valence across the BTO structure by the EELS technique. The occupation of the *3d* band of titanium is directly related to the relative intensities of the L_2 and L_3 titanium edges [42,43]. Therefore, the Ti oxidation state can be quantified from Figure 3.10b using a multiple linear least-square (MLLS) fit to reference spectra for bulk $LaTiO_3$ (Ti^{3+}) and $BaTiO_3$ (Ti^{4+}). From the fit we can obtain a relative proportion Ti^{3+}/Ti^{4+} so that in Figure 3.10e a line scan of the Ti oxidation state for the BTO layer is presented. The oxidation state inside the BTO layer is reduced from +4 in the stoichiometric compound to +3.9. This is in good agreement with previous analysis of the changes in the energy prepeak at the oxygen K-edge [44]. This energy change is typically related to the oxidation state of the transition metal oxide. The trusted values of the prepeak are from the bulk BTO layer. This is because the prepeak is modified near the interface with other oxides. In fact, the prepeak values in the middle of the BTO are in good correspondence with those obtained from the Ti $L_{2,3}$ edge. In the same Figure 3.10e, Cu oxidation state was analyzed across the cuprate using the energy shift of the prepeak at 529 eV at the oxygen K-edge [45]. The Cu is
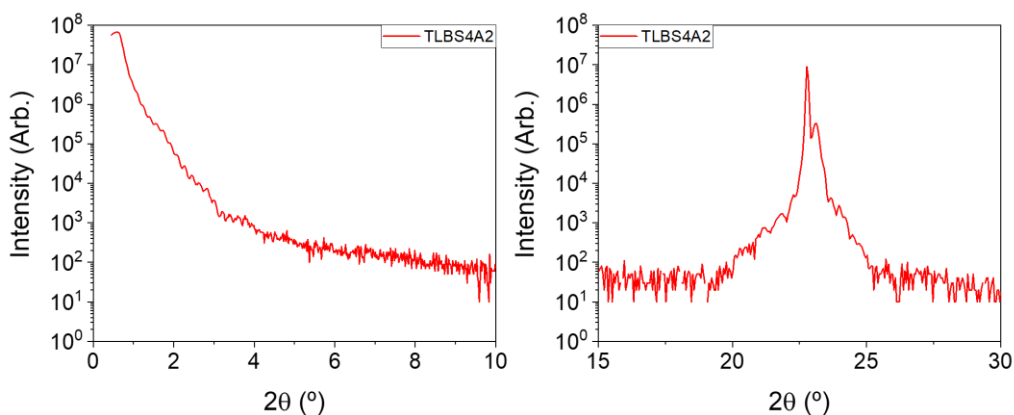

Figure 3.9: X-Ray diffraction (right) and reflectometry (left) 2θ scans of a LSMO/BTO/LSCO heterostructure.
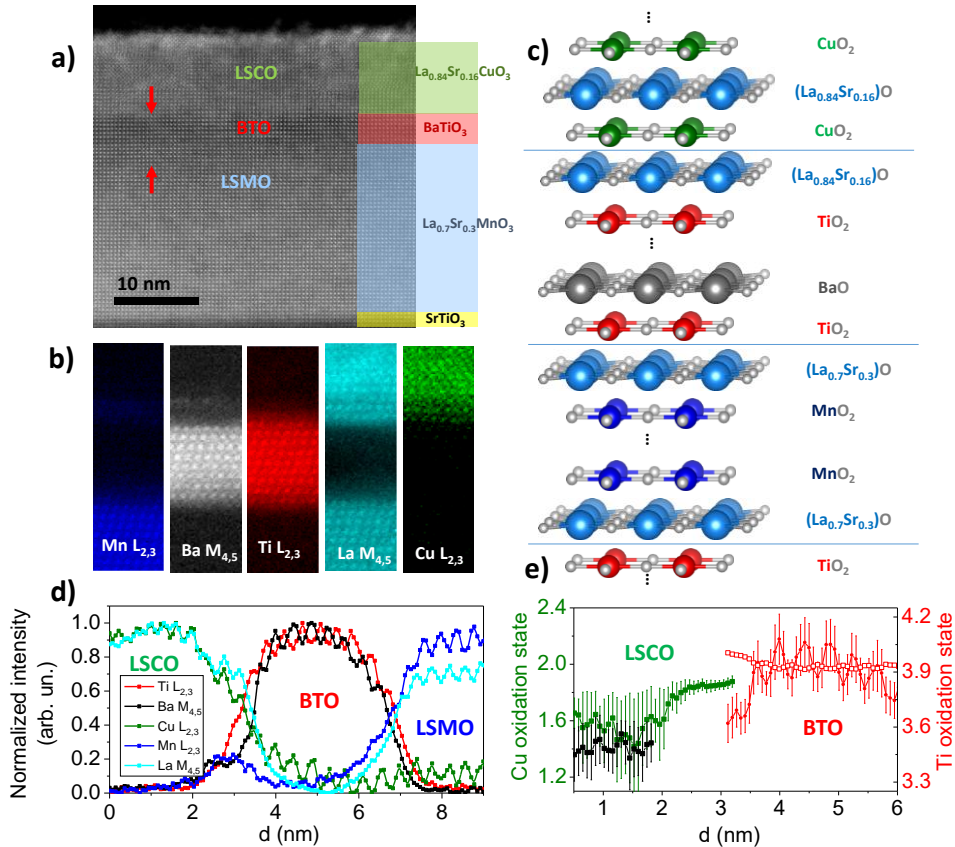
Figure 3.10: a) High Angle Annular Dark Field HAADF image of a trilayer STO (100)//LSMO/BTO/LSCO. The different layers are identified using rectangular colored blocks b) Elemental maps of the different elements as measured by EELS at the following absorption edges: $Mn\ L_{2,3}$, $Ba\ M_{4,5}$, $Ti\ L_{2,3}$, $La\ M_{4,5}$, and $Cu\ L_{2,3}$. . c) Sketch illustrating the sequence of lattice planes of the heterostructure as deduced from EELS. d) EELS line scan illustrating that both BTO interfaces are TiO2 terminated. e) Ti oxidation state measured fitting the Ti $L_{2,3}$ absorption edge (red symbols) and the position of the prepeak at the oxygen K-edge. Cu oxidation state estimated from the energy shift of the oxygen prepeak at the interface (green symbols) and in a single cuprate thin film (black symbols).

strongly reduced when is far from the BTO interface, and its oxidation values are similar to the typical values of cuprate thin films (black symbols) like Cu_3O_4, CuO_2 and CuO. The great increase of the oxidation state at the interface indicates that the dopants are not uniformly distributed in the layer, and this produces a strong hole doping near the BTO interface.

From the Figure 3.10e we can see that the Ti oxidation state decreases near the cuprate interface. This may be indication for the presence of oxygen vacancies (OV) in the ferroelectric layer. Each oxygen vacancy supplies typically one electron to its neighboring Ti atom, but it does not affect the ferroelectricity. Ferroelectricity, as demonstrated in [46], can remain until the doping concentration exceeds a critical

value of 0.11 e⁻ per unit cell. The electrons from the OV can be released to the conduction band saving 0.4 eV [47], which is the difference between the conduction band (-3.6 eV) and the donor level (-4 eV) energies. So, the increase in the oxidation state of the Cu and the decrease of the Ti oxidation state at the interface indicates that a transference of OV from the LSCO to the BTO has been produced. This process may be driven by the strain modulation in the heterostructure. The lattice expands around oxygen vacancies resulting from the underbonding of the transition metal ion [48], and this makes ferroelectric and ferroelastic materials the preferential regions for the nucleation of OV, which are situated in domain walls or dislocations, where the lattice expansion is larger [49].

In terms of strain relaxation, the heterostructure is constrained to the lattice parameter of the STO, which is 3.905 Å. This produces an in-plane compressive strain in the BTO, whose lattice parameter is 4.02 Å, and so an out-of-plane expansion. The Cuprate, with a lattice parameter a= 3.84 Å suffers an in-plane expansion and an out-of-plane compression. The way for the cuprate to release the energy associated with the strain is transferring oxygen vacancies from the first 1 nm to the BTO. This OV transference is seen in the increase of the Cu oxidation state at the interface (Figure 3.10e). Another evidence of OV transference is the highly ordered perovskite state found only at the first 3 unit cells from the interface, and large density of stacking faults that start to emerge one nanometer away from the interface. This indicates that the oxygen vacancies generation produces a strain modulation in the structure.

2.2 Samples fabrication

The device configuration is a distribution of micron-size pillars fabricated with optical lithography technique (see chapter 2). The samples were covered with a photosensitive resist and illuminated across a mechanical mask (Figure 3.11) The lithography was done in two steps. The first step is used to define 8 rectangular pillars, elongated in the 110 easy axis of the bottom LSMO electrode, that will become the tunnel junctions. The pillars are defined through Reactive Ion Etching (RIE) technique using an Ar plasma. Here the sample is etched down to the bottom electrode. The pillars dimensions vary from 5x10µm² to 9x18µm² as represented in Figure 3.11. The AFM images of the pillars are shown in Figure 3.12a. The second step consists on the use of a second mask to electrically isolate the junctions by depositing photoresist in the space between each junction and the lower electrode, and to open holes over the junctions to sputter a metal (gold in this case) and set the electrical contacts on them. We isolate each contact using a shadow mask when depositing the gold contact over the sample (Figure 3.12b). We use this design to
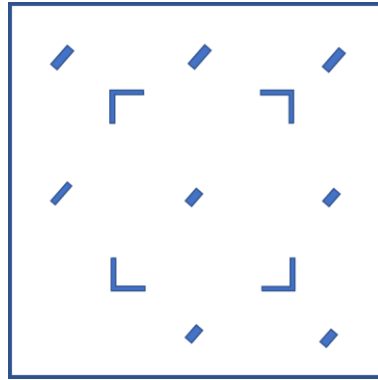
Figure 3.11: Scheme of the mechanical mask used to define the tunnel junctions in the samples during the optical lithography process
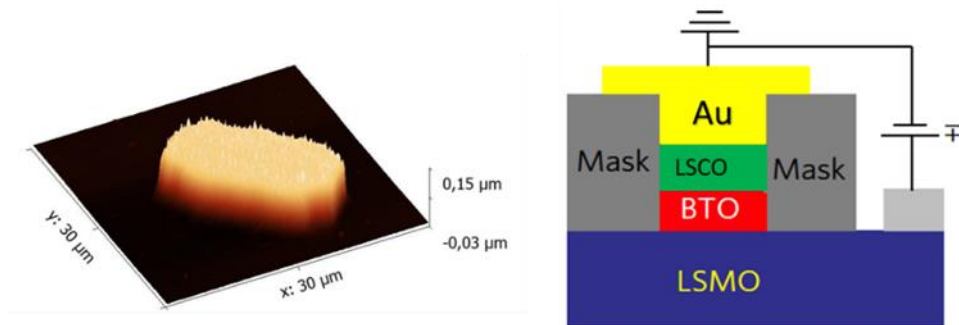

Figure 3.12: a) AFM image of a defined pillar of the heterostructure. The dimensions are approximately 9x18µm². b) Scheme of the tunnel junction final device to measure Current Perpendicular to Plane (CPP).

measure current perpendicular to the plane (CPP). In this configuration, the electronic transport is across the ferroelectric barrier.

3. Interfacially induced magnetism in ferroelectric tunnel junctions

Transport was measured using a closed He-cycle cryostation from Montana Instruments with the Magneto-Optic modulus. Current-voltage and differential conductance-voltage curves were measured simultaneously using a Keithley 6221 to inject the AC or DC current and a Keithley 2182A to detect voltage.

Two kinds of trilayer samples were grown, one symmetric (LSMO/BTO/LSMO), as can be seen in Figure 3.13a, and the other asymmetric (LSMO/BTO/LSCO). The objective was to study the influence of ferroelectric polarization switching on the
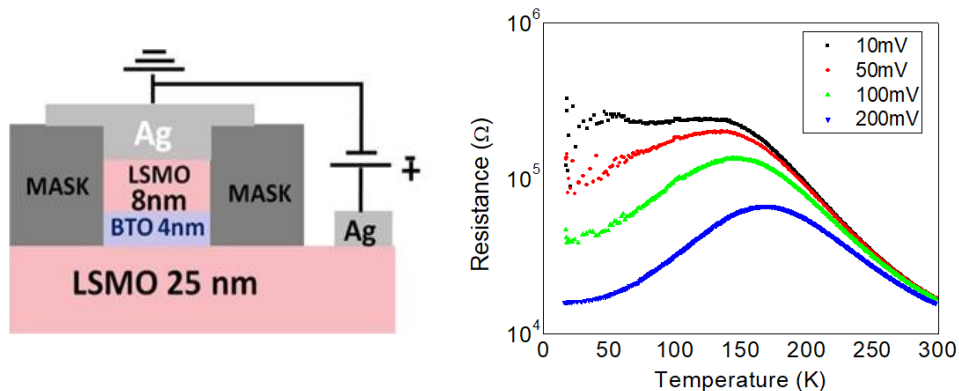
Figure 3.13: a) Scheme of the symmetric tunnel junction device. The top electrode is grounded so positive voltages correspond to electric fields pointing up. b) Resistance versus temperature measurements of a micrometer size symmetric tunnel junction at different read voltages: 10mV (black), 50mV (red), 100mV (green) and 200mV (blue).

interfacial properties of different materials: LSMO and LSCO. In this section, we are going to analyze the measurements of the top LSMO electrode sample.

Figure 3.13b shows the evolution of resistance with temperature of a $5 \times 10 \mu m^2$ tunnel junction. The evolution consists on a resistance increment up to a maximum around 140-170K, and the resistance levels off at the lowest temperatures. This agrees with the literature [50] which says that the tunnel barrier shape is independent of temperature. We can observe that the junction has different resistance values as a function of the applied bias, which corresponds to the non-linear tunneling transport in systems with manganite electrodes [51]. Current vs. voltage curves were also non-linear, and exhibited a small tunneling electroresistance, around 200% (Figure 3.14a). This observed TER is associated with
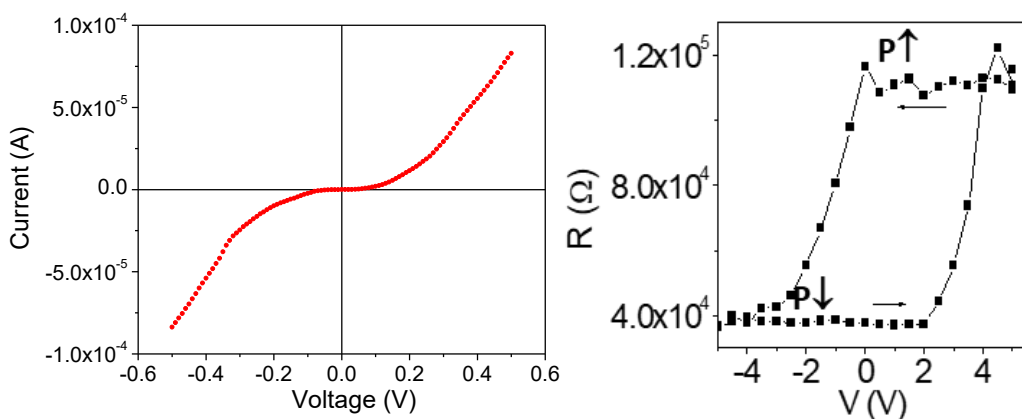

Figure 3.14: a) I-V curve of a LSMO/BTO/LSMO junction measured at 15K, showing a non-linear behavior. b) Electroresistance measured at 120K. The resistance values were recorded at 10mV after applying the DC voltages displayed in the x axis. Adapted from [51].
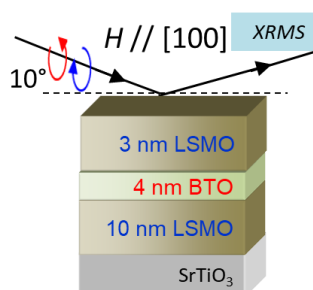
Figure 3.15: a) Scheme of the sequence and thicknesses of the layer used in the X-ray absorption experiment. The magnetic field was applied in the [100] direction of the sample.

ferroelectric polarization switching. The presence of this electroresistance indicates a certain degree of asymmetry in the system [3]. In Figure 3.14b the electroresistance loop is shifted to positive voltages, indicating that ferroelectric polarization prefers to point down, towards the thick LSMO layer.

In order to study properly the interfacial interaction between layers, magnetism was examined in both individual layers and at the interfaces by resonant X-Ray absorption and polarized neutron reflectometry. The X-ray absorption spectroscopy measurements were done at Bessy II (HZB, Berlin) with the VEKMAG end station [52,53]. The sample analyzed by using this technique was STO (100)// LSMO (10nm)/BTO(4nm)/LSMO(3nm) (Figure 3.15). The reduced thickness of the manganite layers is because the electrons and photons extracted from the sample come from a few nm from the surface (around 10nm) and we want to access the bottom electrode. We measured X-ray magnetic circular dichroism (XMCD) and X-ray absorption spectroscopy (XAS) at the Mn and Ti L_2 and L_3 absorption edges (Figure 3.16) and X-ray magnetic scattering (XRMS) [54] around the $L_{2,3}$ edge of the manganese and the titanium (Figure 3.16).

Figure 3.16 shows X-ray absorption spectra (upper panels) and X-ray magnetic circular dichroism (lower panels) in reflectivity mode for Mn and Ti at their absorption edges in a trilayer. The intensities of the four graphs are in arbitrary units because it depends on the intensity of the beam in the measuring moment. From the XMCD signal of Ti we can conclude that magnetism is present in the BTO layer.

In Figure 3.17 we show a hysteresis loop measured at the titanium $L_{2,3}$ edge. In the blue cycle two different coercive fields are evident, the first one at 160 Oe and the second one at 470 Oe. These two coercive fields correspond to the bottom and the top manganite layers respectively, which switch at different fields due to their different thicknesses. The magnetic loop found in titanium has the same coercive field as the bottom LSMO (See appendix 1), but a second coercive field is not visible.
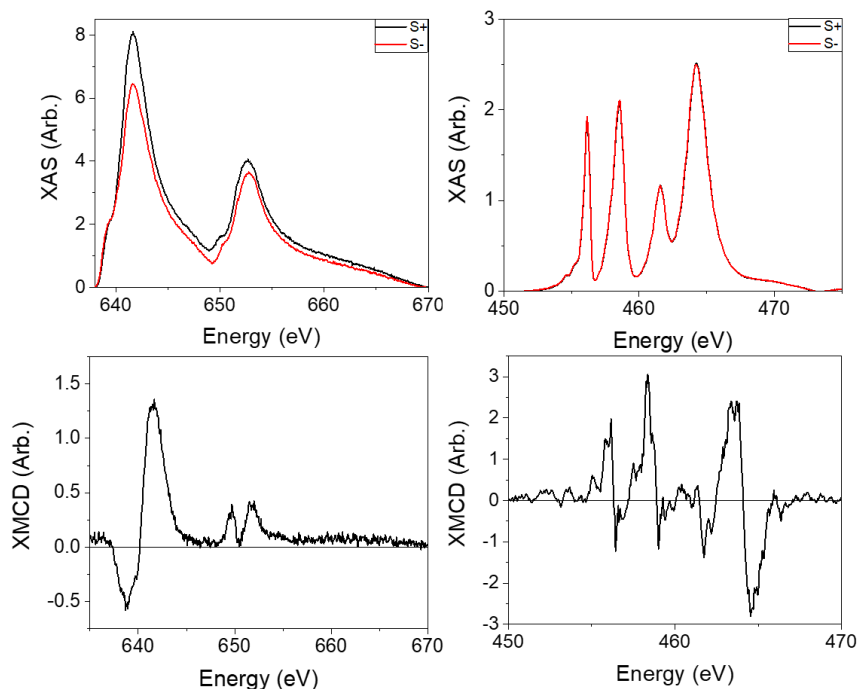
Figure 3.16: Upper panels: X-ray absorption spectra of a LSMO/BTO/LSMO trilayer measured in VEKMAG corresponding to the Mn (left) and Ti (Right) energies. Black lines are for right-handed circularly polarized light and red lines are for left-handed circularly polarized light. Lower panels: X-ray magnetic circular dichroism signal of Mn (left) and Ti (right). All the spectra were measured at 10K and with an applied field of 0.2T in the [100] direction.

This magnetic signal may be produced by a magnetic moment induced at the Ti due to the super-exchange interaction between the Mn, O and Ti atoms, in agreement with previous works [55]. Notice that the Y-axis is in arbitrary units and cannot be used to estimate the magnetic moment of the systems.

Polarized Neutron Reflectometry (PNR) measurements were performed to study the magnetic depth profile of the system [56] (See chapter 2). The measurements were performed at the Magnetism Reflectometer at the Spallation Neutron Source at Oak Ridge National Laboratory. The samples used had the same thicknesses as the ones patterned into junction devices. Figure 3.18.a shows the R^+ and R^- reflectivities, respectively the sample reflectivities for neutrons with polarization parallel and antiparallel to the applied field. A fit was also performed to the reflectivities in Figure 3.18a to a model that consists on a depth profile of the structural and magnetic parameters to each layer. The results of that fit are shown in Figure 3.18b. The saturation magnetization varies from the top LSMO layer (439 emu/cm^3) to the bottom layer (513 emu/cm^3). This suppressed magnetization may be due to the nucleation of oxygen vacancies in the top electrode. This, together with the reduced
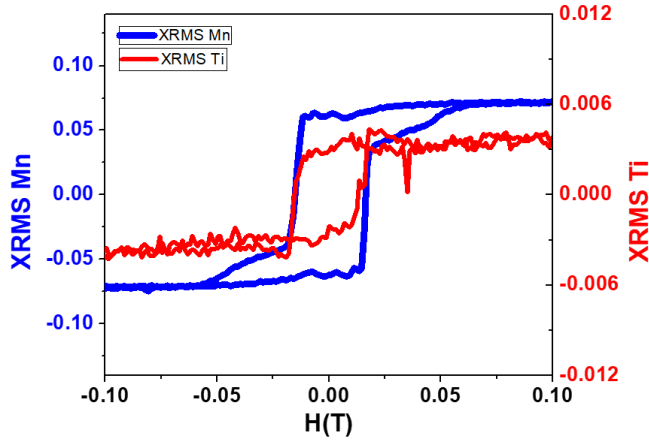
Figure 3.17: XRMS hysteresis loops measured in VEKMAG. The Mn loop (blue) was measured at 641.4 eV and the Ti loop (red) was measured at 464.6 eV, which are the $L_{2,3}$ edge energies for both elements. The loops were measured at 10K.

Curie temperature typically found in manganites at the interface [57], may explain why there is no Ti magnetic moment at the top BTO interface.

These results are in good agreement with previous experiments [58], where resistance was measured as a function of magnetic field, which was applied in the [110] easy axis. Abrupt switches were reported at the magnetic fields that corresponded to the coercive fields of both manganite layers. Tunnel magnetoresistance was calculated from the R vs. H curves using the formula:

$$TMR = \frac{R_{AP} - R_P}{R_P} \qquad (30)$$

TMR values were calculated as a function of the direction of the ferroelectric polarization. Ferroelectric polarization pointing up produced large TMR values, around 1000% at low T, meanwhile these values were deeply reduced when the polarization pointed down (yielding values of 10%). Studies of the barrier shape (using the Brinkman model [59] concluded that polarization switching had deep effects on the tunnel barrier shape, with a reduction of the thickness from 3.6nm when polarization points up, to 2nm when it points down. This change is induced by the ionization of oxygen vacancies, which is a process that changes the position of the Fermi level and, consequently, the barrier height. The suppression of TMR at low temperatures when the polarization points down is characteristic of spin filters.

The term spin-filter was firstly suggested by Esaki in 1967 [60], and later demonstrated in junctions with a ferromagnetic tunnel barrier [15,61]. Spin filtering is a phenomenon produced when spins up and down find a different barrier height
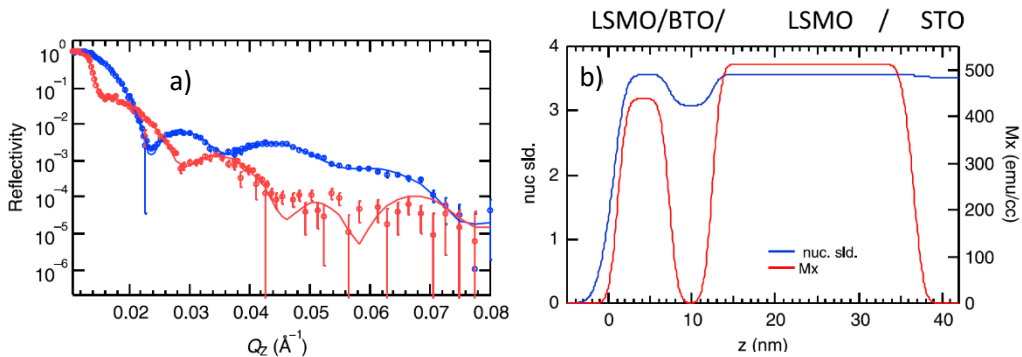
Figure 3.18: a) Polarized Neutron Reflectometry measured at 10K in an applied field of 1T. The Blue points are for R⁻ and the red points for R⁺ reflectivities. b) Depth profile of the nuclear scattering length density (blue) and magnetization (red) that corresponds to the fitting of the data shown in a).

when tunneling across it. This makes the electrons have different transmission probabilities as function of their spin and thus, polarizes the spin current.

In the case of our samples, the spin filtering behavior may come from the induced magnetic moment found in the Ti at the LSMO interface. At the interface, Ti orbitals hybridize with Mn orbitals via Ti-O-Mn superexchange enabled by the LaSrO/TiO_2 terminations. The alignment between Ti and Mn moments is antiparallel, as seen before [55]. The scheme of the orbital hybridization at the interface is shown in Figure 3.19. The d_{xz} and d_{yz} bands of the titanium hybridize with the t_{2g} ($\downarrow$) bands from the manganese. Notice that the t_{2g} band is split by Hund coupling interaction into spin up and spin down bands [62,63]. A strong hybridization produces between the occupied Mn $d(3z^2-r^2)$ and the empty $d(3z^2-r^2)$ band of Ti. Hybridization of t_{2g} bands of Ti and Mn also occurs, although to a lesser degree because of the smaller overlap of t_{2g} orbitals. The electronic occupation is as follows: Three of the manganese electrons occupy the $d(3z^2-r^2)$, the t_{2g} d(xz) and d(yz) hybrids. The Ti t_{2g} electron situates at the t_{2g} hybrid level with spin down, and thus the alignment will be antiferromagnetic. The superexchange process occurs between the Ti t_{2g} electrons and the Mn t_{2g} bands.

Finally, the spin filter results from the energy difference between the spin down (bonding) levels, marked with a dashed green line in the Figure 3.19, and the spin up (anti bonding) levels, at a higher energy than the previous, marked with a continuous grey line.
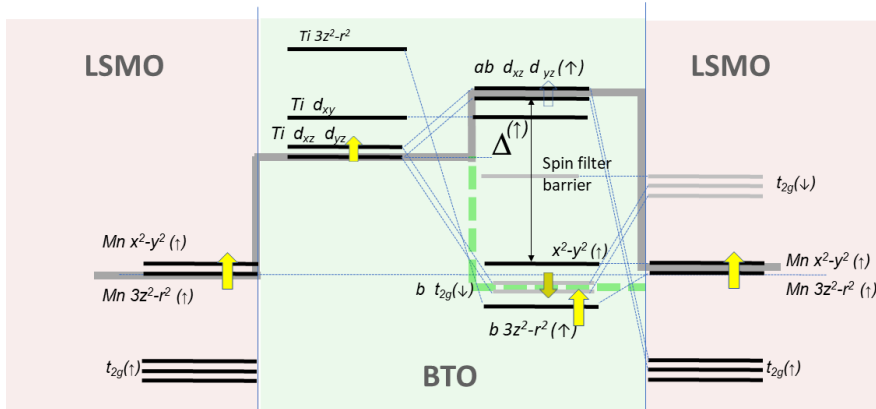
Figure 3.19: Orbitals scheme of the LSMO/BTO bonding at the right interface (bottom). The unpolarized dxz and dyz Ti bands hybridize with t_{2g} bands (spin up and spin down), splitted by the manganite exchange interaction. The grey line shows the barrier profile for spin up, and the green dashed line shows the barrier profile for electrons with spin down.

Note that this spin filtering behavior only occurs when the FE polarization is pointing down. This can be associated to the role of the oxygen vacancies ionization during the polarization switching process (Figure 3.20). When the polarization is pointing down, the oxygen vacancies generated at the top interface are ionized, and their associated electrons (and some oxygen vacancies) move towards the lower interface in order to screen the FE polarization charges. This partial metallization of the BTO bottom interface is responsible for the generation of magnetic moment in the titanium ions. This interfacial magnetism happens at the bottom interface due to the strong magnetic moment of the manganite. But the Mn magnetism is not so robust in the LSMO top layer. The depressed magnetism breaks the interfacial superexchange, and this suppress the interfacial magnetism of Ti. This may be the reason why spin filtering does not happen when polarization points towards the top interface.
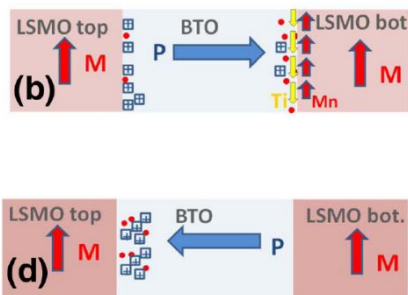

Figure 3.20: Scheme of the doping distribution along the tunnel barrier when the ferroelectric polarization is pointing down (a) and up (b). The switching of the polarization carries a simultaneous switching of the oxygen vacancies.

We have found in this system an interfacially induced spin filtering functionality. This behaviour is favoured by the accumulation of oxygen vacancies at the interface, which makes the Ti^{4+} species become Ti^{3+}, bonding to Mn across a Mn-O-Ti superexchange path.

4. Ferroionic induced interfacial superconductivity in tunnel junctions

In order to study the role of oxygen vacancies in interfacial properties of tunnel junctions, we fabricated multiferroic tunnel junctions based on the previous heterostructure, but replacing the top LSMO by a LSCO layer, which is a system that can act as an oxygen vacancies reservoir. We propose a strategy to arrive at a reduced complex-oxide phase in LSCO by exploiting the formation and migrating of oxygen vacancies in a ferroelectric tunnel junction as in a topotactic reaction [20,22,25,27,28]. As introduced before, we fabricated asymmetric tunnel junctions with the structure STO(100)//LSMO(30nm)/BTO(4.4nm)/LSCO(10nm), forming micron-size pillars combining optical lithography and ion milling techniques.

The transport across the ferroelectric barrier shows TER, which we are going to study at 100K. The procedure was to apply a 'writing voltage', V_{Write}, in a hysteretic sequence recording the resistance measured at a low voltage (V_{Read}=10mV) between write voltages. Figure 3.21 shows an electroresistance loop of the sample, where one can see two stable resistance states in the system as a function of the applied voltage. A high resistance state for negative voltages, and a low resistance state for positive voltages. The Tunneling Electroresistance (TER) was calculated, giving a large value of 10^5 %. These enormous values of TER have been obtained in asymmetric tunnel junctions composed of very different materials [64]. That is because ER has been attributed to asymmetries in the screening of the polarization charges by the two electrodes of the tunnel junction [3]. However, in our case, this cannot be the reason of the large electroresistance, because here the two electrodes, LSMO and LSCO, are expected to have similar screening lengths. Since LSCO is an oxygen vacancies reservoir, the switching of oxygen vacancies, combined with the ferroelectric polarization switch) may be responsible for the ER effect.

In the electroresistance cycle we can appreciate a gradual resistance increase at positive voltages just before the positive voltage switch, and also an equivalent depression before the negative voltage switch. These onsets correspond to a gradual displacement of oxygen vacancies across the BTO. However, the abrupt switches cannot be explained with oxygen vacancies movement only. Thus, ferroelectric polarization switches concurrently with oxygen vacancies [65,66].
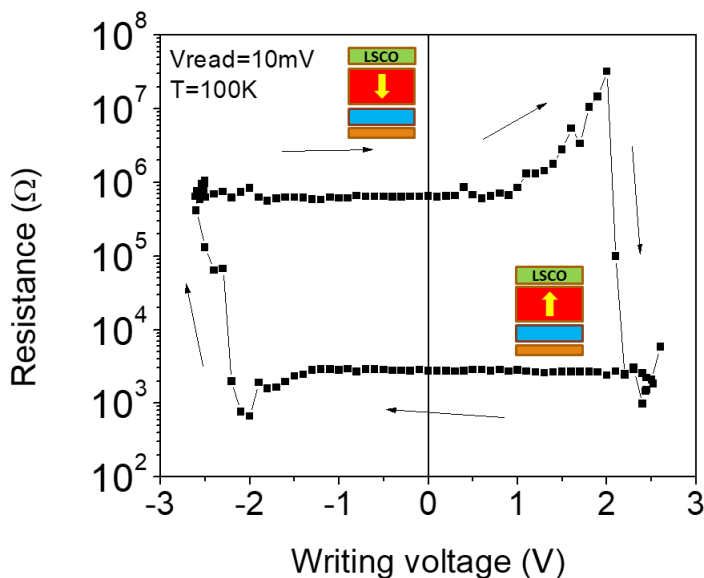
Figure 3.21: Electroresistance loop measured at 100K. The yellow arrows indicate the direction of the ferroelectric polarization for each resistance state of the systems.

Differential conductance measurements were taken at the two resistance states in order to study the low voltage dependence, as it is proportional to the shape of the tunnel barrier (Figure 3.22). The curves display a parabolic behavior, which is characteristic of tunneling transport. We appreciate that a strong voltage asymmetry appears in the low resistance state, which is not present in the high resistance state, denouncing a deep change in the shape of the tunnel barrier.

In order to study the evolution of the tunnel barrier effective shape, differential conductance curves were analyzed with the Brinkman-Dynes-Rowell model (BDR)
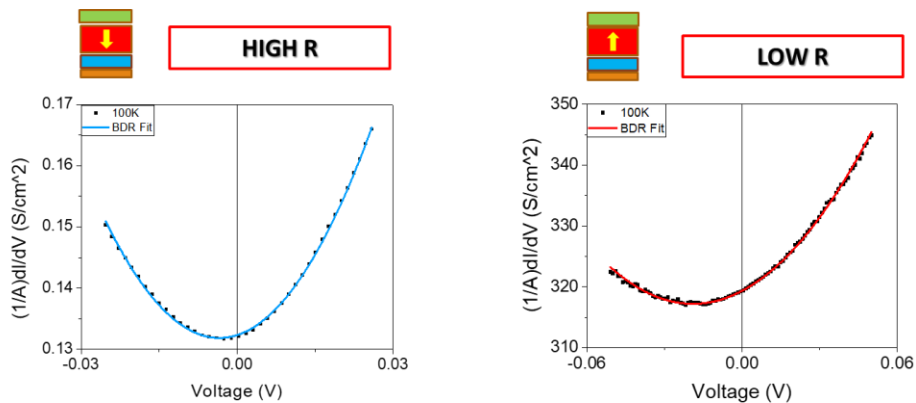

Figure 3.22: Points: Differential conductance vs. voltage measurements taken at 100K in the high (left) and low (right) resistance states. Lines are fits to the Brinkmann, Dynes and Rowell model.

for a trapezoidal tunnel barrier [59]. In this method, and assuming WKB approximation [67], which implies that the band structure of the M-I-M system varies slowly compared to the electron wavelength, the conductance is given by:

$$\frac{G(V)}{G(0)} = 1 - \left(\frac{A_0 \Delta\varphi}{16 \varphi^{3/2}}\right) eV + \left(\frac{9}{128}\frac{A_0^2}{\varphi}\right)(eV)^2 \qquad (31)$$
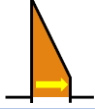
Where φ is the average barrier height, $\Delta\varphi = \varphi_2 - \varphi_1$ is the barrier asymmetry,

$$A_0 = 4(2m)^{1/2}d/3\hbar, \text{ and} \qquad (32)$$

$$G(0) = (3.16 \cdot 10^{10} \cdot \varphi^{1/2}/t)e^{(-1.025 \cdot t \cdot \varphi^{1/2})} \qquad (33)$$

where t is the barrier thickness in Å and φ the voltage in volts.

Table 1: Tunnel barrier shape parameters obtained in the BDR fitting to the differential conductance curves in the high and low resistance states of the tunnel junction

State	φ (meV)	Δφ (meV)	t (nm)	Barrier shape
HRS	210	54	4.5	
LRS	622	430	1.8	

Fits to this model are present in Figure 3.22 as lines in the differential conductance plots. These fits quantify the height and the asymmetry of the tunnel barrier. The data obtained and the estimation of the barrier shapes are in Table I.

In the HRS, the barrier thickness obtained is 4.5nm, in very good agreement with the nominal thickness of BTO, which is 4.4nm. The barrier height is 210 meV, with a small asymmetry (Δφ=54 meV). On the other hand, in the LRS, a much larger average barrier height was obtained, φ=622 meV, with also a strong asymmetry (Δφ=430meV). The barrier thickness is t=1.8nm, much smaller in this state. These changes in the barrier dimensions account for the large electroresistance found. In fact, they demonstrate that the oxygen vacancies ionization is driven by the ferroelectric polarization switching, outlining the role of the ferroionic coupling in a mixed electrochemical-ferroelectric state [6]. The height of a tunnel barrier is determined by the distance from the Fermi level to the edge of the conduction band. In BTO, at equilibrium, the Fermi level lies above the donor level of oxygen vacancies, which is 0.4 eV below the conduction band edge. These oxygen vacancies should be weakly ionized at the temperature of the experiment in the HRS,

explaining the low barrier height in this state. On the other hand, a strong increase is produced in the barrier height when the system switches to the LRS, this, together with the strong asymmetry, indicates a much stronger ionization of the oxygen vacancies at the bottom interface than at the top interface. The difference in the ionization between the two interfaces is due to the ferroelectric polarization and occurs to screen polarization charges. When the polarization is pointing up, the oxygen vacancies generated at the bottom interface get ionized, donating electrons to the top interface to screen the polarization charges. That in turn reduces the barrier width. For negative electric fields (FE polarization pointing down), the oxygen vacancies abandon the interface, and the screening is carried out by the holes of the LSCO. This yields a more symmetric tunnel barrier. These two states are schematically presented in the Figure 3.23.

The temperature dependence of the transport properties was also measured for the two resistance states. Current vs. voltage and differential conductance measurements were taken between -100mV and +100mV in a temperature range between 5K and 200K. The IV curves (Figure 3.24 left panels) show a non-linear dependence which is more pronounced at low temperatures. This is the typical behavior of a current across a tunnel barrier. We can see that at the LRS, the curve is almost linear, and this is in agreement with the thinner barrier found in this state.

At low temperatures, the differential conductance plots (g(V)) display a conductance suppression near low voltages that suggests the opening of a temperature dependent gap (Figure 3.24 right panels). This gap seen to be present in the two resistance states of the system. In order to clarify the dimensions of the gap in both resistance states, the conductance plots were normalized to their value at 40mV (G= (g)/(g(40mV))) and corrected for the normal state conductance by dividing each curve below 100K by the 100K one (G/G_N(100K)). When we do this, a clear gap

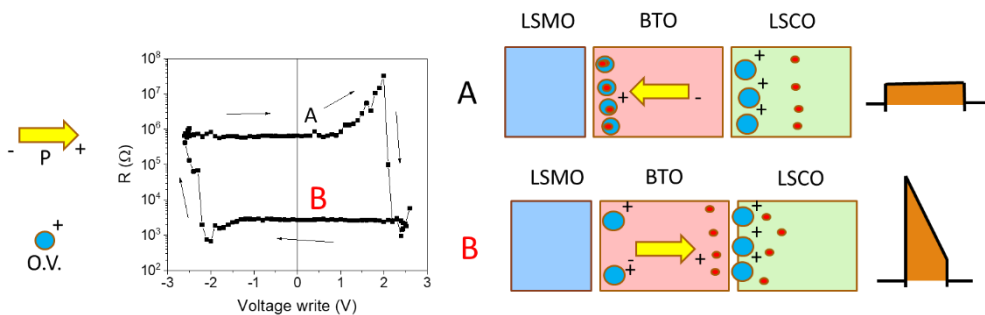*Figure 3.23: A: Scheme of the screening charges distribution in the junction when the ferroelectric polarization points down. The oxygen vacancies inside the BTO are neutralized and the screening is performed by the holes inside the LSCO. B: When the polarization points up, the oxygen vacancies get ionized inside the BTO and their electrons screen the polarization charges at the top interface.*
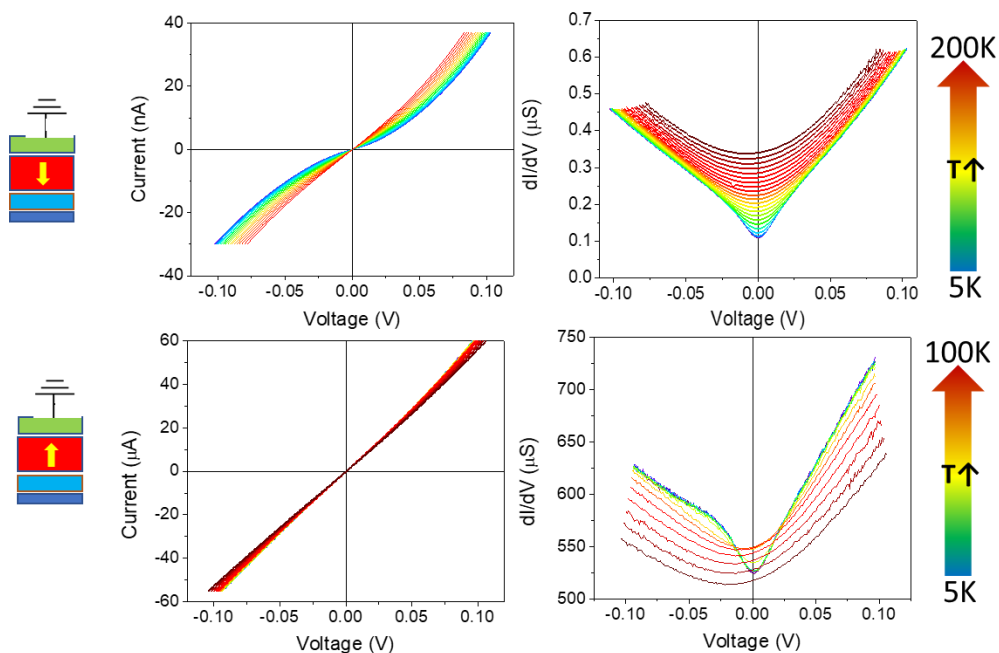
Figure 3.24: Current vs voltage (left panels) and differential conductance vs voltage (right panels) curves as a function of temperature when the sample is in the HRS (upper panels) and in the LRS (lower panels).

emerges in the HRS, resembling a superconducting gap (Figure 3.25 left panels). In the HRS (upper panel) the gap persists up to 80K and takes values of 50 mV, which are characteristic values of superconducting cuprates. The gap still appears in the LRS, but is shallower, reaching values of 30 mV of width, and closes at 40K (lower panel). The right panels of Figure 3.25 show the contour plots of differential conductance, which illustrate the differences of the gap features in the two resistance states. We can conclude that the interface superconducting state can be switched on and off by applying an electric field. In the HRS even appears quasiparticle peaks around 40 meV (Figure 3.26).

This gap has been observed in three more samples, one of them with silver instead of gold as top electrode (See appendix 2), but in another sample, with lower conductance in the initial state, a conductance enhancement is present at small bias, instead of a conductance suppression (Figure 3.27). The conductance enhancement remains until temperature exceeds 60K and until voltage exceeds 40 mV. This behaviour is characteristic of the Andreev reflection in a metal/superconductor junction, and therefore strongly suggests the presence of a superconducting state at the interface [68,69]. In summary, switching between HRS and LRS, driven by the application of an electric field, modulates the superconducting properties of the LSCO interface.
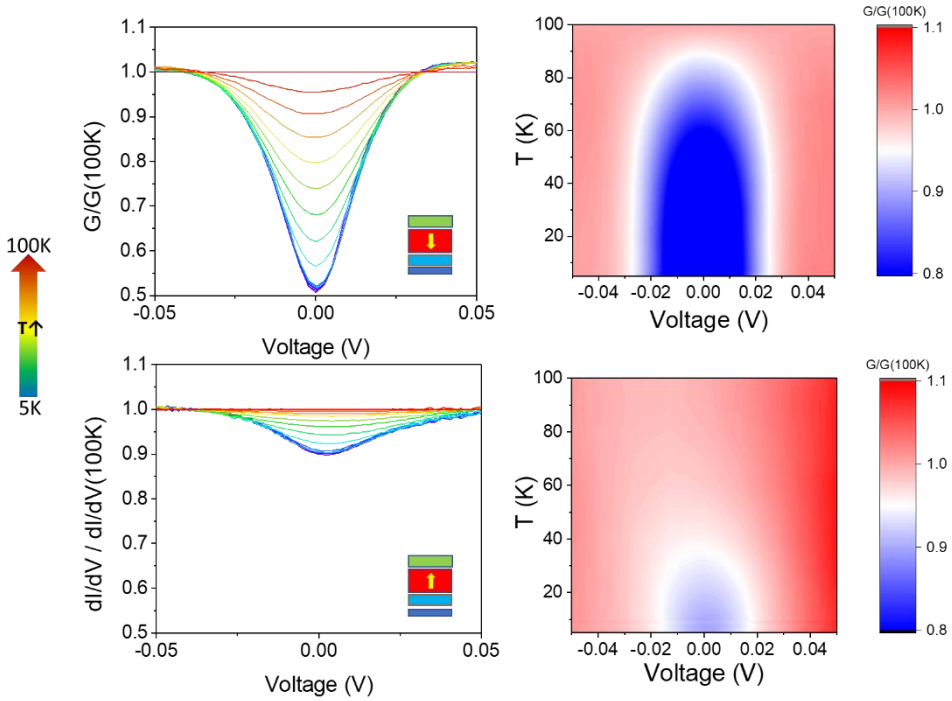
Figure 3.25: Left: Differential conductance curves normalized to the 100K curve for ferroelectric polarization pointing down (upper panel) and up (lower panel). Color code reflects temperature increase as shown in the left arrow. Right: Contour plots showing the emergence of a gap and its evolution with temperature for ferroelectric polarization pointing down (upper panel) and up (lower panel).

It is possible to analyse this phenomenon in the frame of the Bloder-Tinkham-Klapwijk (BTK) [70] theory for superconductor/metal junctions (Figure 3.28). The fittings were performed by Kevin Seurre in the group of Javier E. Villegas in Unité Mixte de Physique, CNRS, Thales, Université Paris-Saclay. This theory explains the special features of conductance spectra associated to the superconducting gap (Δ) in terms of a Z parameter, which measures the strength of the junction's barrier. As Z increases, the junction transparency reduces. The transparency is defined in terms of the mismatch of Fermi velocities at the normal and superconductor sides; also, it can be defined as the strength of the oxide barrier in a tunnel junction.

The used fit for both resistance states is a BTK modified version for d-wave superconductors extended to the case of c-axis tunneling [71,72]. According to the peak structure of the system, it can be interpreted as a spectral convolution of the d-wave quasiparticle DOS, which gives a V-shaped gap broadening and the quasi-2D normal-state DOS, which has a logarithmic singularity near the Fermi level. The conductance expression is as follows:
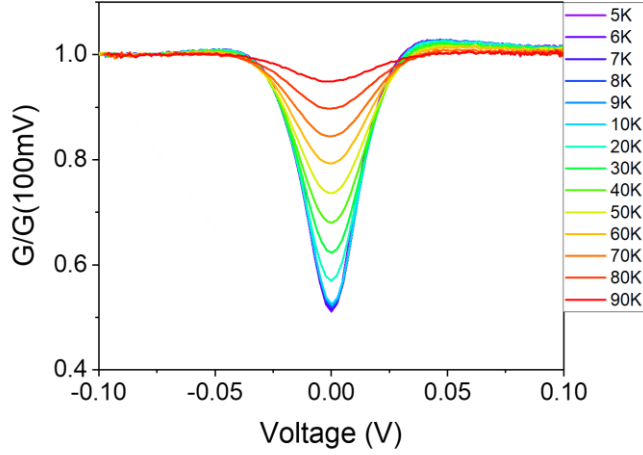
Figure 3.26: Enlarged view of the normalized differential conductance of the junction from figure 3.25 left upper panel. Quasiparticle peaks are observed at low temperatures.

$$\tilde{\sigma}_s(E,\theta) = \frac{16(1+|\Gamma_+|^2)\cos^4\theta + 4Z^2(1-|\Gamma_+\Gamma_-|^2)\cos^2\theta}{|4\cos^2\theta + Z^2[1-\Gamma_+\Gamma_- e^{(i\varphi_- - i\varphi_+)}]|^2} \tag{34}$$

Where Z is the barrier strength, $\Gamma_\pm = \left(\frac{E}{\Delta_\pm}\right) - \sqrt{\left(\frac{E}{|\Delta_\pm|}\right)^2 - 1}$, and $e^{(i\varphi_\pm)} = \Delta_\pm/|\Delta_\pm|$.

This expression represents the phase of the pair potential experienced by an Andreev-reflected electron (or hole) propagating at an angle θ relative to the junction normal. The tunneling current is also proportional to a parameter β, which in case of an interface in the Normal/Insulator/Superconductor limit, is rather small. In addition to the bare extended BTK model, broadening effects were considered, in particular the effect of quasiparticle lifetime [73,74], which can be quantified by

Figure 3.27: Left: Zero bias peak present in another junction at low temperatures and bias. The peak persists until 60K. At high voltages (right) the behavior reminds of a typical tunnel junction.

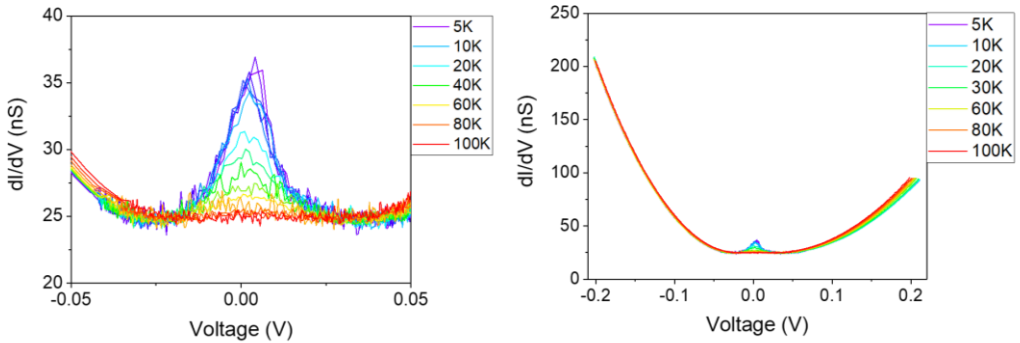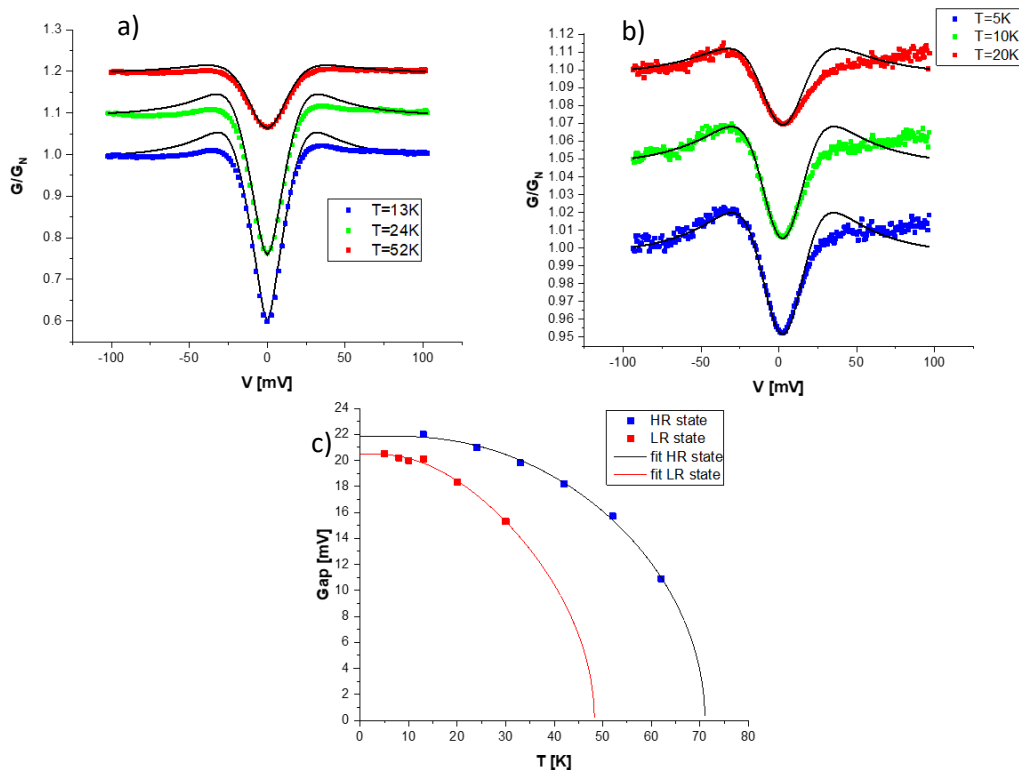*Figure 3.28: Manifestation of superconductivity in the high and low resistance states (respectively HR and LR). a) Normalized conductance of the HR state (scatter) and the extended BTK-simulation (line) [69] with Z=30 for T=13,24 and 52K. b) Normalized conductance of the LR state (scatter) and the extended BTK-simulation (line) with Z=1.7 for T=5,10 and 30K. c) Extracted value of the superconducting gap for the two states (scatter) and their fit (line) [73] to determine an estimate of the critical temperature T_c. For the HR state, $T_c \approx 71K$ and for the LR state, $T_c \approx 48K$.*

means of a phenomenological parameter Γ. As seen in the Figure 3.28, the data are in good correlation with the BTK theory for the state with the enhanced superconductivity, whereas shows a symmetric behavior which does not correspond to the real measurements for the depressed-superconductivity state. This difference may be due to the fact that the BTK theory applies only for Normal/Superconductor interfaces. The values obtained from the BTK fitting are summarized in the Table 2. If this study is carried out at several temperatures, one can obtain the temperature evolution of the superconducting gap. These plots show familiar behaviour [48] as shown in the inset to Figure 3.28b. In the high resistance state the gap closes at a temperature slightly exceeding 70K, while in the low resistance state it closes below 50K. Within the BTK theory, this may be interpreted as Z being larger in the in the HRS than in the LRS in agreement with our results.

Table 2: Parameters obtained from the BTK fitting to the differential conductance measurements.

T=5K	Z	Δ	Γ
HRS	22	10.5	8
LRS	2.42	22	22

A fitting was performed to deduce the Tc of the superconducting state for the high and low resistance states (Figure 3.28c) as done in [75]. Here we can estimate a critical temperature of Tc=70K for the HRS, which is very similar to that in YBCO, and Tc=50K for the LRS.

The sample with a conductance enhancement at low voltages has been fitted with the BTK model, as can be seen in Figure 3.29. This zero bias peak appears in d-wave superconductor/metal interface where the superconducting parameter makes an angle of 45° with the interface (α=π/4) [72]. The change of sign of the order parameter for the incident and reflected quasiparticle results in the formation of quasiparticle bound states at the interface between the superconductor and the metal. This resonant zero energy bound states dominate the tunneling process at low bias and gives rise to the peak at zero bias. Such a geometric tunneling configuration requires that the epitaxial growth is locally modified to expose the nodes of the order parameter to the tunneling cone. A situation favored by the rather high density of stacking faults observed in the high resolution microscopy images of the heterostructure in Figure 3.7b, which probably result from the transfer of oxygen vacancies. The finding of the two different features, the gap-like behavior and the zero bias conductance peak in this system strongly supports the existence of a superconducting state at the BaTiO$_3$-cuprate interface which is modulated by the resistive switching.

The transfer of OV from the cuprate to the ferroelectric produces structural modifications besides the doping effect and are crucial for the stabilization of the superconducting state. For example, it can be observed in the microscopy image (Figure 3.7b) that the buckling of the lattice planes induced by oxygen vacancies is suppressed, indicating that the depletion of OV is accompanied by structural changes. The OV are known to be the origin of the lack of superconductivity of the LSCO cuprate. It has been proposed that their electron doping field compensate the effect of the holes introduce by the Sr doping, and because of that, the CuO$_2$ planes never reach the doping level necessary to start superconducting. Furthermore, the arrays of oxygen vacancies lining up along a and b directions of the unit cell break the necessary connectivity of CuO$_6$ octahedra keeping the 3D transport metallic, although anisotropic, but hindering the nucleation of superconductivity [36].

OV transfer across the junction produces a strong modification of doping at the cuprate interface, which is also modulated by the coupled switching of ferroelectric polarization and oxygen vacancies. If the 3.9 oxidation state over the whole BTO barrier is caused by the transfer of oxygen vacancies from the (whole) 10 nm thick cuprate layer, this would produce a hole doping of 6.6 10^{20} cm^{-3} which will be
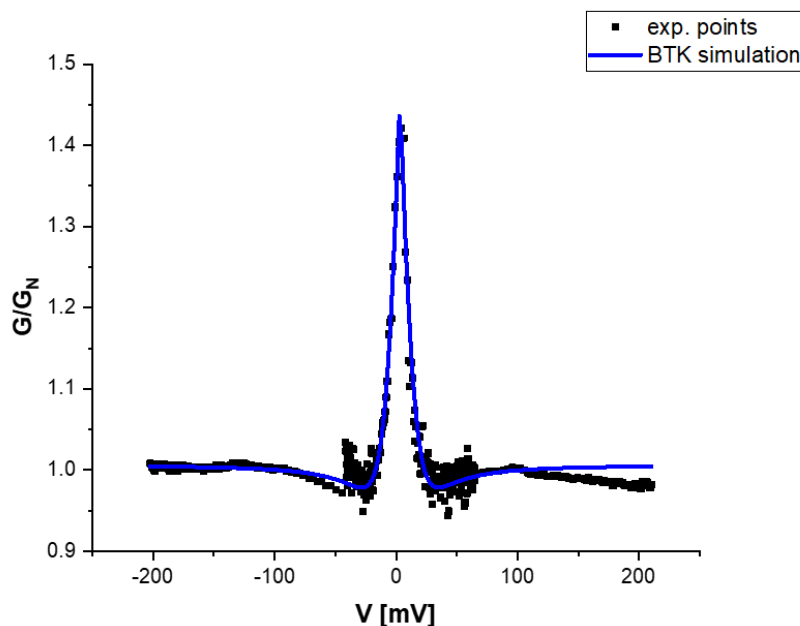
Figure 3.29: Normalized conductance of one particular sample and a simulation with the extended BTK method for d-wave superconductors. This zero bias conductance peak is typical of d-wave superconductor/metal interface where the superconducting order parameter makes an angle of 45° with the interface [69]. This peak results from the formation of quasiparticle bound states at the interface between the superconductor and the metal.

modulated at the interface layer by ferroelectric field effect. It is precisely in the high resistance state where the larger gap is observed, that the cuprate will be strongly hole doped by the depletion of oxygen vacancies and the screening of the negative (down) polarization charges (Figure 3.23). As discussed above, these vacancies transferred to the BTO are weakly ionized in a way dictated by the ferroelectric polarization, and consequently the barrier remains insulating. On the other hand, in the low resistance state, with a smaller gap, oxygen vacancies have been partially swept to the cuprate and polarization is pointing up, what favors less hole doping of the interface. Now polarization is partially screened by the oxygen vacancies remaining in the barrier (what increases their ionization) and thus contribute less to electron doping of the cuprate.

In summary, we have found fingerprints of superconductivity at the interface between a non-superconducting cuprate and a ferroelectric barrier in a tunnel junction. Both the energy size and the temperature range of the gap suggests a high critical temperature of 80 K in a cuprate where superconductivity had never been found before. We propose that the transfer of oxygen vacancies from the cuprate interface to the titanate barrier triggered by the modulation of the lattice expansion at both sides of the interface, plays a major role on the stabilization of the superconducting phase. In addition, the coupled switching of ferroelectric

polarization and oxygen vacancies produce a strong doping modulation at the interface layers resulting from the combined effect of the doping field of the oxygen vacancies and the field effect to screen the ferroelectric polarization.

5. Conclusions

We have fabricated multiferroic tunnel junctions in order to study the interfacial interaction between different complex oxides. We found that oxygen vacancies play an important role in the properties of the tunnel junctions due to carrier doping, generating a spin filter behavior in a symmetric tunnel junction. This functionality arises from a superexchange interaction between the manganese, the oxygen and the titanium at the interface. In order to clarify the participation of oxygen vacancies in the generation of novel interfacial properties, we fabricated tunnel junctions replacing the top LSMO by a LSCO layer, which is an oxygen vacancies reservoir, finding a superconducting fingerprint in the interface of the cuprate. Probably the local transfer of oxygen vacancies from the cuprate to the titanate produces the necessary doping effect to stabilize the superconducting phase on the cuprate. We have found a coupling between the oxygen vacancies and the ferroelectric polarization switching, so the doping at the interface may be a combination of the doping field of the oxygen vacancies and the field effect of the charges that screen the ferroelectric polarization. In view of these results, we conclude that the generation of the superconducting phase at the interface goes far beyond the effect of doping. Furthermore, the ferroionic doping route appears as a promising new strategy to explore phase diagrams at doping levels beyond the ones reached with field effect or even ionic liquid doping.

6. References

[1]   J. Chakhalian, A. J. Millis, and J. Rondinelli, Nat. Mater. **11**, 92 (2012).

[2]   J. P. Veev, C. G. Duan, J. D. Burton, A. Smogunov, M. K. Niranjan, E. Tosatti, S. S. Jaswal, and E. Y. Tsymbal, Nano Lett. **9**, 427 (2009).

[3]   M. Y. Zhuravlev, R. F. Sabirianov, S. S. Jaswal, and E. Y. Tsymbal, Phys. Rev. Lett. **94**, 1 (2005).

[4]   E. Y. Tsymbal and H. Kohlstedt, Science (80-.). **313**, 181 (2006).

[5]   S. V. Kalinin and N. A. Spaldin, Science (80-.). **341**, 858 (2013).

[6]   S. M. Yang, A. N. Morozovska, R. Kumar, E. A. Eliseev, Y. Cao, L. Mazet, N. Balke, S. Jesse, R. K. Vasudevan, C. Dubourdieu, and S. V. Kalinin, Nat. Phys. **13**, 812 (2017).

[7]   V. Garcia, M. Bibes, L. Bocher, S. Valencia, F. Kronast, A. Crassous, X. Moya, S. Enouz-Vedrenne, A. Gloter, D. Imhoff, C. Deranlot, N. D. Mathur, S. Fusil, K. Bouzehouane, and A. Barthelemy, Science (80-.). **327**, 1106 (2010).

[8]   Z. Wen, C. Li, D. Wu, A. Li, and N. Ming, Nat. Mater. **12**, 617 (2013).

[9]   A. Chanthbouala, A. Crassous, V. Garcia, K. Bouzehouane, S. Fusil, X. Moya, J. Allibe, B. Dlubak, J. Grollier, S. Xavier, C. Deranlot, A. Moshar, R. Proksch, N. D. Mathur, M. Bibes, and A. Barthélémy, Nat. Nanotechnol. **7**, 101 (2012).

[10]   X. S. Gao, J. M. Liu, K. Au, and J. Y. Dai, Appl. Phys. Lett. **101**, 142905 (2012).

[11]   A. Chanthbouala, V. Garcia, R. O. Cherifi, K. Bouzehouane, S. Fusil, X. Moya, S. Xavier, H. Yamada, C. Deranlot, N. D. Mathur, M. Bibes, A. Barthélémy, and J. Grollier, Nat. Mater. **11**, 860 (2012).

[12]   D. J. Kim, H. Lu, S. Ryu, C. W. Bark, C. B. Eom, E. Y. Tsymbal, and A. Gruverman, Nano Lett. **12**, 5697 (2012).

[13]   A. Zenkevich, M. Minnekaev, Y. Matveyev, Y. Lebedinskii, K. Bulakh, A. Chouprik, A. Baturin, K. Maksimova, S. Thiess, and W. Drube, Appl. Phys. Lett. **102**, (2013).

[14]   Y. W. Yin, J. D. Burton, Y. M. Kim, A. Y. Borisevich, S. J. Pennycook, S. M. Yang, T. W. Noh, A. Gruverman, X. G. Li, E. Y. Tsymbal, and Q. Li, Nat. Mater. **12**, 397 (2013).

[15]   M. Gajek, M. Bibes, S. Fusil, K. Bouzehouane, J. Fontcuberta, A. Barthélémy, and A. Fert, Nat. Mater. **6**, 296 (2007).

[16]   C. G. Duan, S. S. Jaswal, and E. Y. Tsymbal, Phys. Rev. Lett. **97**, 13 (2006).

[17]   J. D. Burton and E. Y. Tsymbal, Phys. Rev. Lett. **106**, 1 (2011).

[18]   J. G. Bednorz and K. A. Müller, in *Prop. Perovskites Other Oxides* (WORLD SCIENTIFIC, 2010), pp. 545–562.

[19]   R. J. Cava, J. Am. Ceram. Soc. **83**, 5 (2000).

[20]   K. R. Poeppelmeier, M. E. Leonowicz, J. C. Scanlon, and B. Yelon, J. Solid State Chem. **79**, 71 (1982).

[21]   F. Millange, V. Caignaert, B. Domengès, B. Raveau, and E. Suard, Chem. Mater. **10**, 1974 (1998).

[22]   J. A. Alonso and M. J. Martínez-Lope, J. Chem. Soc. Dalt. Trans. 2819 (1995).

[23]   M. James and J. P. Attfield, Phys. C Supercond. Its Appl. **235**–**240**, 751 (1994).

[24]   R. J. Cava, H. Takagi, J. J. Krajewski, W. F. Peck, and H. Y. Hwang, Phys. Rev. B **47**, 11525 (1993).

[25]   M. A. Hayward, M. A. Green, M. J. Rosseinsky, and J. Sloan, J. Am. Chem. Soc. **121**, 8843 (1999).

[26]   G. A. Sawatzky, Nature **572**, 592 (2019).

[27]   D. Li, K. Lee, B. Y. Wang, M. Osada, S. Crossley, H. R. Lee, Y. Cui, Y. Hikita, and H. Y. Hwang, Nature **572**, 624 (2019).

[28]   J. Zhang, A. S. Botana, J. W. Freeland, D. Phelan, H. Zheng, V. Pardo, M. R. Norman, and J. F. Mitchell, Nat. Phys. **13**, 864 (2017).

[29]   M. Hepting, D. Li, C. J. Jia, H. Lu, E. Paris, Y. Tseng, X. Feng, M. Osada, E. Been, Y. Hikita, Y. D. Chuang, Z. Hussain, K. J. Zhou, A. Nag, M. Garcia-Fernandez, M. Rossi, H. Y. Huang, D. J. Huang, Z. X. Shen, T. Schmitt, H. Y. Hwang, B. Moritz, J. Zaanen, T. P. Devereaux, and W. S. Lee, Nat. Mater. **19**, (2020).

[30]   Y. Tokura, J. B. Torrance, A. I. Nazzal, T. C. Huang, and C. Ortiz, J. Am. Chem. Soc. **19**, 7555 (1988).

[31]   H.-C. Yu and K.-Z. Fung, in *Proc. 8th Int. Symp. Solid State Fuel Cells VIII*, edited by C. Singhal and M. Dokiya (n.d.), pp. 591–600.

[32]   J. F. Bringley, B. A. Scott, S. J. La Placa, R. F. Boehme, T. M. Shaw, M. W. McElfresh, S. S. Trail, and D. E. Cox, Nature **347**, 263 (1990).

[33]   J. F. Bringley, B. A. Scott, S. J. La Placa, T. R. McGuire, F. Mehran, M. W.

McElfresh, and D. E. Cox, Phys. Rev. B **47**, 15269 (1993).

[34]   H. C. Yu and K. Z. Fung, J. Mater. Res. **19**, 943 (2004).

[35]   S. Darracq, S. G. Kang, J. H. Choy, and G. Demazeau, J. Solid State Chem. **114**, 88 (1995).

[36]   J. B. Torrance, Y. Tokura, A. Nazzal, and S. S. P. Parkin, Phys. Rev. Lett. **60**, 542 (1988).

[37]   T. Mamiya, K. Hattori, H. Shibayama, K. Iwahashi, T. Kusakabe, and K. Adachi, Phys. B Phys. Condens. Matter **194**–**196**, 1523 (1994).

[38]   C. Michel, L. E. Rakho, M. Hervieu, J. Pannetier, and B. Raveau, J. Solid State Chem. **68**, 143 (1987).

[39]   M. Varela, Z. Sefrioui, D. Arias, M. A. Navacerrada, M. Lucía, M. López de la Torre, C. León, G. D. Loos, F. Sánchez-Quesada, and J. Santamaría, Phys. Rev. Lett. **83**, 3936 (1999).

[40]   M. Varela, W. Grogger, D. Arias, Z. Sefrioui, C. León, C. Ballesteros, K. M. Krishnan, and J. Santamaría, Phys. Rev. Lett. **86**, 5156 (2001).

[41]   G. Sanchez-Santolino, J. Tornos, D. Hernandez-Martin, J. I. Beltran, C. Munuera, M. Cabero, A. Perez-Muñoz, J. Ricote, F. Mompean, M. Garcia-Hernandez, Z. Sefrioui, C. Leon, S. J. Pennycook, M. C. Muñoz, M. Varela, and J. Santamaria, Nat. Nanotechnol. **12**, 655 (2017).

[42]   E. Stoyanov, F. Langenhorst, and G. Steinle-Neumann, Am. Mineral. **92**, 577 (2007).

[43]   J. Garcia-Barriocanal, F. Y. Bruno, A. Rivera-Calzada, Z. Sefrioui, N. M. Nemes, M. Garcia-Hernández, J. Rubio-Zuazo, G. R. Castro, M. Varela, S. J. Pennycook, C. Leon, and J. Santamaria, Adv. Mater. **22**, 627 (2010).

[44]   J. Salafranca, J. Rincón, J. Tornos, C. León, J. Santamaria, E. Dagotto, S. J. Pennycook, and M. Varela, Phys. Rev. Lett. **112**, 1 (2014).

[45]   N. Gauquelin, D. G. Hawthorn, G. A. Sawatzky, R. X. Liang, D. A. Bonn, W. N. Hardy, and G. A. Botton, Nat. Commun. **5**, 1 (2014).

[46]   Y. Wang, X. Liu, J. D. Burton, S. S. Jaswal, and E. Y. Tsymbal, Phys. Rev. Lett. **109**, 1 (2012).

[47]   Y. Xiao, V. B. Shenoy, and K. Bhattacharya, Phys. Rev. Lett. **95**, 1 (2005).

[48]   S. B. Adler, J. Am. Ceram. Soc. **84**, 2117 (2004).

[49]   E. K. H. Salje, ChemPhysChem **11**, 940 (2010).

[50]   J. Kadlec, Solid State Electron. **17**, 469 (1974).

[51]   J. S. Noh, T. K. Nath, C. B. Eom, J. Z. Sun, W. Tian, and X. Q. Pan, Appl. Phys. Lett. **79**, 233 (2001).

[52]   T. Noll and F. Radu, Proc. MEDSI2016 370 (2017).

[53]   J. Tornos, F. Gallego, S. Valencia, Y. H. Liu, V. Rouco, V. Lauter, R. Abrudan, C. Luo, H. Ryll, Q. Wang, D. Hernandez-Martin, G. Orfila, M. Cabero, F. Cuellar, D. Arias, F. J. Mompean, M. Garcia-Hernandez, F. Radu, T. R. Charlton, A. Rivera-Calzada, Z. Sefrioui, S. G. E. Te Velthuis, C. Leon, and J. Santamaria, Phys. Rev. Lett. **122**, 37601 (2019).

[54]   D. Raoux, N. Jaouen, J. M. Tonnerre, and E. Bontempi, Acta Phys. Pol. A **98**, 483 (2000).

[55]   Y. Liu, J. Tornos, S. G. E. Te Velthuis, J. W. Freeland, H. Zhou, P. Steadman, P. Bencok, C. Leon, and J. Santamaria, APL Mater. **4**, 0 (2016).

[56]   Y. Zhu, *Modern Techniques for Characterizing Magnetic Materials* (2005).

[57]   V. Garcia, M. Bibes, A. Barthélémy, M. Bowen, E. Jacquet, J. P. Contour, and A. Fert, Phys. Rev. B - Condens. Matter Mater. Phys. **69**, 1 (2004).

[58]   J. T. Castillo, Spin-Dependent Transport in Oxide Multiferroic Tunnel Junctions, Universidad Complutense de Madrid, 2014.

[59]   W. F. Brinkman, R. C. Dynes, and J. M. Rowell, J. Appl. Phys. **41**, 1915 (1970).

[60]   L. Esaki, P. J. Stiles, and S. Von Molnar, Phys. Rev. Lett. **19**, 852 (1967).

[61]   J. S. Moodera, X. Hao, G. A. Gibson, and R. Meservey, Phys. Rev. Lett. **61**, 637 (1988).

[62]   S. Okamoto, Phys. Rev. B - Condens. Matter Mater. Phys. **82**, 1 (2010).

[63]   J. Garcia-Barriocanal, J. C. Cezar, F. Y. Bruno, P. Thakur, N. B. Brookes, C. Utfeld, A. Rivera-Calzada, S. R. Giblin, J. W. Taylor, J. A. Duffy, S. B. Dugdale, T. Nakamura, K. Kodama, C. Leon, S. Okamoto, and J. Santamaria, Nat. Commun. **1**, (2010).

[64]   V. Garcia, S. Fusil, K. Bouzehouane, S. Enouz-Vedrenne, N. D. Mathur, A. Barthélémy, and M. Bibes, Nature **460**, 81 (2009).

[65]   R. Waser and M. Aono, Nat. Mater. **6**, 833 (2007).

[66]   R. Waser, R. Dittmann, C. Staikov, and K. Szot, Adv. Mater. **21**, 2632 (2009).

[67]   W. A. Harrison, Phys. Rev. **123**, 85 (1961).

[68] R. J. Soulen, J. M. Byers, M. S. Osofsky, B. Nadgorny, T. Ambrose, S. F. Cheng, P. R. Broussard, C. T. Tanaka, J. Nowak, J. S. Moodera, A. Barry, and J. M. D. Coey, Science (80-.). **282**, 85 (1998).

[69] Michael Tinkham, Introd. to Supercond. 454 (1996).

[70] G. E. Blonder, M. Tinkham, and T. M. Klapwijk, Phys. Rev. B **25**, 4515 (1982).

[71] J. Y. T. Wei, N. C. Yeh, D. F. Garrigus, and M. Strasik, Phys. Rev. Lett. **81**, 2542 (1998).

[72] S. Kashiwaya, Y. Tanaka, M. Koyanagi, H. Takashima, and K. Kajimura, Phys. Rev. B **51**, 1350 (1995).

[73] R. C. Dynes, V. Narayanamurti, and J. P. Garno, Phys. Rev. Lett. **41**, 1509 (1978).

[74] A. Pleceník, M. Grajcar, A. Beňačka, P. Seidel, and A. Pfuch, Phys. Rev. B **49**, 10016 (1994).

[75] W. K. Park, L. H. Greene, J. L. Sarrao, and J. D. Thompson, Phys. Rev. B - Condens. Matter Mater. Phys. **72**, 6 (2005).

References

Chapter 4: Electric-field controlled correlations and emergent ferromagnetism in SrIrO3 ultrathin layers

1. Introduction

Materials with correlated electrons are a very interesting source of different phenomena like high Tc superconductivity, metal-insulator transitions or ferroic behavior. More specifically, 5d oxides have recently attracted a great deal of attention due to the possibility of generating new electronic ground states [1–3]. This is because, in some compounds the coulomb repulsion, the characteristic energy for bandwidth and spin orbit interaction falls in the same range, between 0.3 and 0.4 eV, thus generating some exotic electronic phases that result from their interplay. One important property of these 5d Transition Metal Oxides (TMOs) is the large spatial extent of the d-electron orbitals. The latter is responsible for the interactions between the d-orbitals of the transition metal and the p-orbitals of the oxygens, leading to an enhanced d-p hybridization. This interplay results in narrow d-bands. This is the feature that makes the 4d and the 5d oxides very sensitive to electron-electron interactions. The combination between extremely correlated narrow bands (which have a small bandwidth (W)) with a large Coulomb repulsion (U) can have an important role in the electronic structure of these systems. It has recently been observed that the SOC constant is 0.3-0.4 eV in 5d TMOs, much larger than in 3d-TMOs (20 meV), and U is in the vicinity of 0.5 eV.

According to the Hubbard model, the strongly correlated systems can be characterized by the U-W ratio:

-If W<<U the system will be insulating

-if W≥U an Insulator-Metal transition (IMT) occurs and the system becomes metallic.

This W-U ratio can be controlled with the dimensionality. The I-M transition happens between $Sr_3Ir_2O_7$ and $SrIrO_3$, which are the n=2 and the n=∞ members of the Ruddlesden-Popper series $Sr_{n+1}Ir_nO_{3n+1}$. Its first member, the Sr_2IrO_4 is a spin orbit Mott insulator [4–6]. $Sr_2Ir_1O_4$ shows a metallic behavior below 120K and a strongly anisotropic behavior along the (100) and the (010) directions. Unlike systems like ruthenates, $Sr_2Ir_1O_4$ does not show correlations between conductivity and magnetism. When n increases, Z, the number of neighboring iridium ions in each compound, increases proportionally. As Z increases, the neighboring Ir ions along the c-axis have been described as having a stronger hybridization of their d-bands with the p-bands of the O ions. This hybridization splits the bands into bonding and antibonding states, which results in an increase of W. The presence of S.O.C. can

induce the formation of $J_{eff1/2}$ and $J_{eff3/2}$ bands (Figure 4.1). In addition, by Coulomb repulsion (U), the $J_{eff1/2}$ band splits into a Lower Hubbard Band (LHB) and an Upper Hubbard Band (UHB), opening a Mott gap. This makes the system insulator, as is the case for Sr_2IrO_4. When n increases, the bandwidth increases proportionally, allowing the LHB and UHB to overlap, destroying the Mott gap and triggering the IMT, as encountered in $SrIrO_3$. The last member of the RP series, Strontium iridiate ($SrIrO_3$, SIO) has a paramagnetic semi-metallic ground state, and has attracted recently much attention, principally due to the possibility of developing a new topological phase as has been proposed by some theoretical studies.

In $SrIrO_3$, the surprisingly narrow bands near the Fermi level (responsible for the semi-metallic state) are ultimately responsible for the control on the physical properties that can be exerted, not only by Spin-Orbit interaction and dimensionality, but by the interplay between them and the lattice distortions due to both in- and out-of-plane IrO_6 octahedral rotations [7].

In $SrIrO_3$, the surprisingly narrow bands near the Fermi lever (responsible for the semimetallic state) come from both in- and out-of-plane IrO_6 octahedral rotations [7], and the interplay between Spin-Orbit interaction and dimensionality is ultimately responsible for the control on the physical properties of the iridate.

Another factor to account for is the influence of the confinement when the dimensionality is reduced. It is well known that quantum confinement can be the
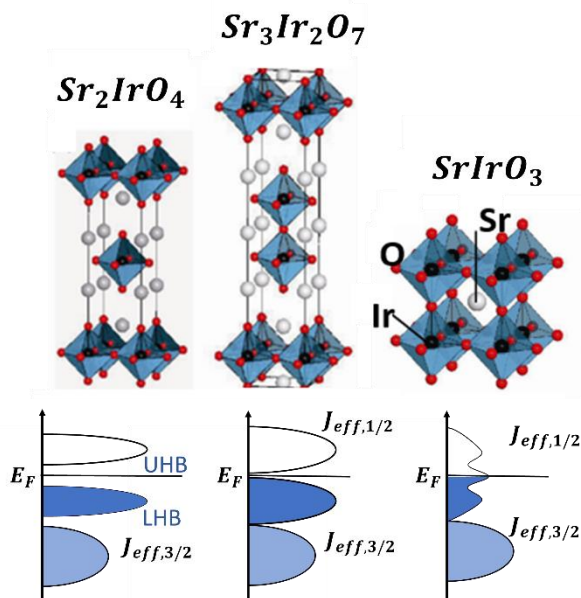

Figure 4.1: a) Structure of the 3 most representative members of the RP series, n=1, n=2 and n=∞. b) Schematic representation of the band structure of the three compounds near the Fermi level.

source of novel phenomena like high Tc superconductivity in cuprates (as seen in the chapter of cuprates) or enhanced magnetoresistance in manganites. The combination between confinement and SOC can host unexpected new effects. SIO thin films experience a Metal-Insulator transition for thicknesses under 2 nanometers. Theoretical calculations show that the Insulating state is also a correlated state due to an antiferromagnetic state developed in the transition. It is still not clear if the transition is driven by the interaction between electronic correlations and dimensionality or by the emergent magnetic state in the insulating phase [8,9]. Our objective is to clarify the origin of this transition in order to open the possibility of engineering a Spin Orbit Mott insulator.

1.1 Rashba Spin-Orbit Coupling

A 2-Dimensional electronic system (2DES) confined into an asymmetric quantum well will have a broken inversion symmetry This asymmetry will introduce in the system an electric field, which gives rise to a proportional Rashba Spin-orbit coupling [10,11].

SOC is the way to describe the coupling between an electron's spin and its orbital angular momentum about the nucleus. It is a relativistic correction to the Schrödinger equation, given by the following term in the Hamiltonian:

$$H_{so} = -\frac{\hbar}{4m_e^2 c^2} \vec{\sigma} \cdot \vec{p} \times \vec{\nabla} V \tag{35}$$

where σ are Pauli matrices (σ_x, σ_y, σ_z), $\vec{p}$ is the kinetic momentum and V is the electric potential of the atomic core. SOC can be understood as arising from the electric field produced by the nucleus which in the moving electron reference frame is perceived as a magnetic field which varies with the orbit of the electron. This results in a momentum dependent effective Zeeman energy. Two types of SOC exist, one generated by the bulk inversion asymmetry (BIA), known as Dresselhaus SOC, and Rashba coupling, which is due to the structure inversion asymmetry (SIA) in heterostructures [10,12,13]. For example, in a bidimensional system with an electric field applied in the z direction $\vec{E}=E_z \cdot \vec{z}$ this field breaks the symmetry between the +z and -z directions. resulting in Rashba SOC splitting as indicated in Figure 4.2 for a system with degenerate bands for spin up and down components.

In this example the Rashba term in the Hamiltonian will be:

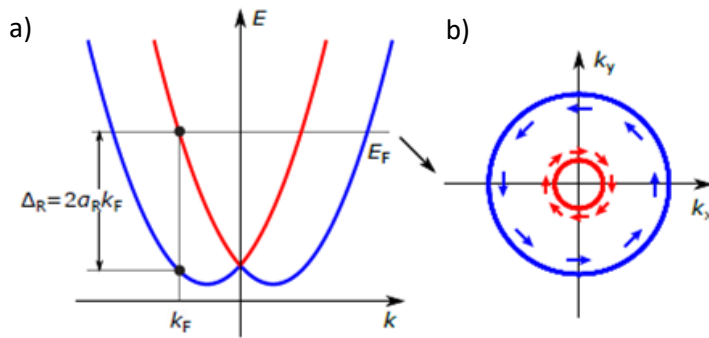$$H_R = \frac{\alpha_R}{\hbar} \vec{\sigma} \cdot \vec{p} \times \vec{z} \tag{36}$$

Figure 4.2: Degenerated bands for spin up and down due to the Rashba interaction. Adapted from [13].

where α_R is the Rashba parameter which reflects the strength of the SOC. Interestingly, this coupling constant is proportional to the electric field experienced by the system, so it can be modified by applying an external voltage. $\alpha = b\langle E \rangle$, where the coefficient b is proportional to the energy gap and the effective mass [14,15].

This type of SOC can be identified and studied from weak localization and antilocalization effects in the magnetoresistance measurements, discussed in the next section.

1.1.1 Weak Localization (WL) and Weak Anti-Localization (WAL)

In a weakly disordered system, the electrons motion will be preferentially diffusive. This can be distinguished studying the following two characteristic lengths [16]:

a) L_e: The mean free path: Measures the average distance that an electron can travel before its momentum changes by an elastic scattering in a static scattering center.

b) $L\varphi$: Phase coherent length: Measures the average distance that an electron can maintain its phase coherence. It is determined by inelastic scattering from electron-phonon and electron-electron interactions.

If:

$L_e \geq L\varphi$ The system is in a classic diffusive regime, so it can be described with a Drude model.

$L_e \ll L\varphi$ The system is in a quantum diffusive regime. Electrons maintain their phase coherence even after being scattered many times.
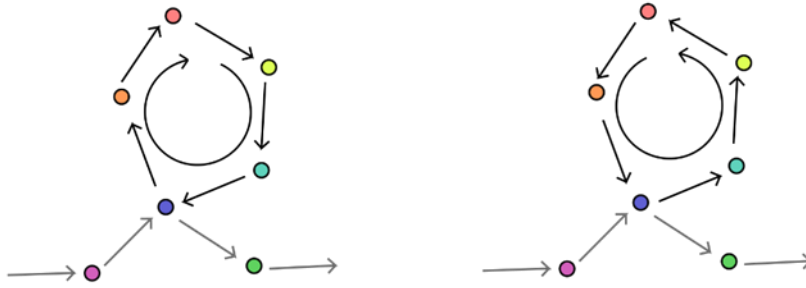
Figure 4.3: Schematic of the two possible time-reversed closed-loop trajectories of a pair of electrons. The quantum interference between them can be decisive if within the system the phase-coherence length is larger than the mean free path (Lφ> Le)

In the quantum diffusive regime, the constructive quantum interference between time-reversed pairs of electrons with closed-loop trajectories, will reduce the Drude conductivity. The effect of this quantum correction is called Weak Localization (WL) [16]. The two possible trajectories of a pair of interacting electrons are illustrated in Figure 4.3.

In presence of SOC, the spin of the electron is locked to its momentum. The two time-reversed paths gain an extra phase π. So, the destructive quantum interference between the two electron paths will increase the Drude conductivity. This effect is called Weak Anti-Localization (WAL). The temperature and magnetic field dependence of these effects is illustrated in Figure 4.4.

The behavior with the magnetic field can be understood as the magnetic field breaking the time-reversal symmetry, and thus destroying quantum interference.
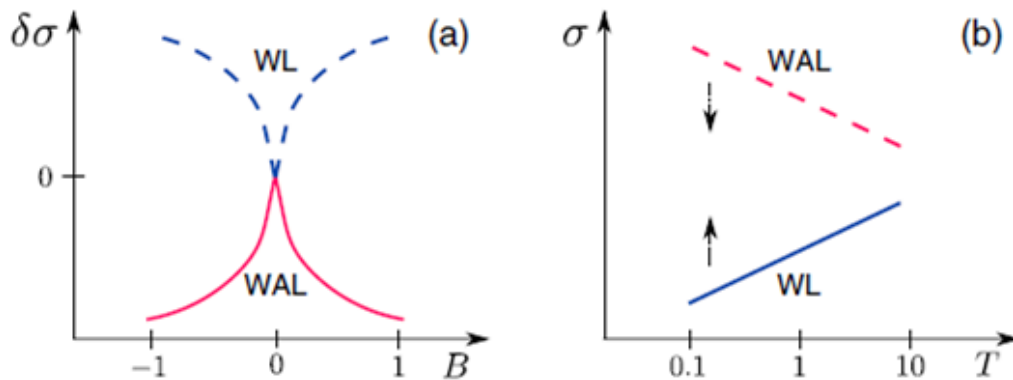

Figure 4.4: a) Effect of WAL and WL in the magnetoconductivity. b) Evolution of WL and WAL with temperature. Adapted from [16]

The correction to the conductivity is [16]:

$$\sigma^{qi} \propto \pm \frac{e^2}{\pi h} ln \frac{l_\varphi}{l_e} \qquad (37)$$

where + is for WAL and − for WL.

1.2 Dzyaloshinskii-Moriya interaction

The DMI causes spin canting around the D_{ij} vector according to $D_{ij}(S_i \times S_j)$, with $D_{ij} = r_{ij} \times \delta$, where r_{ij} is the direction that in SIO connects two Ir atoms and d is the bending of the Ir-O-Ir bond. (Figure 4.5). Although canting may yield non-zero magnetic moments locally, symmetry conditions may cancel the global magnetic moment. As seen in Figure 4.5, out of plane moments require the bending of out of plane Ir-O-Ir bonds. The out-of-plane (OOP) magnetization is, thus, associated to an OOP tilting of the oxygen octahedra, which is a rotation around the [110] axes. This tilting has not been found in previous works [17–19].
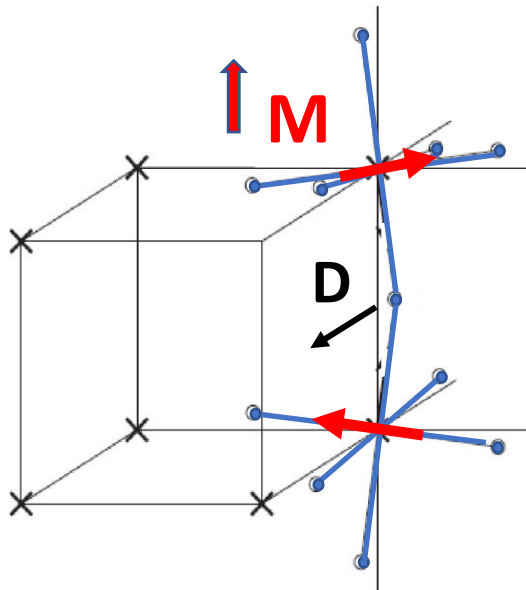

Figure 4.5: Sketch illustrating that the out of plane canted moment results from the out of plane bending of the Ir-O-Ir bonds in SIO.

1.3 Ionic Liquid gating

The objective of this work is to study the MIT of ultrathin SIO layers using the Ionic Liquid (IL) gating technique. Due to the high degree of carrier compensation, which makes the system a bad metal, the carrier density is low, and that offers the possibility to explore large portions of the phase diagram of the compound [20–26]. At the interface between a metal electrode and an ionic liquid, emerges a link between long-range structural correlations and the electrochemical response of a double layer capacitor. This phenomenon can be noticed as a variation of the capacitance as a function of the applied voltage. This response, studied by molecular simulations [27], results from a competition between entropic effects of packing and local constraints of electric neutrality within the ionic liquid near a planar, constant, potential electrode.

In the surroundings of an electrified interface, the distribution of ions and the thickness of the Electric Double Layer (EDL) depend on the electrode charge potential. In the case of an IL (which has a carrier density of 10^{15} cm^{-2}, one order of magnitude bigger than the generated by ferroelectric gating), all the ions which move to the interface in order to screen the charge density of the electrode, do not have room in the first layer, because of the size of the molecules. So, the ions that do not fit in the first layer will accommodate in the consecutive layers, as can be seen in the Figure 4.6.

At the IL-Metal interface, large electric fields are generated due to the EDL formation. These electric fields are screened over the Thomas Fermi screening length (which is a few nanometers in the case of SIO), which is almost the same
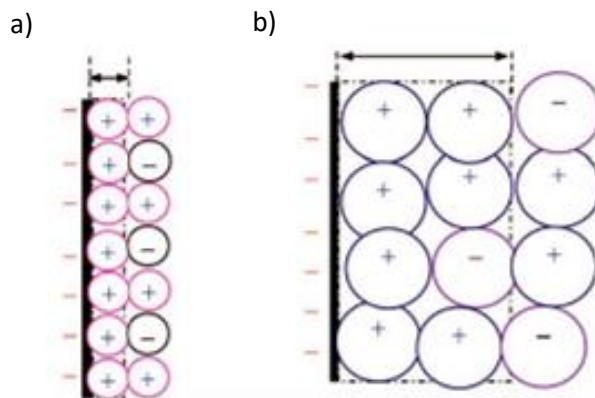

Figure 4.6: Schematic diagrams of an EDL generated in an IL with a) Small ions, and b) Large ions.

range as where the iridiate becomes insulating. For this reason, the IL gating is an ideal technique to investigate the origin of the MIT of ultrathin SIO layers. It is also important to consider the effects of the electric field at the interface, because it has a strong effect on the dimensionality of the system due to its selective effect on the confinement of bands with out of plane orbital polarization.

2. Sample growth, characterization and fabrication

2.1 Sample growth

SIO samples were grown using a High-pressure Sputtering system in the "Grupo de Física de Materiales Complejos (GFMC)" in "Universidad Complutense de Madrid (UCM)", with thicknesses oscillating from 1 to 3 nm (in order to study the system near the MIT) to 7nm (in order to study the structural properties). The growing conditions were a high pressure of pure oxygen (2.8mbar), and a substrate temperature of 650°C. Once the samples were deposited on the substrate and went passed through a one hour annealing at 650°C in a pure oxygen atmosphere (~920 mbar). This technique allows efficient thickness control due to its slow deposition rate (1nm/hour), and results in samples which are perfectly homogeneous and epitaxial (Figure 4.7).

| $La_{0.7}Sr_{0.3}MnO_3$ ■ | $SrIrO_3$ ■ | $SrTiO_3$ |
| Capping ■ | 7 u.c. ■ | (001) |
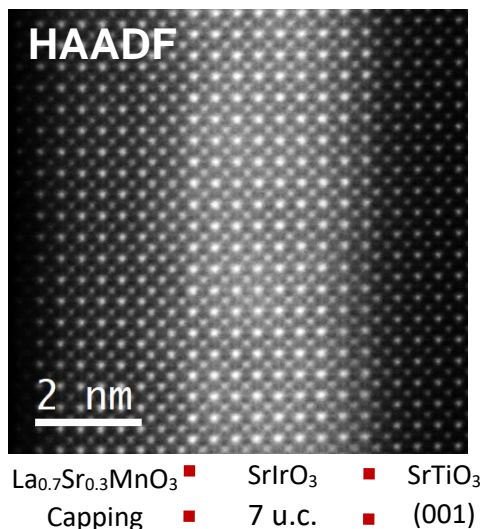
Figure 4.7: High angle annular dark field (HAADF) image of a 2.8nm SIO sample grown on a STO (100) substrate. A LSMO capping were grown on top of to sample in order to avoid degradation effects associated with the sample preparation.

2.2 Structural and electrical characterization

In order to determine the crystalline structure and the thickness of different SIO thin films, they were studied by X-Ray diffraction near (001) and (002) STO Bragg peaks
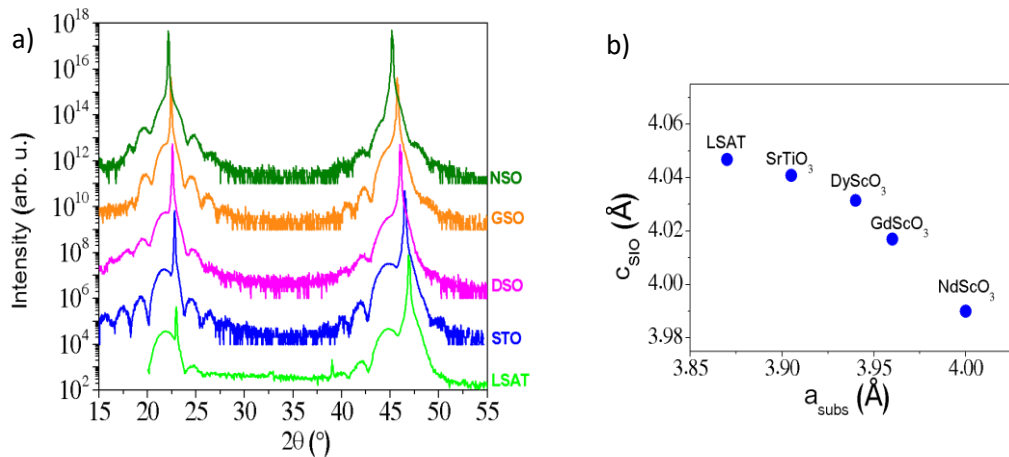
Figure 4.8: a) X-Ray diffraction measurements of 5nm SIO samples grown over different substrates. STO and LSAT induce compressive strain in the ab axis, and DSO, GSO and NSO induce expansive strain in the ab axis. b) c lattice parameter of the SIO as a function of the a lattice parameter of the different substrates.

(Figure 4.9). Satellite peaks can be observed near the STO peaks. This provides evidence of coherent epitaxial growth with sharp interfaces. We can obtain the c lattice parameter of the SIO layer from the position of the diffraction peak. As the thickness of the film decreases from 7.2 to 2nm, the observed lattice parameter c increases from 4.05 Å to 4.2 Å This behavior in the out of plane lattice parameter is expected given the existing mismatch between in plane SIO and STO lattice
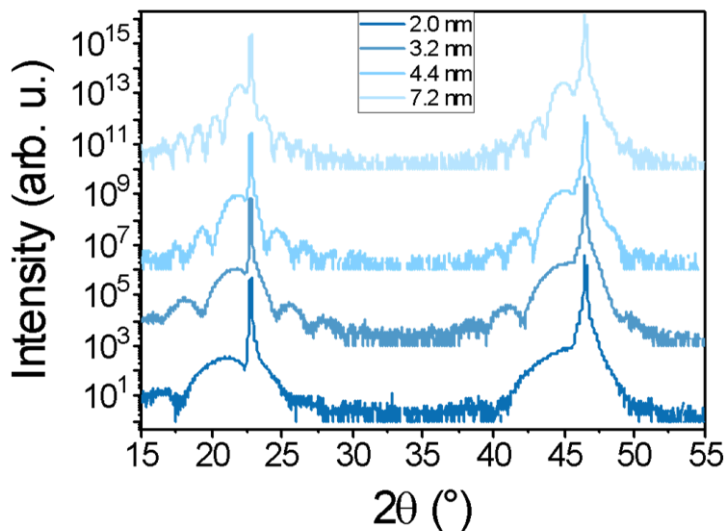

Figure 4.9: X-Ray diffraction measurements of samples with different thicknesses of SIO grown over STO (100) substrates.

parameters (bulk SIO: a = 3.94 Å; bulk STO: a = 3.905 Å). Thus, compressive tension in the ab axis will generate expansive tension in the c axis.

SIO samples were grown over different substrates to explore the effect of the strain in the MIT (Figure 4.8). The substrates chosen were two compressive in plane ($SrTiO_3$ and ($La_{0.18}Sr_{0.82}$) ($Al_{0.59}Ta_{0.41}$)O_3 (or LSAT)) and three expansive in plane ($NdScO_3$, $DyScO_3$ and $GdScO_3$).

For the electrical characterization, the samples were measured in Van der Pauw configuration [28] to study their behavior with temperature. Figure 4.10a shows the resistivity evolution with decreasing temperature for different thicknesses of SIO grown on STO. It can be perceived the MIT occurs when the thickness is reduced to 4-5 unit cells, proving that this process is directly related to the dimensionality of the system. The same study was done for different substrates (Figure 4.10b), and it
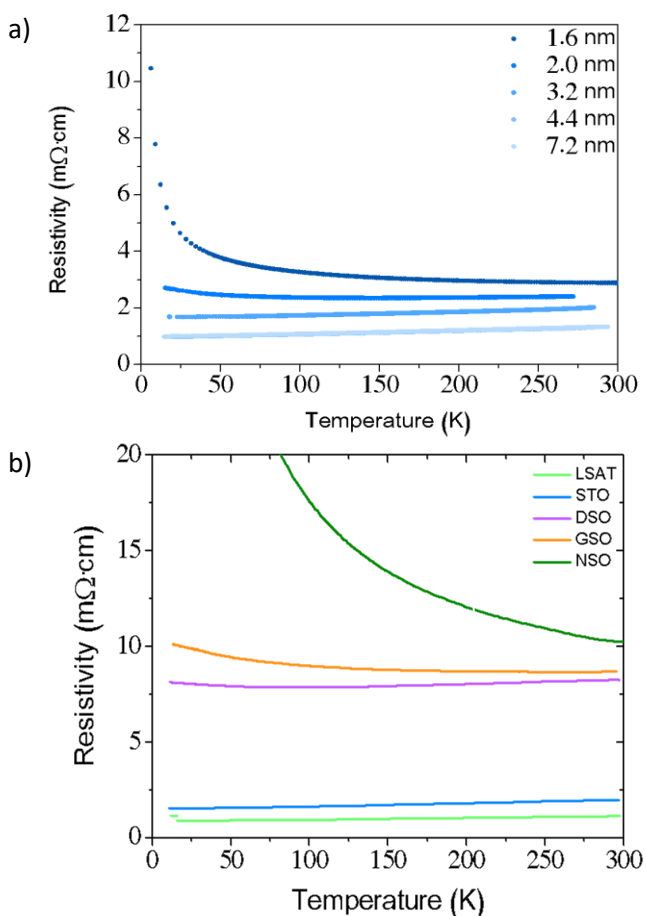

Figure 4.10: a) R vs. T measurements of SIO samples grown on STO (001) with different thicknesses. A MIT happens when the dimensionality is reduced to 4-5 unit cells of iridiate. b) R vs. T of 4nm SIO over different substrates.

was observed that the samples that were grown under a compressive strain (i.e. over STO and LSAT) have a metallic behavior, while the samples grown under an expansive strain have larger resistivities at room temperature and an insulating behavior when the strain is large enough (i.e. over GSO and NSO).

So, we have achieved a MIT in two ways, firstly with dimensionality reduction by decreasing the SIO thickness, and secondly by strain using a variety of substrates with different lattice parameters. This leaves us in an excellent position to explore the objective and achieve the MIT modifying the carrier density with a gating experiment in a suitably fabricated device.

2.3 Device fabrication

The device configuration is a Hall Bar design with a side gating geometry (Figure 4.11a) in order to measure Hall Effect. The definition of the device on the sample was performed with optical lithography (see chapter 2) using a mechanical mask (Figure 4.11b), combined with reactive Ion etching. The lithography was done in two steps. The first step defines both the Hall bar and the metallic contacts. The second one (Figure 4.11b) is used to evaporate gold over the contacts and the millimetric gates.

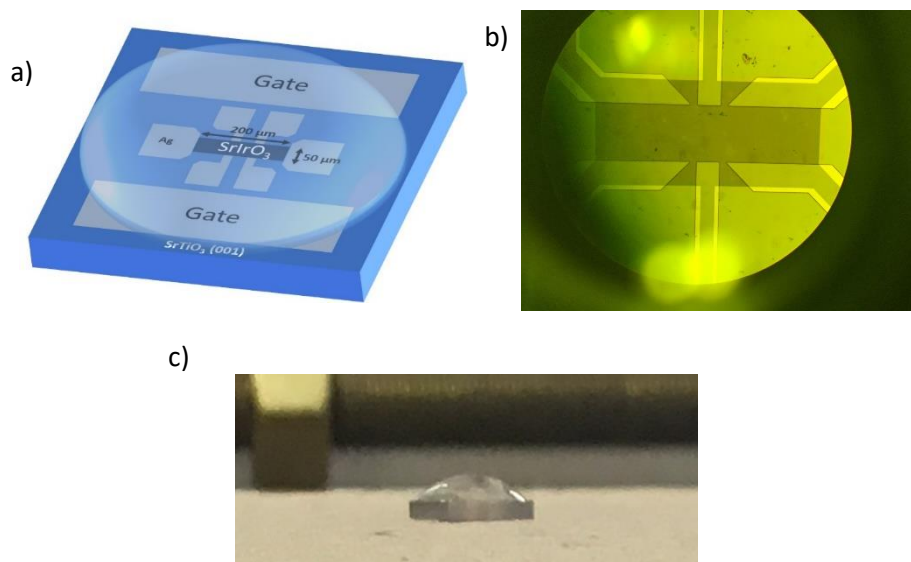*Figure 4.11: a) Representation of the final device in side gating geometry with the SIO Hall Bar and the drop of ionic liquid the sample and the gold gates. b) Image of a real sample from the optical lithography. The dimensions of the Hall Bar sample are 250µm width and 160µm length. The contacts were sputtered with gold, which is non-reactive with the ionic liquid. c) Image of the sample with the ionic liquid drop on top.*

The last step is to deposit a 1µl drop of ionic liquid (Figure 4.11c) that covers all the sample. This ionic liquid is a DEME-TFSI [21] which is reactive for temperatures over 230K, so it was deposited with the sample on a previously cooled cold plate. The DEME-TFSI was baked at 100°C and at 10^{-2} Torr for the previous 24 hours.

3. Transport measurements

The transport characterization was performed using a PPMS system at "Instituto de Ciencia de Materiales de Madrid (ICMM-CSIC)". The study is based on two samples, grown with 1.6 and 2 nm thicknesses, which are at the neigbourhood but on different regimes of a Metal to Insulator transition: one in the metallic (2nm) regime and the other (1.6nm) in the insulating range. The samples were polarized with ionic liquid gating, in order to traverse the MIT from both regimes. Figure 4.12a shows the two configurations that measure resistance in four/point configuration (V_{xx}) or Hall effect configuration (V_{xy}).The way of changing the electric and magnetic state of the samples is by applying different gate voltages to the ionic liquid using the configuration shown in Figure 4.12b. Therefore, proven that positive voltages dope the samples with electrons, meanwhile negative voltages dope them with holes. The ions of the IL cannot move below 230K, so the process for sample polarization consists of rising the temperature to 230K, applying the gate voltage for 5 minutes, wait for the stabilization of the double layer and then decreasing temperature, freezing the ions and fixing the carrier doping of the SIO.

We measured resistance versus temperature in the 1.6 and the 2 nm samples for different gate voltages (Figure 4.13). For the 2nm sample, the gate voltage applied was positive, doping the system with electrons, and so the sample became insulating. On the other hand, negative voltages applied to the 1.6nm sample turned
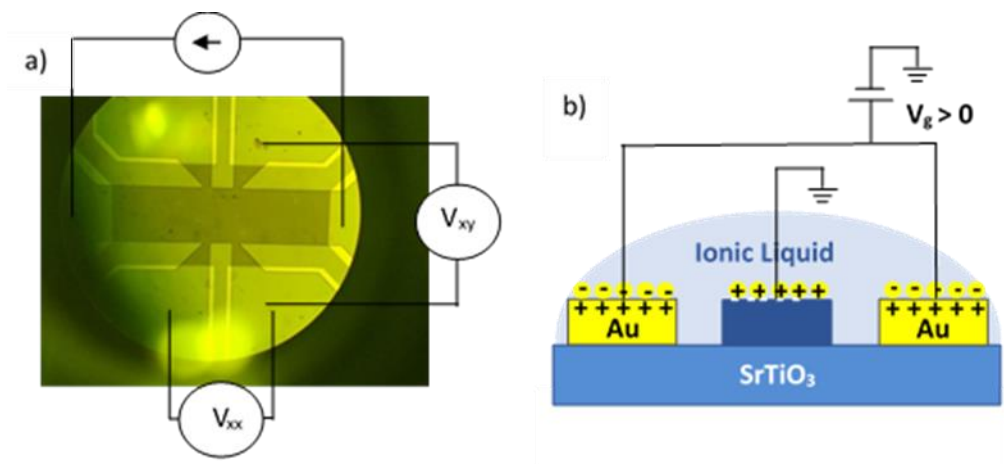

Figure 4.12: a) Scheme of the Hall Bar configuration for measuring Rxx and Rxy. b) Scheme of the polarization configuration for a positive voltage applied.
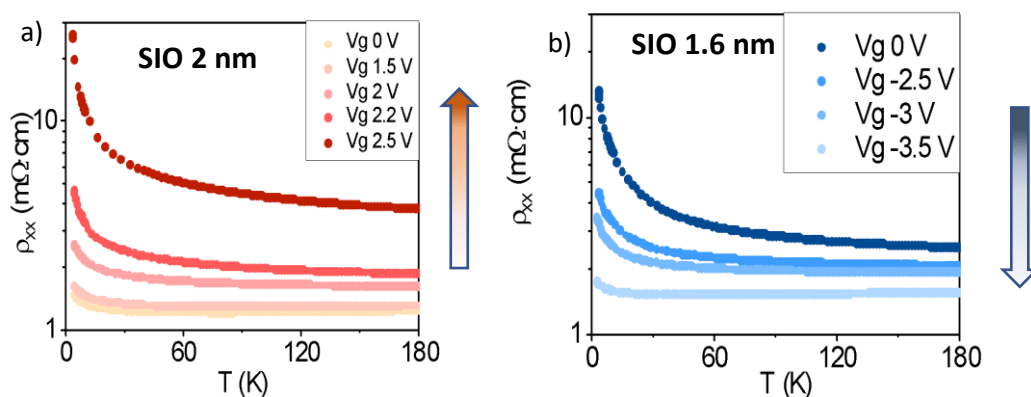
Figure 4.13: IL gating experiments of a 2 nm SIO 113 sample at the metallic side of the MIT (left panel) and of a 1.6 nm sample at the insulating side (right panel)). Longitudinal resistivity measured at each gate voltage. The samples were grown near the MIT edge in order to cross the transition from both sides. The metallic 2nm sample were doped with electrons, using positive voltages, and the 1.6nm sample was doped with negative voltages (hole doping).

it metallic. This result suggests that the holes are the responsible carriers for the conduction.

The gate voltages are not the same for the *Metal to Insulator* transition as in the reverse order (*Insulator to Metal*). For positive voltages, the SIO becomes insulator when a gate voltage of 2.5V is applied, but it is necessary to apply -3.5V to reverse the insulating state in the other sample. One possible explanation to this is that the necessary voltage depends on how far the sample is from the transition. Another possibility is that the confinement effect of the ultrathin samples is modulated by the electric field generated during the gating process. The applied voltages are in the limit of what the ionic liquid can reach without degradation. To ensure that, we performed a study of degradation of the ionic liquid (Appendix 1) for the voltages used in the experiment.

In the same configuration as the R vs. T measurements inside the PPMS, magnetoresistance (MR) measurements were performed on both samples at each gate voltage (Figure 4.14). The magnetic field was applied in normal incidence from -14T to +14T. We can observe that both samples show the same behavior when in metallic or insulating state. In the upper panels, the magnetoresistance turns from negative at 4K to positive at 40K.

The lower panels show the magnetoresistance measurements for both samples in the metallic state. In this case the 1.6nm sample was measured after applying a gate voltage of -3.5V. The MR is positive in all the temperature range.
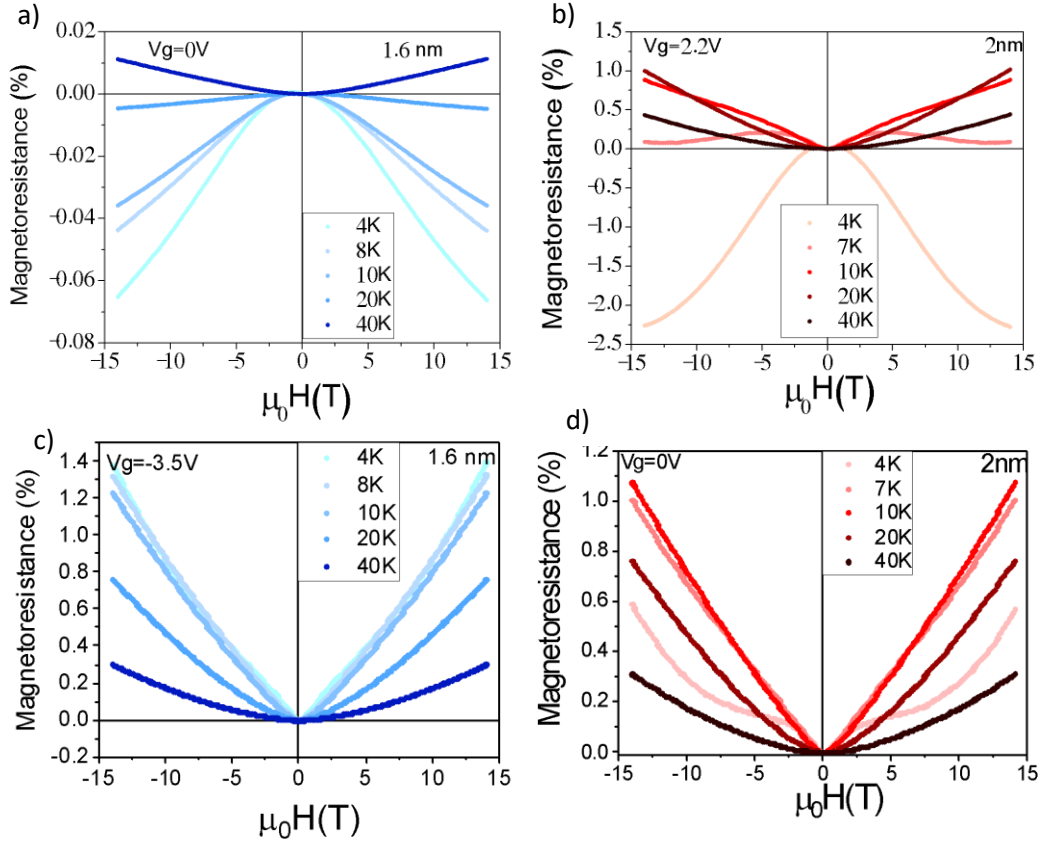
Figure 4.14: Magnetoresistance measurements in both samples at the insulating (upper panels) and metallic (lower panels) states.

The behavior of the magnetoresistance curves is directly related with the modification of the scattering lengths for different processes due to the electric field-modulated confinement. To analyze this relation, a Hikami-Larkin-Nagaoka fitting was performed in the MR curves of the two samples.

3.1 Hikami-Larkin-Nagaoka analysis

For the measurements of Figure 4.15 a Hikami-Larkin-Nagaoka [29,30] fitting was performed to obtain the free length scales for different interactions:

$$l_H = \sqrt{\frac{hc}{2eH}} : \text{Flux quantum length}$$

$$l_{so} = \sqrt{D\tau_{so}} : \text{Spin-Orbit diffusion length}$$

$$l_i = \sqrt{D\tau_i} : \text{Inelastic length}$$

108

The magnetoresistance regime depends on the relative size of these characteristic lengths. The Hikami-Larkin-Nagaoka formula of the magnetoconductance in a bidimensional system into a perpendicular magnetic field, assuming negligible Zeeman splitting [8,29,31], is:

$$\frac{\Delta\sigma(B)}{\sigma_0} = -\Psi\left(\frac{1}{2} + \frac{B_e}{B}\right) + \frac{3}{2}\Psi\left(\frac{1}{2} + \frac{B_\varphi + B_{so}}{B}\right) - \frac{1}{2}\Psi\left(\frac{1}{2} + \frac{B_\varphi}{B}\right)$$
$$-ln\left(\frac{B_\varphi + B_{so}}{B_e}\right) - \frac{1}{2}ln\left(\frac{B_\varphi + B_{so}}{B_\varphi}\right) \tag{38}$$

where $\Psi(x)$ is the Digamma function, which is the logarithmic derivative of the gamma function:

$$\Psi(x) = \frac{d}{dx}ln\left(\Gamma(x)\right) \tag{39}$$

with $\Gamma(n) = (n-1)!$ For any positive integer, n. If not, any real number the gamma function is defined via a convergent improper integral:

$$\Psi(z) = \int_0^\infty x^{z-1}e^{-x}dx \tag{40}$$

and $B_i = \frac{\hbar}{4el_i^2}$

For the elastic characteristic field, we assume the value of Be= 1.2T, a value that corresponds to an elastic length of 11.7 nm and a carrier density in the order of 10^{19} cm^{-3} as in [8]. The resistivity values are similar in both samples and for the different polarization voltages, so the use of the same B_e for all the curves is acceptable. The magnetic field dependence of the conductance underscores a coupling between spin dynamics and transport. Presented in Figure 4.15 is the magnetoconductance [σ(H)-σ(H=0)]/σ(H=0), with σ being the sheet conductance in $e^2/\pi h$ units, and H the magnetic field, applied perpendicular to the SIO-IL interface.

The magnetoconductance is calculated as follows:

$$\sigma_{xx} = \frac{\rho_{xx}}{\rho_{xx}^2 - \rho_{xy}^2} \tag{41}$$

and:

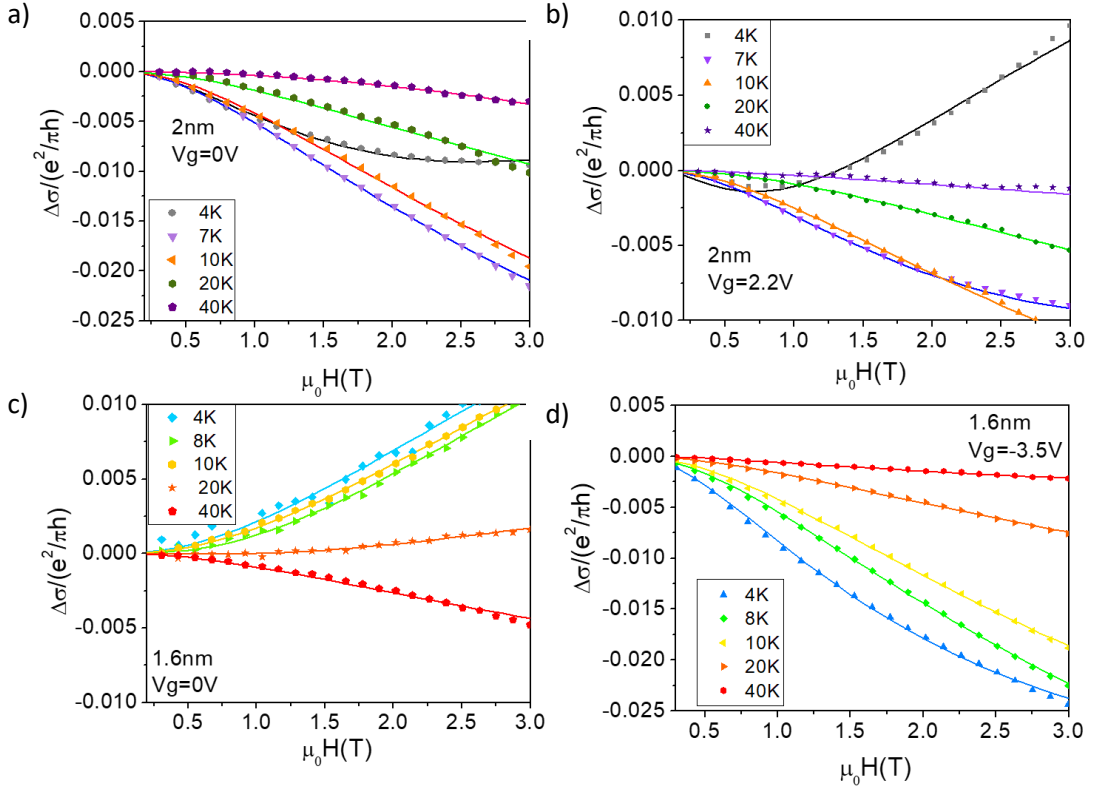$$\rho_i = R_i * \frac{S}{l} \tag{42}$$

Figure 4.15: Hikami-Larkin-Nagaoka fittings to the magnetoconductance in $e^2/\pi h$ at different temperatures. The upper panels show the MC of the 2nm sample with 0V (left) and 2.2V (right) applied. The lower panels show the MC of the 1.6nm sample with 0V (left) and -3.5V (right).

where "i" can be "xx" or "xy", S is the cross-section area and "l" is the length of the Hall bar. ρ_{xx} (ρ_{xy}) is referred to the measurement of the resistance in the V_{xx} (V_{xy}) configuration (Figure 4.12). The fitted MR curves are presented in Figure 4.15.

According to the analysis of the Hikami-Larkin-Nagaoka equation, the scattering lengths and the corresponding effective fields $B_i = \hbar/4el_i^2$ for both inelastic and spin-orbit scattering can be extracted and their influence on the MIT studied (Figure 4.16). It can be observed that l_{SO} decreases in the metallic state and increases when the sample becomes insulating. On the contrary, the inelastic interaction seems to remain constant during the MIT of the system. A decrease of l_{SO} implies an increase of the SOC in the metallic state. As previously stated, the Spin Orbit Coupling is responsible for the Weak Anti-Localization effect, which is in good agreement with the raise in the MR in both samples in the metallic state (Figure 4.14 lower panels).

In Figure 4.16 we can also observe that the values of l_{SO} are similar for the two samples in the metallic state (M) and in the insulating state (I), proving that we can
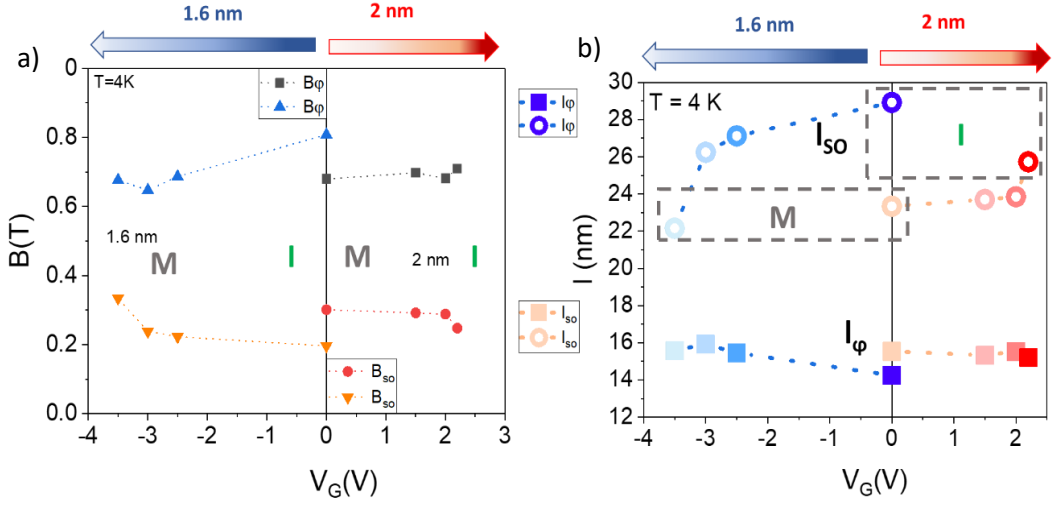
Figure 4.16: Values extracted from the Hikami-Larkin-Nagaoka fittings to the magnetoconductance curves as a function of the applied gate voltages. Here can be observed the evolution of the Spin orbit diffusion effective field and the Inelastic effective Field in the left panel, and the evolution of the SO diffusion length and the Inelastic length in the right panel.

traverse the MIT from both states, the metallic and the insulating, and that the strength of the SOC can be decisive in this transition.

3.2 Hall measurements

Hall effect measurements were conducted simultaneously with the longitudinal resistivity and the magnetoresistance. The measurement configuration is specified in Figure 4.12a, and the Hall curves are presented in Figure 4.17. These curves can be used to examine possible changes in the carrier density as a result of the gating process. We selected 40K because at this temperature the effects of quantum corrections to the conductivity or possible low temperature magnetic phases are not present, as discussed below. The negative slope for all the applied voltages indicates that the mobility is larger for electrons than for holes, as seen in previous reports [32,33]. The minor changes in the Hall slope shows that the carrier density is slightly varying, due to the carrier compensation. It is necessary to use a two-band model to extract the carrier density and the mobilities from the Hall measurements [32]:

$$\rho_H = \frac{tR_{xy}}{B} = \frac{1}{e} \frac{n_h\mu_h^2 - n_e\mu_e^2 + (n_h - n_e)(\mu_h\mu_e B)^2}{\frac{\sigma_0^2}{e^2} + (n_h - n_e)^2(\mu_h\mu_e B)^2} \tag{43}$$
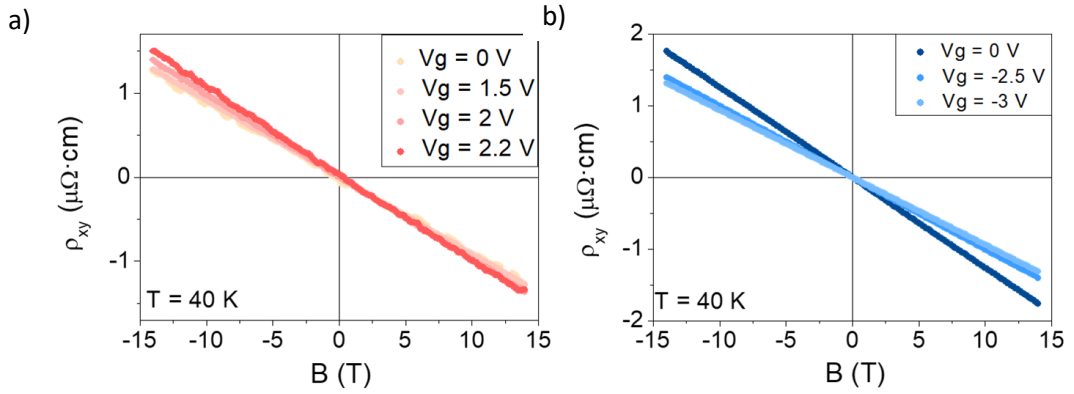
a)

b)

Figure 4.17: Hall effect measured for the 2nm (left) and the 1.6nm sample (right) at 40K and at each gate voltage.

where t is the film thickness, R_{XY} is the Hall resistance, e is the electron's charge, B is the magnetic field, n is the carrier density, μ is the carrier mobility, and:

$$\sigma_0 = \sigma_h + \sigma_e = e(n_h \mu_h + n_e \mu_e) \tag{44}$$

Since the Hall measurements of Figure 4.17 are linear and negative for the whole magnetic field range, the Hall resistivity expression can be approximated with its low-field limit:

$$\rho_H = \frac{e}{\sigma_0^2}(n_h \mu_h^2 - n_e \mu_e^2) \tag{45}$$

In two-band systems showing inflection points in the magnetic field dependence of ρ_H, carrier parameters can be extracted from the combined measurements of σ_0 and ρ_H. In our case, ρ_H shows a linear regime in all the measured magnetic field range and the estimation of carrier parameters cannot be done.

Magnetoresistance measurements can provide the rest of the magnetotransport information, necessary to estimate the carrier concentrations and mobilities in our samples. From the magnetoresistance we extract the cyclotron component:

$$MR = \frac{e}{\sigma_0}(n_h \mu_h \mu_e^2 + n_e \mu_e \mu_h^2)B^2 \tag{46}$$

where MR is the slope of for magnetoresistance curves plotted versus B^2. With these equations and assuming that the ratio between the electron and hole mobilities remains constant and equal to:

$$\mu_e = \alpha_0 \mu_h \tag{47}$$

we obtain the values of carrier density and mobilities as a function of the applied gate voltage (Figure 4.18). We can observe that, for $\alpha_0 = 1.3$, the electrons and holes carrier densities are almost equal for the two samples when they are in the same conducting state (metallic or insulating), meanwhile the mobilities hardly vary from one state to another. The values obtained are in good agreement with the obtained by Manca et al. [32] in the same system. All the values of mobility and carrier density as a function of the applied voltage are presented in the Table 4.1 and Table 4.2:

Table 4.1: Input parameters and carrier densities & mobilities extracted from the equations for the 1.6nm sample.

1.6 nm	σ_0 (10^4 S/m)	ρ_H (10^{-9} $\Omega\cdot$m)	MR (10^{-5} T^{-2})	n_e (10^{25} m^{-3})	n_h (10^{25} m^{-3})	μ_e (cm²/V·s)	μ_h (cm²/V·s)
0V	4.82	-1.26	3.88	1.90	3.20	68.8	52.9
-2.5V	7.23	-1.00	2.72	3.47	5.70	57.6	44.3
-3V	8.28	-0.94	2.15	4.45	7.32	51.2	39.4

Table 4.2: Input parameters and carrier densities & mobilities extracted from the equations for the 2nm sample.

2 nm	σ_0 (10^4 S/m)	ρ_H (10^{-9} $\Omega\cdot$m)	MR (10^{-5} T^{-2})	n_e (10^{25} m^{-3})	n_h (10^{25} m^{-3})	μ_e (cm²/V·s)	μ_h (cm²/V·s)
0V	8.97	-0.88	1.34	6.17	9.96	40.52	31.17
1.5V	8.33	-0.91	1.39	5.62	9.11	41.23	31.72
2V	6.18	-1.00	1.54	3.94	6.45	43.34	33.35
2.2V	4.84	-1.16	1.93	2.75	4.53	48.50	37.31

We can observe that the mobility variation is too small to have any influence in the MIT, and that the increase of the carrier density is large, but not enough to change the slope of the Hall resistivity, probably due to carrier compensation. Observing the semi-metallic band structure of the SIO, the MIT cannot be explained as an increase of the number of carriers increases the conductivity. This points to an effect of the electric field being the origin of the gating induced MIT rather than of the carrier density variation.

The evolution of the conducting states of both samples with gating suggests that the electric field pointing down on the 2nm sample generates the same conducting states as a comparable electric field pointing up does on the 1.6nm sample. In particular, the insulating state is reached in the 2nm sample under an electric field
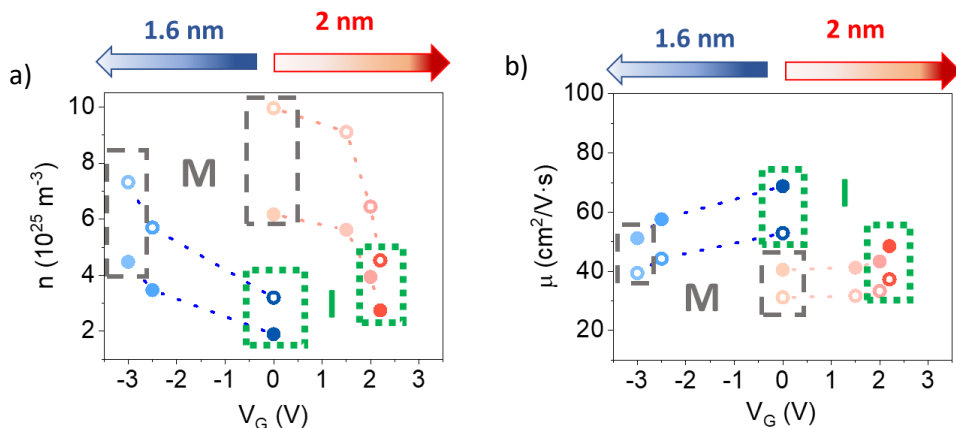
Figure 4.18: (Left) Carrier density modification with the applied voltage. The values are very similar for the two samples when they are in the metallic state (dashed grey lines) and when are in the insulating state (dotted green lines). (Right) Carrier mobility modification with the voltage for the two samples. The Hollow circles represent the holes and the filled circles, the electrons.

pointing down of $6 \cdot 10^{21}$ N/C, corresponding to a gate voltage of 2.2V. On the other hand, the 1.6nm sample reaches the metallic state with an electric field pointing up of $7.7 \cdot 10^{21}$ N/C, corresponding to a gate voltage of -3V. This indicates that the confinement effect of the ultrathin samples can be modulated by the electric field generated during the gating process.

In order to rationalize these observations and to correlate them with electronic structure features, it should be noted that t_{2g} orbitals of the SIO ultrathin layers will be highly confined by the large 3.2 eV gap of the STO and the surface potential. The effect of this confinement will be different for each orbital d_{XY}, d_{XZ} and d_{YZ}, due to their different symmetry. d_{XY} bands will remain bulk like due to their 2D character, meanwhile the d_{XZ} and d_{YZ} bands will form confined states. These orbital-selective confinements are known as responsible for the origin of MIT in $SrVO_3$ layers [34–36]. A reduction of the thickness will increase the confinement, pushing these confined states above the Fermi level as expected from the phase shift quantization rule of confined metals [37,38].

The electric field can change the effective width of the confinement potential, but the change in the spacing or the filling of the confined levels should be symmetric in the two vertical directions. So, the difference between the positive and the negative fields is due to a pre-existing electric field related to the symmetry breaking at the SIO-IL interface.

First principles DFT calculations were conducted by J. I. Beltran from UCM, and M.C. Muñoz from ICMM, proving this behavior, as is shown in Figure 4.19. Levels are pushed above the Fermi level for electric fields pointing down (yielding an insulating
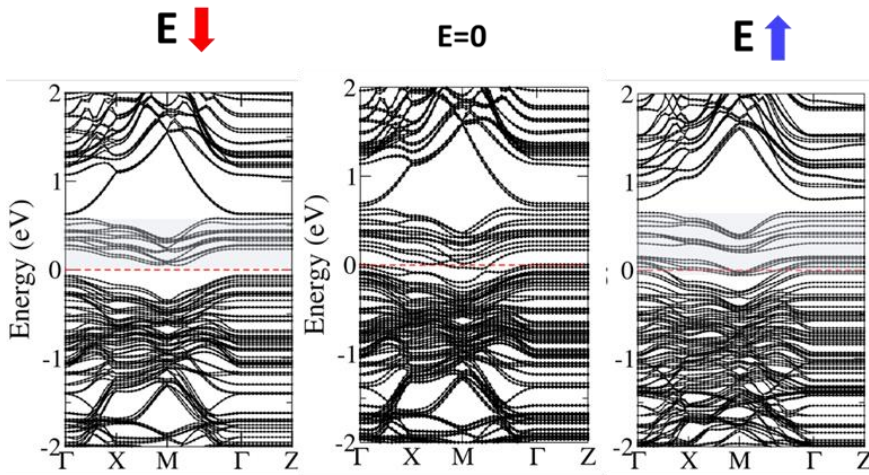
Figure 4.19: First principles Density Functional Theory (DFT) calculations for a 3 monolayers SIO sample on STO (001). We can study the modification of the bands diagram when the applied electric field is down (left panel), zero (center panel) or up (right panel).

state), and levels cross the Fermi level for electric fields pointing up (metallic state). This proves that our MIT is due to strong orbital confinement.

The electric field modulation of confinement is evidence of the possibility of control symmetry breaking. An indication of these broken symmetry states is a magnetic state found in the insulating phase from the low temperature Hall measurements (Figure 4.20). Anomalous Hall effect appears in magnetic systems with spin orbit
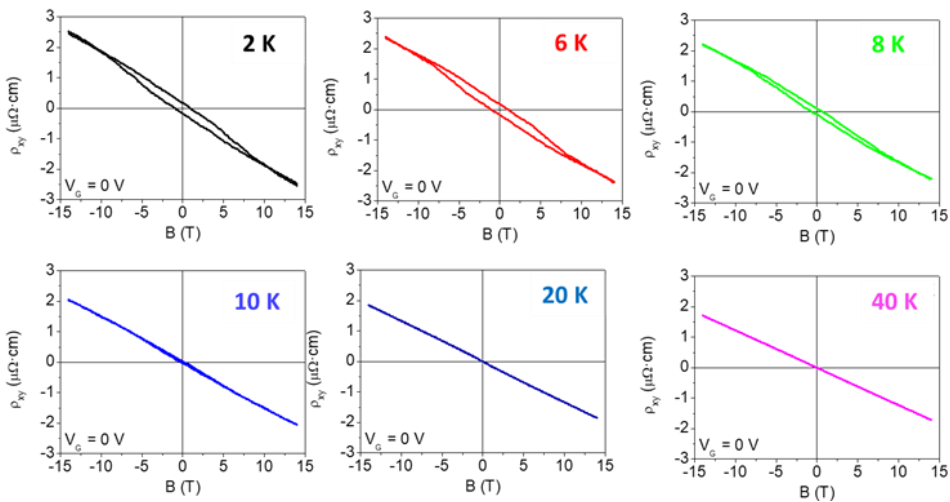

Figure 4.20: Hysteretic Anomalous Hall effect obtained measuring the low temperature transverse resistivity as a function of magnetic field.

interaction and is known to scale with magnetization. The effect is present only at low temperatures (below 10K).

We have subtracted the normal Hall resistivity obtained by the high fields slope (Figure 4.21) and the difference is an inverted hysteresis loop, indicating that the anomalous Hall effect is negative. The coercive field measured is around 5T. It has a remanence when the applied field is out of plane, indicating an out of plane magnetic component in the sample.

This magnetic state is different from other magnetic states found previously in perovskite iridates, such as the metamagnetic state found in Sr_2IrO_4, or the ferromagnetic state found in (SIO/STO) superlattices, both with in-plane magnetic moments. The magnetic state is present only in the insulating phase, and so it can be controlled by an electric field, as seen in (Figure 4.21b). The large coercive and saturation fields indicate that the origin of the magnetic state can be the canting of an antiferromagnetic state by the Dzyaloshinskii-Moriya interaction (DMI), which is
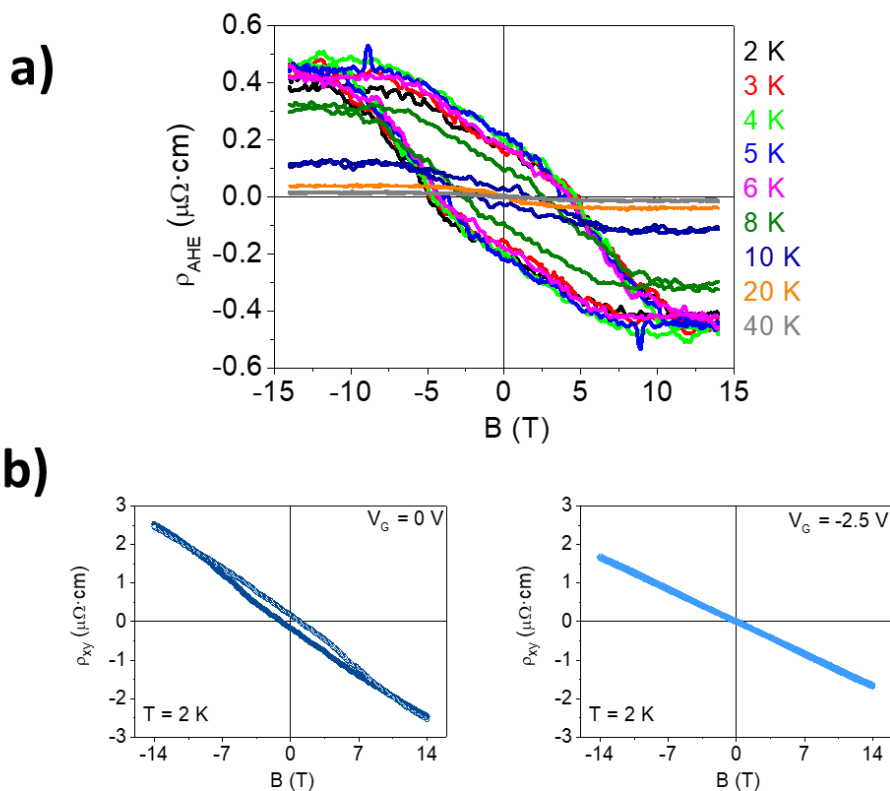

Figure 4.21: a) Contribution of the Anomalous Hall effect resistivity to the transverse resistivity obtained by subtracting the normal (linear) Hall resistivity. b) Electric field control of the emergent magnetism. Gating experiments at 2K at negative voltages show the suppression of the Anomalous Hall effect.

a chiral interaction between spins in systems with broken inversion symmetry [See Dzyaloshinskii-Moriya section].

3.3 Reciprocal space maps

Finally, in order to explore the effect of oxygen rotations on the symmetry reduction of the unit cell, three-dimensional reciprocal space maps were conducted. Reciprocal space maps were measured in a Bruker D8 Discover Micro diffractometer equipped with a two-dimensional Vantec detector, Hubber ¼ Eulerian cradle, video camera / laser alignment system, and a Co Kα X-ray radiation point source (λ= 1.79 Å), situated in the Characterization Facility of the University of Minnesota. The beam is conditioned with a graphite monochromator and the samples were mounted in reflection configuration. The diffractometer images were acquired using 2D detectors, and recorded, analyzed and combined to reconstruct the structure factor in 3D reciprocal space using a self-designed software tool, named RS*Lab. In Figure 4.22 reciprocal space maps are shown with (H,K,L) triads referred to the pseudo cubic unit cell. Non-integer reflections, in plane and out of plane, can be identified. The pattern of non-integer reflections indicates a reconstruction ($\sqrt{2} \times \sqrt{2} \times 2$) of the unit cell. This reconstruction is compatible with a "Pbmn" structure, which involves 3-D rotations of the oxygen octahedra. The Pbmn symmetry group, according to Bertaut Rules [39] is consistent with the out of plane weak ferromagnetism [40]. Precisely, the plane tilting of the oxygen octahedra (as said, rotation around in plane [110] directions) is responsible for the OOP magnetic moment, as sketched in Figure 4.5.
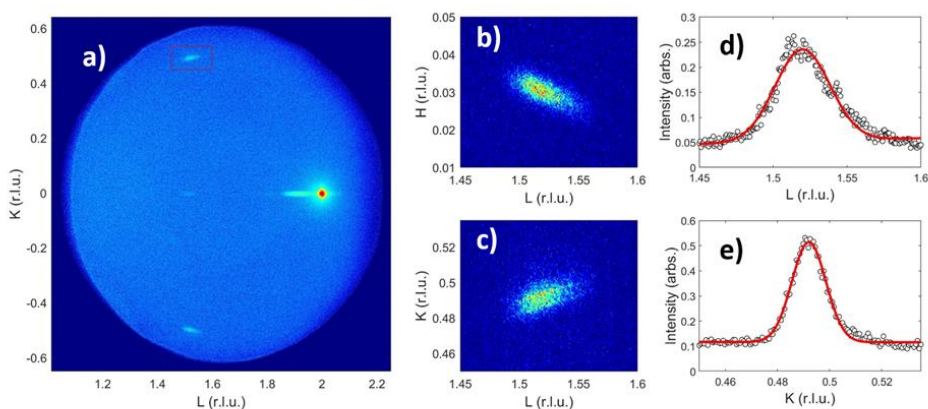

*Figure 4.22: a) Reciprocal space map of a **2nm** thick SrIrO₃ sample deposited on (100) STO, showing half integer reflections named with H, K and L indexes, refereed to the pseudocubic cell. L (b,d)and H (c,e) intensity profiles of the (-0.5, 0, 1.5) reflection.*

3.4 Gating Reversibility

In order to study whether the gating process is reversible or not, a metallic SIO sample was grown and fabricated into the device structure explained in section XX an Ionic Liquid drop was deposited on top of the device. The sample was firstly doped with a positive 2.5V voltage in order to make it insulator (Figure 4.23). After that, a -3V voltage was applied, making the sample metallic, even with lower resistivity than at 0V. This probes the reversibility of the gating process.
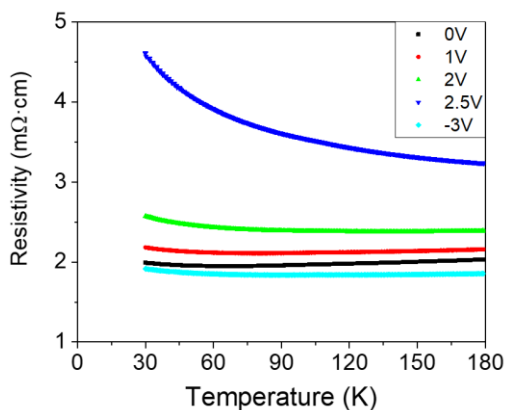

Figure 4.23: R vs. T measurements for different gate voltages from 0V (black) up to 2.5V (Blue) and after that, at -3V (Light blue).

4. Conclusions

We have found an MIT in $SrIrO_3$ thin films, with a weak ferromagnetic state when the system is insulator. We can cross the transition from both sides and in a reversible way by using an IL gating technique. The emergent ferromagnetic state originated from a canted antiferromagnetism associated to the insulating phase, gives solid evidence that electronic correlations are playing a role in the MIT activation. The electric field-controlled confinement allows us to modulate the bandwidth, raising the importance of the electronic correlations, and this yields the MIT. Besides, ferromagnetic insulators can be very useful in spintronic technologies, as spin filters or as electrodes in proximity interactions. When the transition is crossed, we have a non-magnetic metal with strong spin-orbit interaction. These systems are desirable, for example, as spin-charge converters. The possibility of switching between both states with an electric field could inspire novel developments in the oxide electronics field.

5. References

[1]   S. J. Moon, H. Jin, K. W. Kim, W. S. Choi, Y. S. Lee, J. Yu, G. Cao, A. Sumi, H. Funakubo, C. Bernhard, and T. W. Noh, Phys. Rev. Lett. **101**, 2 (2008).

[2]   A. Yamasaki, H. Fujiwara, S. Tachibana, D. Iwasaki, Y. Higashino, C. Yoshimi, K. Nakagawa, Y. Nakatani, K. Yamagami, H. Aratani, O. Kirilmaz, M. Sing, R. Claessen, H. Watanabe, T. Shirakawa, S. Yunoki, A. Naitoh, K. Takase, J. Matsuno, H. Takagi, A. Sekiyama, and Y. Saitoh, Phys. Rev. B **94**, 1 (2016).

[3]   H. Zhang, K. Haule, and D. Vanderbilt, Phys. Rev. Lett. **111**, 1 (2013).

[4]   G. Cao, J. Bolivar, S. McCall, J. Crow, and R. Guertin, Phys. Rev. B - Condens. Matter Mater. Phys. **57**, R11039 (1998).

[5]   B. J. Kim, H. Ohsumi, T. Komesu, S. Sakai, T. Morita, H. Takagi, and T. Arima, Science (80-.). **323**, 1329 (2009).

[6]   B. J. Kim, H. Jin, S. J. Moon, J. Y. Kim, B. G. Park, C. S. Leem, J. Yu, T. W. Noh, C. Kim, S. J. Oh, J. H. Park, V. Durairaj, G. Cao, and E. Rotenberg, Phys. Rev. Lett. **101**, 1 (2008).

[7]   Y. F. Nie, P. D. C. King, C. H. Kim, M. Uchida, H. I. Wei, B. D. Faeth, J. P. Ruf, J. P. C. Ruff, L. Xie, X. Pan, C. J. Fennie, D. G. Schlom, and K. M. Shen, Phys. Rev. Lett. **114**, 1 (2015).

[8]   D. J. Groenendijk, C. Autieri, J. Girovsky, M. C. Martinez-Velarte, N. Manca, G. Mattoni, A. M. R. V. L. Monteiro, N. Gauquelin, J. Verbeeck, A. F. Otte, M. Gabay, S. Picozzi, and A. D. Caviglia, Phys. Rev. Lett. **119**, 2 (2017).

[9]   P. Schütz, D. Di Sante, L. Dudy, J. Gabel, M. Stübinger, M. Kamp, Y. Huang, M. Capone, M. A. Husanu, V. N. Strocov, G. Sangiovanni, M. Sing, and R. Claessen, Phys. Rev. Lett. **119**, 1 (2017).

[10]   Y. A. Bychkov and E. I. Rashba, JETP Lett. **39**, 78 (1984).

[11]   R. Winkler, *Spin--Orbit Coupling Effects in Two-Dimensional Electron and Hole Systems* (Springer Berlin Heidelberg, Berlin, Heidelberg, 2003).

[12]   V. Galitski and I. B. Spielman, Nature **494**, 49 (2013).

[13]   P. Seiler, Anti-Localization in Oxide Heterostructures Dissertation, Universität Augsburg, 2018.

[14]   J. Nitta, T. Akazaki, H. Takayanagi, and T. Enoki, Phys. Rev. Lett. **78**, 1335 (1997).

[15]   G. Lommer, F. Malcher, and U. Rossler, Phys. Rev. Lett. **60**, 728 (1988).

[16] H.-Z. Lu and S.-Q. Shen, Phys. Rev. Lett. **112**, 146601 (2014).

[17] D. I. Khomskii, *Transition Metal Compounds* (Cambridge University Press, 2014).

[18] I. Dzyaloshinsky, J. Phys. Chem. Solids **4**, 241 (1958).

[19] T. Moriya, Phys. Rev. **120**, 91 (1960).

[20] K. Ueno, S. Nakamura, H. Shimotani, A. Ohtomo, N. Kimura, T. Nojima, H. Aoki, Y. Iwasa, and M. Kawasaki, Nat. Mater. **7**, 855 (2008).

[21] H. Yuan, H. Shimotani, A. Tsukazaki, A. Ohtomo, M. Kawasaki, and Y. Iwasa, Adv. Funct. Mater. **19**, 1046 (2009).

[22] J. T. Ye, S. Inoue, K. Kobayashi, Y. Kasahara, H. T. Yuan, H. Shimotani, and Y. Iwasa, Nat. Mater. **9**, 125 (2010).

[23] Y. Yamada, K. Ueno, T. Fukumura, H. T. Yuan, H. Shimotani, Y. Iwasa, L. Gu, S. Tsukimoto, Y. Ikuhara, and M. Kawasaki, Science (80-.). **332**, 1065 (2011).

[24] X. Leng, J. Garcia-Barriocanal, S. Bose, Y. Lee, and A. M. Goldman, Phys. Rev. Lett. **107**, 6 (2011).

[25] A. T. Bollinger, G. Dubuis, J. Yoon, D. Pavuna, J. Misewich, and I. BoŽović, Nature **472**, 458 (2011).

[26] H. Shimotani, H. Asanuma, A. Tsukazaki, A. Ohtomo, M. Kawasaki, and Y. Iwasa, Appl. Phys. Lett. **91**, 10 (2007).

[27] D. T. Limmer, Phys. Rev. Lett. **115**, 1 (2015).

[28] L. J. Van Der PAUW, Philips Tech. Rev. **20**, 220 (1958).

[29] S. Hikami, A. I. Larkin, and Y. Nagaoka, Prog. Theor. Phys. **63**, 707 (1980).

[30] S. Maekawa, Journa Phys. Soc. Japan **50**, 2516 (1981).

[31] S. Hurand, A. Jouan, C. Feuillet-Palma, G. Singh, J. Biscaras, E. Lesne, N. Reyren, A. Barthélémy, M. Bibes, J. E. Villegas, C. Ulysse, X. Lafosse, M. Pannetier-Lecoeur, S. Caprara, M. Grilli, J. Lesueur, and N. Bergeal, Sci. Rep. **5**, 1 (2015).

[32] N. Manca, D. J. Groenendijk, I. Pallecchi, C. Autieri, L. M. K. Tang, F. Telesio, G. Mattoni, A. McCollam, S. Picozzi, and A. D. Caviglia, Phys. Rev. B **97**, 2 (2018).

[33] L. Zhang, Q. Liang, Y. Xiong, B. Zhang, L. Gao, H. Li, Y. B. Chen, J. Zhou, S. T. Zhang, Z. Bin Gu, S. H. Yao, Z. Wang, Y. Lin, and Y. F. Chen, Phys. Rev. B - Condens. Matter Mater. Phys. **91**, 1 (2015).

[34] K. Yoshimatsu, K. Horiba, H. Kumigashira, T. Yoshida, A. Fujimori, and M. Oshima, Science (80-.). **333**, 319 (2011).

[35] S. Okamoto, Phys. Rev. B - Condens. Matter Mater. Phys. **84**, 1 (2011).

[36] M. Kobayashi, K. Yoshimatsu, E. Sakai, M. Kitamura, K. Horiba, A. Fujimori, and H. Kumigashira, Phys. Rev. Lett. **115**, 1 (2015).

[37] T. C. Chiang, Surf. Sci. Rep. **39**, 181 (2000).

[38] M. Milun, P. Pervan, and D. P. Woodruff, Reports Prog. Phys. **65**, 99 (2002).

[39] E. F. Bertaut, in edited by G. T. Rado and H. Suhl (New York: Academic Press, 1965), p. 149.

[40] E. Bousquet and A. Cano, J. Phys. Condens. Matter **28**, (2016).

References

Chapter 5: Conclusions

In this thesis we have explored routes to manipulate the emergent electronic states nucleating at oxide interfaces towards their functionalization in device novel concepts in a future oxide electronics. Two scenarios have been examined, namely the coupling of the ferroelectric polarization to the electrochemical states driven by oxygen deficiency and mixed valence, and the use of oxides with strong spin orbit interaction to couple the electronic structure to electric fields. The main conclusions achieved can be summarized as follows.

1) The electronic reconstruction occurring at oxide interfaces may be the source of interesting device concepts for future oxide electronics. Among oxide devices, multiferroic tunnel junctions are being actively investigated as they offer the possibility to modulate the junction current by independently controlling the switching of the magnetization of the electrodes and of the ferroelectric polarization of the barrier. In this thesis we have shown that the spin reconstruction at the interfaces of a $La_{0.7}Sr_{0.3}MnO_3$/$BaTiO_3$/$La_{0.7}Sr_{0.3}MnO_3$ multiferroic tunnel junction is the origin of a spin filtering functionality which can be turned on and off by reversing the ferroelectric polarization. We have demonstrated a very large ferroelectric modulation of the tunneling magnetoresistance of a multiferroic tunnel junction, driven by an interfacially induced spin filtering functionality. Spin filtering is triggered by the induced spin polarization of the ferroelectric interface, probably by accumulation of oxygen vacancies, which yields a Ti^{3+} species bonding to Mn across a Mn-O-Ti superexchange path. The ferroelectric control relies in asymmetries in the magnetic structure of the interfaces. The very large modulation of the TMR between 10 and 1000%, enabled by the emergent spin filter calls for future strategies for the design of wider classes of interfacial spin filters exploiting electronic reconstruction at oxide interfaces.

2) We have demonstrated the possibility of engineering ferroionic states at the interface between a ferroelectric and a non superconducting cuprate in a ferroelectric tunnel junction. We have found fingerprints of superconductivity at the interface between a non superconducting cuprate and a ferroelectric barrier in a tunnel junction. As probed by tunneling conductance, such phase is characterized by a 22 meV superconducting gap and a critical temperature T_C as high as 70 K, as well as by spectral features specific of d-wave superconductors such as $YBa_2Cu_3O_7$. Furthermore, we show that ferroelectric switching modulates the superconducting gap, which implies the that coupling between ferroelectric polarization and the

ionization of oxygen vacancies controls the interfacial phase doping. We propose that the transfer of oxygen vacancies from the cuprate interface to the titanate barrier triggered by the modulation of the lattice expansion at both sides of the interface, plays a major role on the stabilization of the superconducting phase. In addition, the coupled switching of ferroelectric polarization and oxygen vacancies produce a strong doping modulation at the interface layers resulting from the combined effect of the doping field of the oxygen vacancies and the field effect to screen the ferroelectric polarization. This ferroionic route appears as a promising new strategy to explore phase diagrams at doping levels far beyond the ones reached with field effect or ionic liquid doping.

3) We have shown that in SrIrO$_3$ ultrathin films, the large electric fields generated in a field effect experiment with ionic liquids couples strongly to the electronic structure, producing deep modifications, which are beyond those expected from doping. The electric field modulation of new inter-orbital hopping channels, opened by the broken inversion symmetry, explains the anomalous band splitting triggering the metal to insulator transition. The emergent anomalous Hall effect related to the out of plane canted antiferromagnetic state found in the insulating phase supplies solid evidence for the leading role played by electron correlations in yielding the transition. The picture emerges that the electric field controlled symmetry breaking provides an effective knob to modulate the effective strength of the correlations yielding the MIT transition. A final remark concerns the finding of a canted antiferromagnetic insulating state tunable by an electric field. Ferromagnetic insulators are scarce, yet they are very useful in spintronics as spin filters, or as electrodes in proximity interactions. On the other hand, metals with strong spin orbit interaction are desirable as spin-charge converters. The possibility of switching between both metallic and ferromagnetic insulating behavior with an electric field demonstrated in this work may inspire novel device concepts in low dissipation oxide electronics.

List of publications

1. Cabero, M., K. Nagy, **F. Gallego**, A. Sander, M. Rio, F. A. Cuellar, J. Tornos, D. Hernandez-Martin, N. M. Nemes, F. Mompean, M. Garcia-Hernandez, A. Rivera-Calzada, Z. Sefrioui, N. Reyren, T. Feher, M. Varela, C. Leon, and J. Santamaria. 2017. "Modified Magnetic Anisotropy at LaCoO 3 /La 0.7 Sr 0.3 MnO 3 Interfaces." *APL Materials* 5(9):096104.

2. Cuellar, Fabian A., David Hernandez-Martin, Javier Tornos, **Fernando Gallego**, Gloria Orfila, Alberto Rivera-Calzada, Zouhair Sefrioui, Carlos Leon, and Jacobo Santamaria. 2018. "Interface Magnetism in La0.7Ca0.3MnO3/PrBa2Cu3O7 Epitaxial Heterostructures." *Physica Status Solidi (A) Applications and Materials Science* 215(19):1–5.

3. Grandal, Javier, Juan I. Beltran, Gabriel Sanchez-Santolino, **Fernando Gallego**, Javier Tornos, Mariona Cabero, Carlos Leon, Federico Mompean, Mar Garcia-Hernandez, Stephen J. Pennycook, M. Carmen Munoz, Jacobo Santamaria, and Maria Varela. 2017. "High Resolution Studies of Oxide Multiferroic Interfaces in the Aberration-Corrected STEM." *Microscopy and Microanalysis* 23(S1):1592–93.

4. Niu, Yue, Riccardo Frisenda, Simon A. Svatek, Gloria Orfila, **Fernando Gallego**, Patricia Gant, Nicolás Agraït, Carlos Leon, Alberto Rivera-Calzada, David Pérez De Lara, Jacobo Santamaria, and Andres Castellanos-Gomez. 2017. "Photodiodes Based in La 0.7 Sr 0.3 MnO 3 /Single Layer MoS 2 Hybrid Vertical Heterostructures." *2D Materials* 4(3):034002.

5. J. Tornos*., **F. Gallego***, S. Valencia, Y. H. Liu, V. Rouco, V. Lauter, R. Abrudan, C. Luo, H. Ryll, Q. Wang, D. Hernandez-Martin, G. Orfila, M. Cabero, F. Cuellar, D. Arias, F. J. Mompean, M. Garcia-Hernandez, F. Radu, T. R. Charlton, A. Rivera-Calzada, Z. Sefrioui, S. G. E. Te Velthuis, C. Leon, and J. Santamaria. 2019. "Ferroelectric Control of Interface Spin Filtering in Multiferroic Tunnel Junctions." *Physical Review Letters* 122(3):37601.

Contribution to Symposiums

-Suzanne Te Velthuis et al. **APS March Meeting** (Denver, Colorado, 2020) – Oral – *Magnetic properties of Manganite/Iridate bilayers.*

-F. Gallego et al. **APS March Meeting** (Denver, Colorado, 2020) – Oral – *Fingerprints of interface superconductivity in ferroelectric tunnel junctions.*

-F. Gallego et al. **XXXVII Reunión Bienal de la RSEF** (Zaragoza, Spain, 2019) – Oral – *Tunable interfacial superconductivity in multiferroic tunnel junctions.*

-J. Santamaria et al. **APS March Meeting** (Boston, Massachusetts, 2019) – Oral – *Metal insulator transition in SrIrO3 Ultra-Thin Films examined by ionic liquid gating.*

-J. Santamaria et al. **APS March Meeting** (Boston, Massachusetts, 2019) –Written – *Controlling transport of the SrIrO3 correlated semimetal by doping with an ionic liquid.*

-J. Tornos et al. 10th International Symposium on Mellic Multilayer **MML 2019**. Madrid, Spain. June 2019. -Oral- *Ferroelectric Control of Interface Spin Filtering in Multiferroic MTJs.*

-F. Gallego et al. **GEFES 2018** (Valencia, Spain, 2018). – Poster – *Control of magnetic and ferroelectric states at interfaces between correlated oxides.*

*-M. Varela et al. at First International Conference on Electron Microscopy of Nanostructures, **ELMINA2018**, Belgrade, Serbia, August* 2018.- Oral- *High Resolution STEM-EELS Mapping of Magnetic Quantities Across Oxide Multiferroic Interfaces.*

-S. te Velthuis et al. *21st International Conference on Magnetism, **ICM2018**, San Francisco, California, USA. July* 2018. -Oral- *Magnetism of Manganite/Iridiate Bilayers.*

-J. Tornos et al. **25th International Workshop on Oxide Electronics**. Les Diablerets, Switzerland. October 2018. -Poster- *Ionic Liquid Gating of SrIrO$_3$ Ultra-Thin Films.*

-F. Gallego et al. **ISOE 2017** (Cargesse, Corsica, 2017) – Poster - *Control of magnetic states at multiferroic oxide interfaces: The role of oxygen vacancies and ferroelectric polarization.*

Short research stays

-Imaging domain walls in La0.7Sr0.3MnO3 nanowires – **BESSY II**. Berlin. January 2019. Techniques: SPEEM, X-Ray absorption and spectroscopy. Duration: 1 Week.

-Probing the long range Josephson coupling by its magnetic fingerprint in planar oxide cuprate/manganite nanostructures – **BESSY II**. Berlin. March 2018. Techniques: SPEEM, X-Ray absorption and spectroscopy. Duration: 1 Week.

-Superconducting ferromagnetic interactions as seed for local imprint of non-trivial spin topologies. - **BESSY II**. Berlin. January 2018. Techniques: SPEEM, X-Ray and spectroscopy. Duration: 1 Week.

-Manipulation of magnetic states at oxide interfaces by ferroelectric polarization - **BESSY II**. Berlin. October 2017. Techniques: SPEEM, X-Ray absorption and spectroscopy. Duration: 1 Week.

-Controlling magnetic groundstates at correlated oxide interfaces by induced oxygen vacancy profiles - **BESSY II**. Berlin. August 2017 and April 2017. Techniques: X- Ray absorption and spectroscopy. Duration: 2 Weeks.

-Tailoring magnetic textures with superconductors: Hybrid superconductor/ferromagnetic nanostructures for future spintronic applications - **BESSY II**. Berlin. May 2017. Techniques: SPEEM, X-Ray absorption and spectroscopy. Duration: 1 Week.

-Controlling magnetic groundstates at correlated oxide interfaces by induced oxygen vacancy profiles - **BESSY II**. Berlín. Diciembre 2016 y Febrero 2017. Techniques: SPEEM, X-Ray absorption and spectroscopy. Duration: 2 Weeks.

*-2018093155 - Investigation of an emergent magnetic state in (La,Sr)MnO3/SrIrO3 bilayers probed by X-Ray magnetic circular dichroism. Standard Proposal. **ALBA**, Barcelona. June 2019.* Techniques: X-Ray absorption and spectroscopy. Duration: 3 days.

*- 2018022704 - Investigation of an emergent magnetic state in (La,Sr)MnO3/SrIrO3 bilayers probed by x-ray magnetic circular dichroism. Standard Proposal. **ALBA**, Barcelona. June 2018.* Techniques: X-Ray absorption and spectroscopy. Duration: 3 days.

Short research stays

Appendix 1: Study of magnetism evolution in LSMO junctions

A magnetism study was perform at VEKMAG for two different samples that contained LSMO: A bilayer consisting on STO(100)// LSMO (10nm)/BTO(4nm), and a trilayer consisting on STO(100)//LSMO(10nm)/BTO(4nm)/LSMO(3nm) (Figure A.1). We observe that both samples have a lower coercive field at 160 Oe. We associate this coercive field to the common layer in both samples, the bottom LSMO. At higher fields the trilayer has another coercive field at 470 Oe, which may be associated to the top LSMO layer.
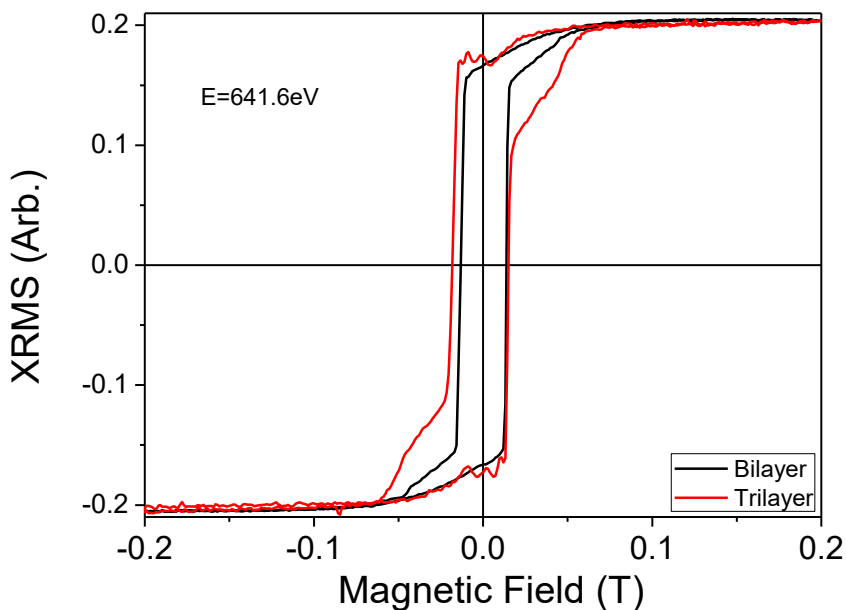

Figure A.1: Normalized XRMS image of a LSMO/BTO sample (Black line) and a LSMO/BTO/LSMO sample (red line). The measurements were taken at 10K and at the Mn edge (641.6 eV).

Appendix 1: Study of magnetism evolution in LSMO junctions

Appendix 2: Superconducting junction with silver electrode

In order to study the influence of the metallic top electrode in the presence of a superconducting state in the LSCO, a sample with a silver electrode was fabricated. Figure A.2 presents the differential conductance measurements, showing that a superconducting gap also emerges at low voltages (20 meV) and low temperatures (40K), as in the case of gold. The result is an evidence that the superconducting state is generated far from the metallic electrode.
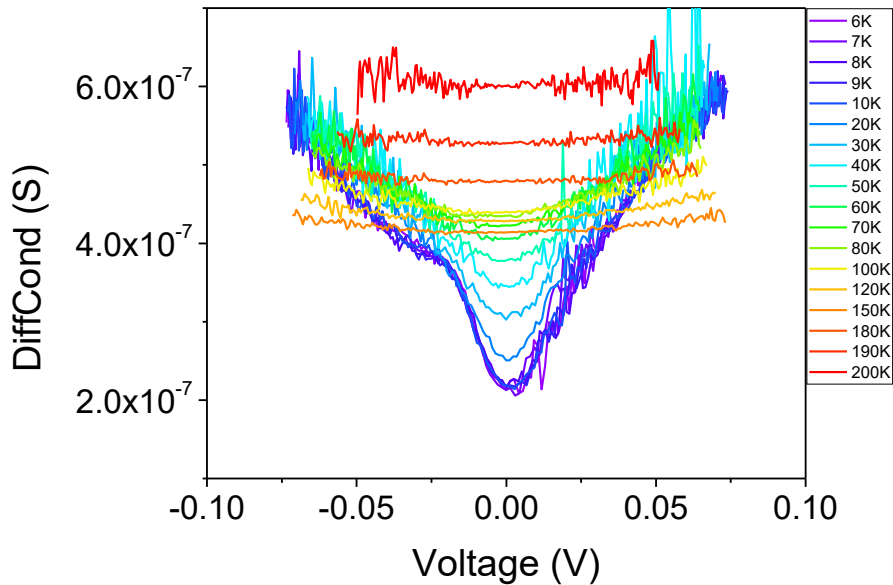

Figure A.2: Differential conductance versus voltage measurements as a function of temperature of a STO(100)//LSMO(20nm)/BTO(4.4nm)/LSCO(10nm)/Ag tunnel junction. A superconducting gap is present at the lowest temperature and survives up to 50K.

Appendix 2: Superconducting junction with silver electrode

Appendix 3: Ionic Liquid degradation study

Capacitance measurements were performed in IL on the same conditions as the experiment, in order to study the possible degradation of the IL with the applied voltage. The capacitance measurements of the EDLT were taken between -3V and +3V. In this range, the ionic liquid shows an electrostatic contribution without degradation. It is important to verify how the EDLT doping mechanism works, and the way to do so is studying the interaction (electronic or electrochemical) between the ionic liquid and the oxide surface. The Impedance Spectroscopy technique offers an ideal field to analyze the behavior of this interfacial doping process [40,41]. In this experiment we investigated the charge mechanics of the EDL in the same configuration as in the Hall and MR measurements. Capacitance was measured as a function of the external voltage at 230K, which is the polarization temperature, when the ionic liquid ions are mobile. From these measurements we can extract information about the formation of the double layer as the doping process is carried out. As can be seen in the Figure A.3, A purely electrostatic mechanism is found at low voltages. Thus, we can be sure that no degradation is appearing in the IL during the SIO gating process.
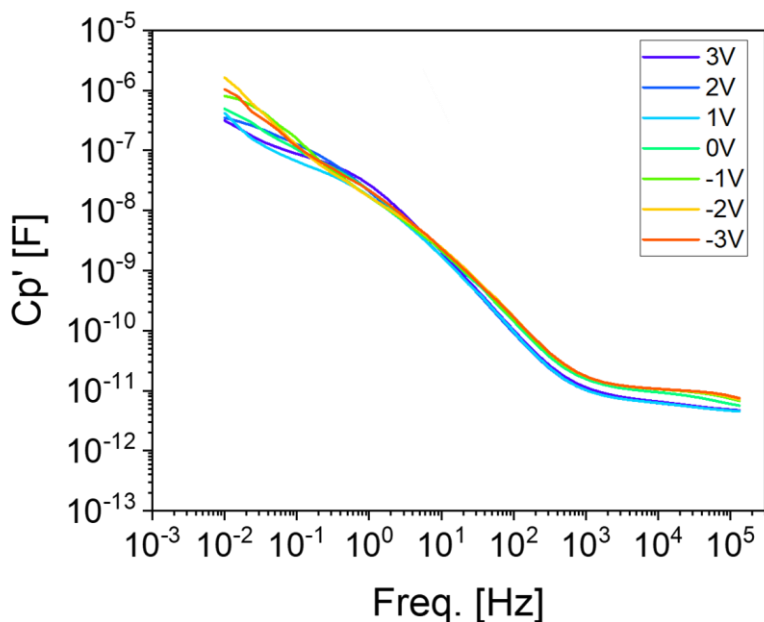

Figure A.3: Capacitance measurements of the EDL at voltages in the working range of the experiment. This measurement proves that the gating process is electrostatic.

However, at high positive voltages (over +3V) a degradation of the double layer was obtained that is absent in the negative voltages. This is associated with the oxygen displacement of the ions up to the interface provoking the EDL to break (Figure A.4)
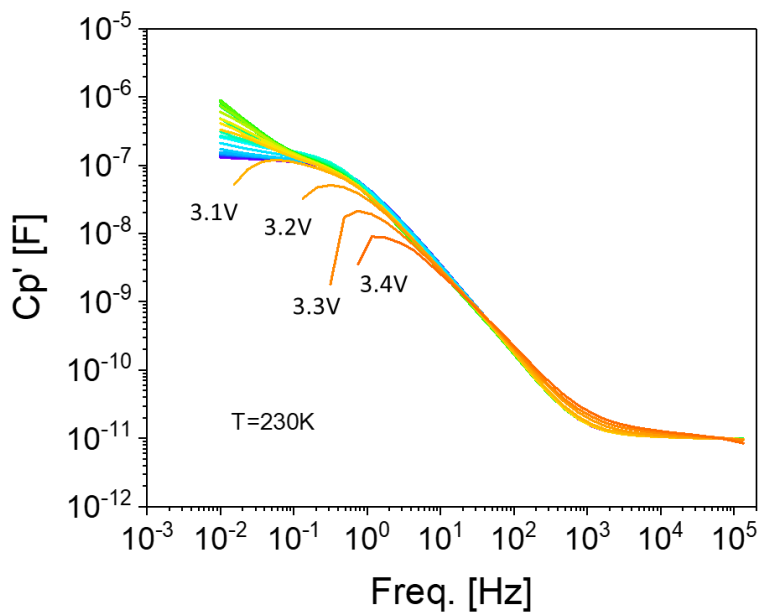

Figure A.4: Capacitance measurements of the EDL at voltages over the working range of the experiment. At voltages larger than 3V, electrochemical reactions start to happen.

Resumen en Castellano

En los últimos años, la demanda de ordenadores con mayor velocidad de computación y capacidad en un menor tamaño ha generado un gran interés en la exploración de materiales que puedan ser útiles en esos ámbitos. En particular, los óxidos basados en metales de transición (TMOs) han atraído gran atención en los últimos años debido al amplio abanico de propiedades físicas que pueden aparecer en estos sistemas gracias a la interacción entre algunas de sus características que en un principio deberían ser independientes entre sí, como el espín, la carga, la órbita, la red, etc. En concreto, las propiedades de conducción del sistema pueden variar desde aislante a metal, pasando por superconductor. La estructura común en todos estos sistemas es el tipo perovskita. Una parte muy importante de estos sistemas es la superficie (o intercara), que es una zona donde la distancia entre iones, y por lo tanto sus enlaces, se altera, debido en parte a la ruptura de simetría. Esto, unido a las reconstrucciones electrónicas que se dan, promueve la aparición de nuevas fases en superficies e intercaras. La valencia mixta de los iones implicados en estos sistemas favorece la transferencia de carga necesaria para la reconstrucción electrónica interfacial, lo cual desemboca en propiedades físicas que se producen sólo en una sección reducida del sistema, como es la intercara.

En este contexto, la fabricación de heteroestructuras y dispositivos basados en intercaras de óxidos complejos tiene un gran interés tanto fundamental como tecnológico. Es de especial interés el control y la modificación de las propiedades interfaciales mediante estímulos externos como campos eléctricos, campos magnéticos, tensión epitaxial, etc. Con esta misión, esta tesis se ha enfocado en el crecimiento y caracterización de películas delgadas de óxidos complejos, y su inclusión en dispositivos tales como uniones túnel multiferroicas (MFTJ) o transistores eléctricos de doble capa (EDLT). Las uniones túnel, son idóneas para estudiar efectos interfaciales debido a alta sensibilidad de la corriente túnel a los estados en la intercara. La inclusión de una barrera túnel ferroeléctrica permite, gracias al apantallamiento de carga, modificar el nivel de dopado de los electrodos en la intercara, tanto mediante el movimiento de cargas como el movimiento e ionización de vacantes de oxígeno. Los dispositivos EDLT permiten, mediante la aplicación de voltajes de puerta, la generación de densidades de portadores inalcanzables mediante otros dispositivos (10^{13} portadores/cm^2). Esto permite explorar la transición metal/aislante en materiales cuánticos, pudiendo encontrar propiedades inesperadas en los sistemas estudiados.

Objetivos

- Crecimiento de películas delgadas y heteroestructuras de óxidos complejos mediante la técnica de pulverización catódica (sputtering) y su caracterización tanto estructural como eléctrica, garantizando unas propiedades de conducción aceptables para la fabricación de dispositivos.
- Fabricación tanto de uniones túnel multiferroicas basadas en $La_{0.84}Sr_{0.16}MnO_3/BaTiO_3$ con $La_{0.84}Sr_{0.16}MnO_{3.}$ como electrodo superior para crear uniones simétricas y con $La_{0.84}Sr_{0.16}CuO_{2.5-\delta}$ para crear uniones asimétricas, como de barras Hall en $SrIrO_3$.
- Caracterización de propiedades de magnetotransporte en los dispositivos fabricados.
- Inducción de propiedades novedosas de intercara en los óxidos complejos estudiados.

Resultados

En el capítulo 3 se han estudiado las propiedades eléctricas y estructurales de láminas delgadas de $La_{0.84}Sr_{0.16}CuO_{2.5-\delta}$. Además, se han fabricado uniones túnel simétricas $La_{0.84}Sr_{0.16}MnO_3/BaTiO_3/La_{0.84}Sr_{0.16}MnO_3$ y uniones túnel asimétricas $La_{0.84}Sr_{0.16}MnO_3/BaTiO_3/La_{0.84}Sr_{0.16}CuO_{2.5-\delta}$. Se ha encontrado la aparición de un estado magnético inducido en el titanato de bario probablemente debido al fenómeno de Supercanje con el electrodo inferior de LSMO. Se ha encontrado en la unión túnel asimétrica la aparición de un estado superconductor interfacial en LSCO que se puede modular mediante la inversión de la polarización ferroeléctrica.

En el capítulo 4 se realizó una caracterización estructural y eléctrica de láminas delgadas de $SrIrO_3$. Se estudió la transición metal-aislante en función tanto del espesor como de la tensión epitaxial. Se fabricó un dispositivo EDLT basado en el uso de un líquido iónico con el objetivo de tomar medidas de magnetorresistencia y Hall y modelizarlas. En estas medidas a baja temperatura se encontró un ferromagnetismo débil en el estado aislante del SIO, el cual se asocia a las correlaciones electrónicas del sistema.

Conclusiones

En todos los sistemas utilizados para esta tesis aparecen una o varias interfases o superficies en diferentes óxidos, de forma que se puedan explorar las transiciones entre los diferentes estados del diagrama de fases de los óxidos. Como conclusiones generales del trabajo cabe destacar:

- En las uniones túnel simétricas se ha encontrado un estado magnético interfacial en el titanio del BTO con una orientación relativa antiparalela al

estado magnético del LSMO inferior. El movimiento e ionización de vacantes de oxígeno promueve la aparición de la interacción de supercanje en el enlace Mn-O-Ti.

- En las uniones túnel asimétricas se ha encontrado un estado superconductor en la intercara entre BTO y LSCO. Este estado viene provocado por el dopado interfacial que generan la ionización de las vacantes de oxígeno y la polarización ferroeléctrica.

- En los dispositivos de SIO, el confinamiento generado por los campos eléctricos debidos al dopado electrostático se encarga de modular algunas propiedades intrínsecas del sistema, como el ancho de banda, lo que desencadena la transición metal/aislante. Se encontró un estado magnético en el sistema cuando se encuentra en el estado aislante, el cual puede provenir de la rotación de octaedros de oxígeno en la celda unidad del SIO para compensar los campos generados por el dopado electrostático.

A lo largo de esta tesis se han estudiado las propiedades de interfase de óxidos complejos en dispositivos micrométricos. Los resultados obtenidos muestran la importancia de la presencia de vacantes de oxígeno en las interfases de heteroestructuras y su fuerte influencia en las propiedades de conducción del sistema. Se ha comprobado que es posible modificar el estado intrínseco de óxidos complejos mediante la aplicación de campos eléctricos. El dopado electrostático con líquido iónico puede también generar transiciones de fase en óxidos.

A pesar de la cantidad de preguntas sin responder relacionadas con los mecanismos intrínsecos relacionados con las propiedades estudiadas, los resultados obtenidos en los experimentos de esta tesis son de gran interés, no sólo desde el punto de vista fundamental, sino también para utilizar estas propiedades para el diseño y la fabricación de dispositivos espintrónicos funcionales en el futuro.

Resumen en Castellano